LETTER

https://doi.org/10.1038/s41586-018-0710-1

Late Middle Pleistocene Levallois stone-tool technology in southwest China

Yue Hu[1], Ben Marwick[1,2]*, Jia-Fu Zhang[3], Xue Rui[1], Ya-Mei Hou[4,5], Jian-Ping Yue[4,5], Wen-Rong Chen[6], Wei-Wen Huang[4] & Bo Li[1,7]*

Levallois approaches are one of the best known variants of prepared-core technologies, and are an important hallmark of stone technologies developed around 300,000 years ago in Africa and west Eurasia[1,2]. Existing archaeological evidence suggests that the stone technology of east Asian hominins lacked a Levallois component during the late Middle Pleistocene epoch and it is not until the Late Pleistocene (around 40,000–30,000 years ago) that this technology spread into east Asia in association with a dispersal of modern humans. Here we present evidence of Levallois technology from the lithic assemblage of the Guanyindong Cave site in southwest China, dated to approximately 170,000–80,000 years ago. To our knowledge, this is the earliest evidence of Levallois technology in east Asia. Our findings thus challenge the existing model of the origin and spread of Levallois technologies in east Asia and its links to a Late Pleistocene dispersal of modern humans.

Middle Palaeolithic prepared-core reduction strategies, commonly referred to as Levallois or mode III technologies, are remarkable for both their ubiquity in Eurasia and Africa, and their apparent absence in east Asia during the Middle and Late Pleistocene (Fig. 1). This uneven global distribution has obscured the origins of Levallois technology, and its relationship to later technologies. The appearance of Levallois artefacts around 200–300 thousand years ago (ka) in Eurasia marks the transition from the Lower to Middle Palaeolithic in these regions. This was a major innovation in optimizing lithic tool manufacturing[3], potentially signalling an expansion of archaic *Homo* populations from Africa[4]. However, early Levallois technology found with bifaces in the southern Caucasus suggests that Levallois technology evolved from the existing local Acheulian (or mode II) technological systems[5]. This supports a hypothesis of isolated technological convergence[6], rather than a single-origin and dispersal model. The recent discovery of Levallois technology in India from around 385–172 ka[7] also raised the need to re-evaluate the relationship between the origins of Middle Palaeolithic culture in South Asia and the dispersal of modern humans.

Previous archaeological evidence from China, Mongolia, South Korea and Japan[8–14] suggests that major changes in raw material procurement, core reduction, retouch and typology of stone artefacts in east Asia tend to be clustered at the Upper Pleistocene (Fig. 1), indicating that a distinct Middle Palaeolithic period of systematic technological innovation did not occur in eastern Asia[15]. Without early ancestral technologies such as the Levallois technology, the appearance of blades in the Upper Pleistocene in East Asia indicates that they may have resulted from population admixture or replacement. The apparent absence of the Levallois technology in east Asia similarly raises critical questions about the relationship between cultural and biological trajectories of populations in east Asia and western regions.

Here we describe the stone artefact assemblage from Guanyindong Cave in the Guizhou province, southwest China (Fig. 2a) that provide evidence of an early appearance of Levallois artefacts in East Asia. Discovered in 1964, Guanyindong Cave is a limestone cave (Extended Data Fig. 1). Excavations during 1964–1973 recovered more than 3,000 stone artefacts and numerous fossilized fauna[16]. Faunal remains mostly belong to the Middle Pleistocene *Ailuropoda*–*Stegodon* fauna complex (Supplementary Information). Several trenches were opened within and in front of the cave, but most of the artefacts were excavated from the main entrance located at the west end of the cave. The stratigraphy of the main entrance was divided into nine layers that can be attributed to three groups (groups A, B and C) (Extended Data Fig. 2 and Supplementary Information). Stone artefacts and fossils were found in groups A (layer 2) and B (layers 3–8) only. Because this site was excavated more than 40 years ago, only 204 pieces of the studied stone artefacts have clear stratigraphic information (87 artefacts from group A and 117 from group B). Among these, we identified five artefacts as Levallois; three of these (two cores and one tool) are from group A and two (all tools) are from group B (Extended Data Figs. 5–7, 10). This suggests that Levallois concepts were present at this site throughout the whole occupation period.

This site was previously dated by U-series techniques[17,18], and a wide range of U-series ages ranging from around 50 to about 240 thousand years (kyr) old have been reported (Supplementary Table 1). However, many of these U-series ages were made on fossils, which should be treated as minimum age estimates[19]. Furthermore, most of the dated carbonate samples do not have firm stratigraphic control, so it is unreliable to associate their U-series ages to the sediment layers (see Supplementary Information for a full discussion on U-series results). To confirm the age of the Guanyindong assemblage, we used single-grain optically stimulated luminescence (OSL) dating on quartz (see Methods) to determine the ages of the deposits from layer 1, groups A and B (Fig. 2b and Extended Data Figs. 3, 4). Three samples from layer 1 yielded age estimates of ~70–40 kyr. Four samples from group A yielded ages of around 90–80 kyr and six samples from group B yielded ages of around 170–160 kyr (Fig. 2b). The OSL ages obtained for each of the groups are statistically consistent with each other at 2σ. Our dating results suggest that both groups A and B were deposited over short periods, although there is a large gap in age (around 80 kyr) between groups A and B, which is consistent with the observation of a sedimentary unconformity between the two groups (Extended Data Fig. 2). Our OSL chronology, therefore, securely places the date of deposit for the Guanyindong archaeological deposits (layers 2–8) between approximately 170 and about 80 ka.

The Guanyindong Cave assemblage consists of flakes, flake breaks, retouched pieces, cores, chunks and debris. The raw materials are predominantly chert (Extended Data Figs. 8–10; see Supplementary Information and Supplementary Figs. 21–24). On the basis of the detailed analysis of 2,273 stone artefacts, we found evidence of Levallois concepts in 45 specimens (see Methods and Supplementary Information for detailed justification), including 11 cores, 30 flakes and

[1]Centre for Archaeological Science, School of Earth and Environmental Sciences, University of Wollongong, Wollongong, New South Wales, Australia. [2]Department of Anthropology, University of Washington, Seattle, WA, USA. [3]MOE Laboratory for Earth Surface Processes, Department of Geography, College of Urban and Environmental Sciences, Peking University, Beijing, China. [4]Key Laboratory of Vertebrate Evolution and Human Origins, Institute of Vertebrate Paleontology and Paleoanthropology, Chinese Academy of Sciences, Beijing, China. [5]CAS Centre for Excellence in Life and Paleo-environment, Beijing, China. [6]Qianxi County Bureau of Cultural Relics Protection, Bijie, China. [7]ARC Centre of Excellence for Australian Biodiversity and Heritage, University of Wollongong, Wollongong, New South Wales, Australia. *e-mail: bmarwick@uw.edu; bli@uow.edu.au

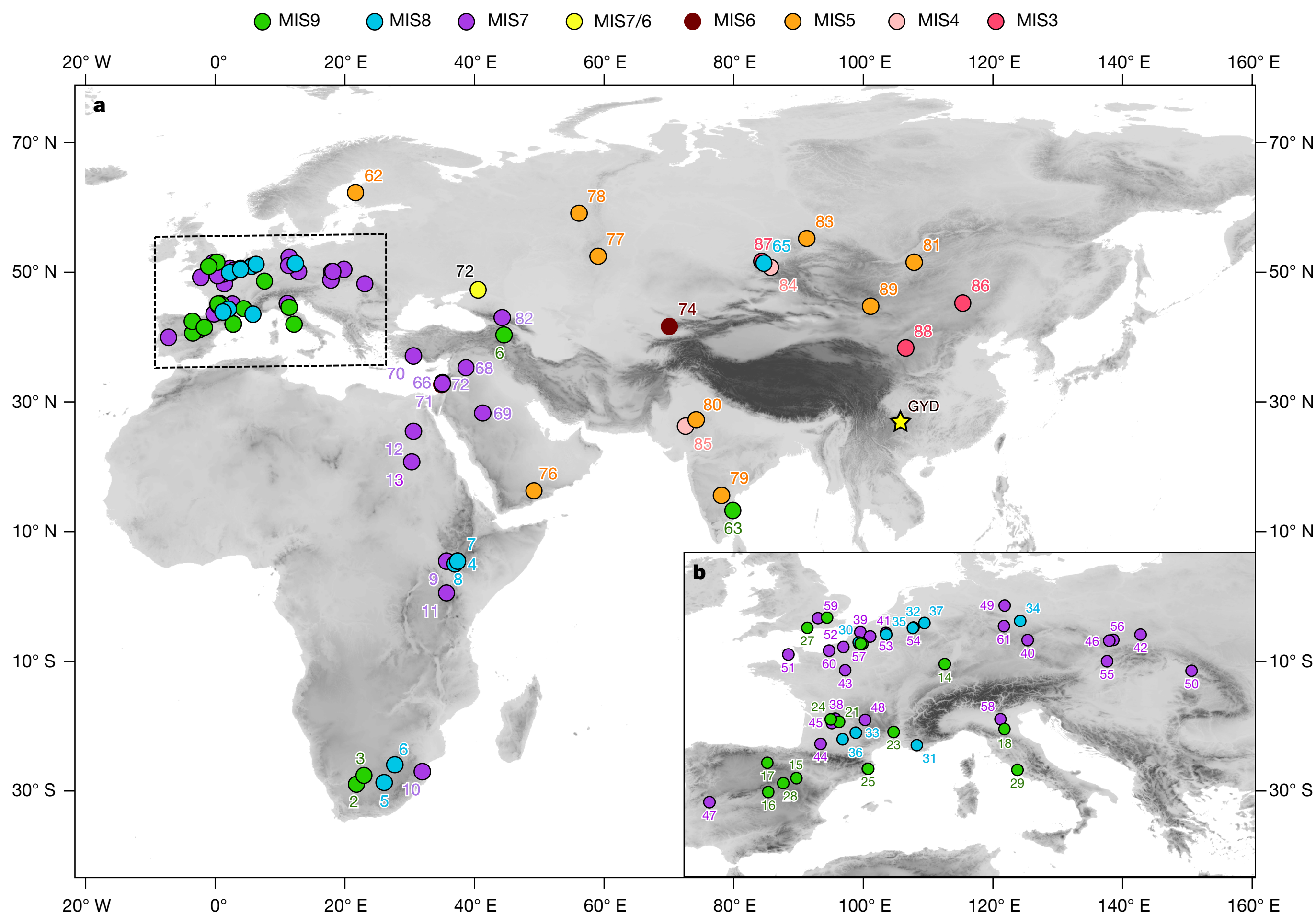

Fig. 1 | Distribution of Levallois technology during the late Middle Pleistocene (from MIS 9 to 3) in Africa and Eurasia. a, **b**, Distribution of Levallois technology across Africa and Eurasia. **b**, Magnification of the region inside the dashed rectangle in **a**. Detailed information on the sites is provided in Supplementary Table 2. The MIS corresponding to the chronology of individual sites is indicated by different colour-coded symbols. Note that there are a large number of sites that are younger than MIS 7 in Europe and Africa; however these sites are not shown here. GYD, Guanyindong Cave.

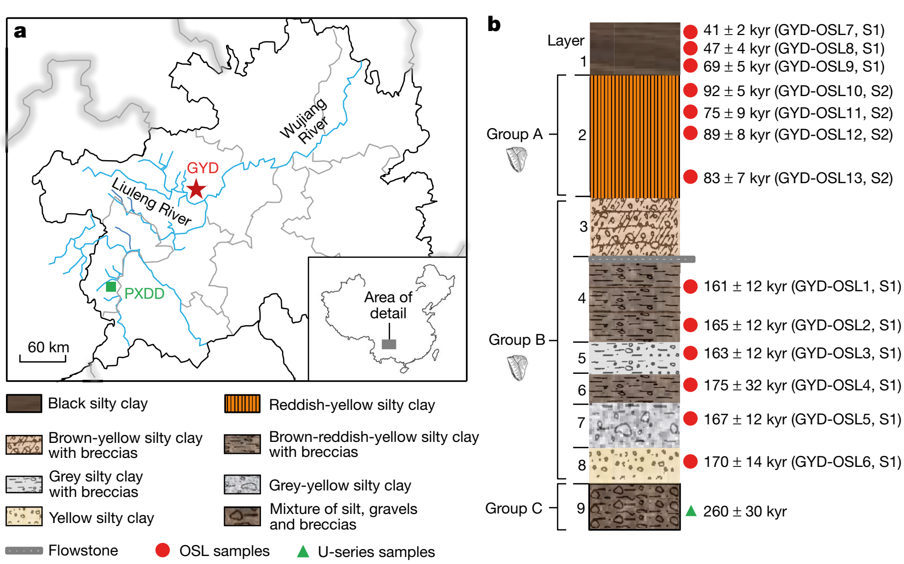

Fig. 2 | Location, stratigraphy and chronology of the Guanyindong site. a, Location of the Guanyindong Cave (GYD) and Panxian Dadong (PXDD) sites in Guizhou Province, southwest China. **b**, Schematic composite stratigraphy at the south wall of the cave entrance, with the depth, profile and ages of the OSL samples and U-series[17] dating results indicated. The sketches of stone tools indicate cultural layers. The uncertainties of the OSL ages are expressed at 1σ. S1 and S2 represent the two residual profiles at the south wall of the cave entrance (Extended Data Fig. 2) where the OSL samples were taken.

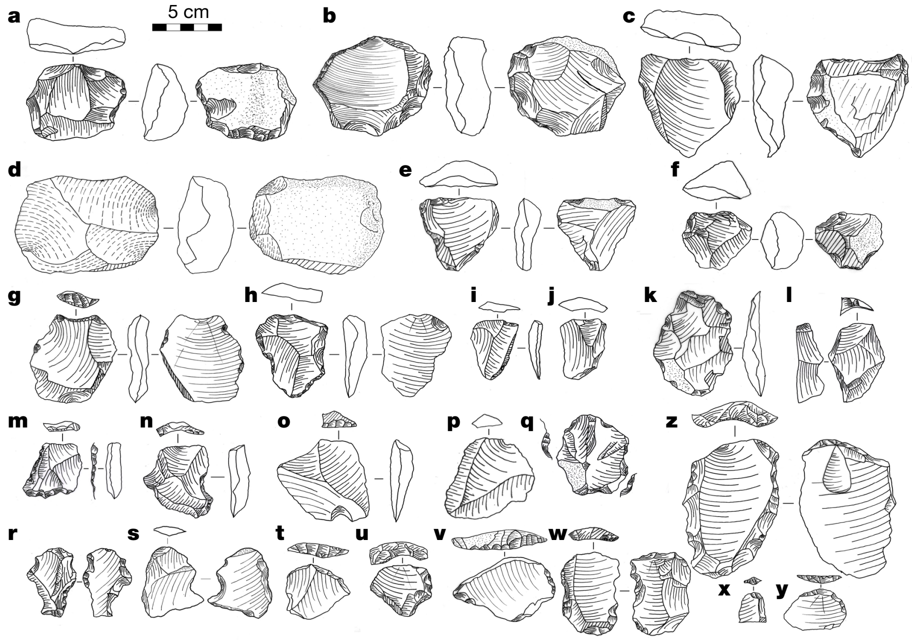

Fig. 3 | Line drawings of selected artefacts from Guanyindong Cave. **a**, **d**, **f**, Levallois recurrent cores. **b**, **c**, **e**, Levallois preferential cores. **g**–**k**, **n**, Levallois flakes. **l**, Débordant. **o**, **p**, Pseudo-Levallois points. **m**, **q**–**s**, Tools made on Levallois blanks. **t**–**z**, Flakes with prepared platforms. The photos of these artefacts are shown in Extended Data Figs. 5–7. The 3D structures of **a**–**c** are shown in the Supplementary Data. The artefacts shown in **b**, **c** and **q** were recovered from group A, and those shown in **r** and **s** were from group B.

4 tools made on Levallois flakes (Fig. 3 and Extended Data Figs. 5–7). Our technological reading of artefacts differs from previous studies, and in support of our analysis we provide three-dimensional models of three Levallois cores (shown in Fig. 3a–c) in the Supplementary Data. Eight cores exhibit patterns of recurrent Levallois concepts (Fig. 3a, d, f), each with two intersecting hierarchically organized surfaces. The upper surfaces of these cores are covered with several scars removed to form convexities that influence the pattern of detachment of the final flake. These scars come from different directions forming a centripetal scar pattern. The scars of the predetermined flakes are parallel to the plane of the intersection of upper and lower surface. The debitage surfaces of the cores have small flake scars along the edge, indicating preparation of their striking platforms. Three preferential Levallois cores are present (Fig. 3b, c, e), and are identifiable by the prominent large final flake detachments that have truncated the distal regions of the previous preparatory flake scars. The scars of the main flake removal on these cores are also parallel to the intersection of the upper and lower surfaces. The lower surfaces are extensively scarred and small platform preparation flake removals are present on the core circumference.

Many Levallois flakes at Guanyindong Cave exhibit a facetted platform, which results from core preparation before flake detachment. In addition, several smaller scars coming on to the dorsal surface of a flake from different directions are visible (Fig. 3g–k, n). These smaller scars may result from flaking to maintain the convexity of the core and in preparation for the removal of the Levallois flake. Four Levallois flakes were retouched along the edges (Fig. 3m, q–s). Besides these distinctive Levallois pieces, a number of non-Levallois flakes show signs of platform preparation (Fig. 3t–z), supporting the presence of more generalized strategies of prepared-core technology in Guanyindong Cave.

Levallois concepts at Guanyindong Cave first appeared in group B, which was dated to Marine Isotope Stage (MIS) 6 (approximately 180–130 ka), a period contemporary to the period during which Levallois technology was widely adopted in Africa and Eurasia[1]. Syntheses of globally distributed benthic $\delta^{18}O$ records indicate that MIS 6 was a glacial period of cooler temperatures and lower sea levels than at present[20]. Microscopic freeze–thaw features in the MIS 6 sediments from the nearby site Panxian Dadong (Fig. 2) suggest frequent freezing conditions during glacial periods, and the winter temperatures of this region during MIS 6 reached −5 °C or lower[21,22]. This evidence, together with the composition of the Panxian Dadong faunal assemblage, indicate a mixed woodland environment, including bamboo forests and open rocky areas with abundant grasses[21,22], suggesting that the landscape around Guanyindong Cave probably contained a reduced rainforest area compared to the present landscape, and a much-expanded open woodland environment.

The earliest age of the Guanyindong Cave lithic assemblage postdates the earliest modern human fossils in Africa[6,23] by 300–200 kyr and the Levant[24] by around 177–194 kyr, but predates any existing evidence of modern humans beyond this region during MIS 5 (around 130–80 ka), especially in south and southwest China[25,26]. With a secure age of approximately 170–80 kyr, the Levallois artefacts from Guanyindong Cave provide, to our knowledge, the earliest unequivocal evidence of prepared-core technology in east Asia, suggesting a geographically more widespread distribution of Levallois before the dispersal of *Homo sapiens*. This discovery has two important implications. First, the Guanyindong Cave assemblage suggests that demographic events may have occurred earlier in the Middle Pleistocene, leading to the appearance of Levallois concepts in east Asia. This possibility is suggested by the approximately 100 kyr-old Xuchang crania with its mosaic of Eurasian and Neanderthal features that indicate population interactions across Eurasia[27]. A Middle Pleistocene demographic event is also indicated by ancient DNA from the Late Pleistocene Tianyuan individual[28] that suggests that the divergence of Asians from Europeans occurred before 40 ka. Second, the emerging evidence of mode II bifacial tools from archaeological sites in east Asia[29,30] indicates that the prepared-core technologies from Guanyindong Cave, although rare, may alternatively represent a convergent technological evolution within the Acheulean technology of the same region. This challenges the existing hypotheses for the absence of Middle Pleistocene prepared-core technology in east Asia, including the idea that there was a lack of a strong ancestral Acheulean (mode II) tradition in this region and that local raw stone materials constrained tool-making to simple forms.

Given the absence of human fossils dated to the same period in southwest China, we can only speculate which species of hominin produced the Guanyindong Cave assemblage. Our findings, however, demonstrate a behavioural capacity compatible with their counterparts from the Western Hemisphere. The rarity of material traces of these complex behaviours in east Asia, relative to the Old World, therefore, may instead be due to the small, low-density populations with weak and/or irregular patterns of social interconnectedness in this region during the Middle Pleistocene. Under these conditions, technological innovation, transmission and persistence would have been rarer, compared to the high population and/or high density conditions of Middle Pleistocene sub-Saharan Africa, where Levallois is more abundant. Because Guanyindong Cave is one of only a few Palaeolithic sites that have been discovered in south China that are reliably dated to the late Middle Pleistocene, the abundance of mode III technology in this region remains an open question.

Online content

Any methods, additional references, Nature Research reporting summaries, source data, statements of data availability and associated accession codes are available at https://doi.org/10.1038/s41586-018-0710-1.

Received: 13 December 2017; Accepted: 26 September 2018;
Published online: 19 November 2018

1. Monnier, G. F. The Lower/Middle Paleolithic periodization in western Europe: an evaluation. *Curr. Anthropol*. **47**, 709–744 (2006).
2. Mcbrearty, S. & Brooks, A. S. The revolution that wasn't: a new interpretation of the origin of modern human behavior. *J. Hum. Evol*. **39**, 453–563 (2000).
3. Lycett, S. J. & Eren, M. I. Levallois lessons: the challenge of integrating mathematical models, quantitative experiments and the archaeological record. *World Archaeol*. **45**, 519–538 (2013).
4. Foley, R. & Lahr, M. M. Mode 3 technologies and the evolution of modern humans. *Camb. Archaeol. J*. **7**, 3–36 (1997).
5. Adler, D. S. et al. Early Levallois technology and the Lower to Middle Paleolithic transition in the Southern Caucasus. *Science* **345**, 1609–1613 (2014).
6. Tryon, C. A., McBrearty, S. & Texier, P.-J. Levallois lithic technology from the Kapthurin formation, Kenya: Acheulian origin and Middle Stone Age diversity. *Afr. Archaeol. Rev*. **22**, 199–229 (2005).
7. Akhilesh, K. et al. Early Middle Palaeolithic culture in India around 385–172 ka reframes Out of Africa models. *Nature* **554**, 97–101 (2018).
8. Boëda, E., Hou, Y. M., Forestier, H., Sarel, J. & Wang, H. M. Levallois and non-Levallois blade production at Shuidonggou in Ningxia, North China. *Quat. Int*. **295**, 191–203 (2013).
9. Li, F., Chen, F., Wang, Y. & Gao, X. Technology diffusion and population migration reflected in blade technologies in northern China in the Late Pleistocene. *Sci. China Earth Sci*. **59**, 1540–1553 (2016).
10. Brantingham, P. J., Olsen, J. W., Rech, J. A. & Krivoshapkin, A. I. Raw material quality and prepared core technologies in northeast Asia. *J. Archaeol. Sci*. **27**, 255–271 (2000).
11. Li, F. et al. The easternmost Middle Paleolithic (Mousterian) from Jinsitai Cave, North China. *J. Hum. Evol*. **114**, 76–84 (2018).
12. Seong, C. & Bae, C. J. The eastern Asian 'Middle Palaeolithic' revisited: a view from Korea. *Antiquity* **90**, 1151–1165 (2016).
13. Sato, H., Nishiaki, Y. & Suzuki, M. in *The Definition and Interpretation of Levallois Technology* (eds Dibble, H. L. & Bar-Yosef, O.) 485–500 (Prehistory Press, Madison, 1995).
14. Zwyns, N. in *Encyclopedia of Global Archaeology* (eds Gladyshev, S. et al.) 5025–5032 (Springer, New York, 2014).
15. Gao, X. & Norton, C. J. A critique of the Chinese 'Middle Palaeolithic'. *Antiquity* **76**, 397–412 (2002).
16. Li, Y. & Wen, B. *Guanyindong: A Lower Paleolithic Site at Qianxi County, Guizhou Province* (Cultural Relics Press, Beijing, China, 1986).
17. Shen, G. J. & Jin, L. H. U-series dating of speleothem samples from Guanyindong Cave at Qianxi County, Guizhou Province. *Acta Anthropologica Sinica* **11**, 93–100 (1992).
18. Yuan, S. X., Chen, T. M. & Gao, S. J. Uranium series chronological sequence of some Paleolithic sites in South China. *Acta Anthropologica Sinica* **5**, 179–190 (1986).
19. Grün, R., Eggins, S., Kinsley, L., Moseley, H., Sambridge, M. Laser ablation U-series analysis of fossil bones and teeth. *Palaeogeogr. Palaeoclimatol. Palaeoecol*. **416**, 150–167 (2014).
20. Lisiecki, L. E. & Raymo, M. E. A Pliocene–Pleistocene stack of 57 globally distributed benthic $\delta^{18}O$ records. *Paleoceanography* **20**, PA1003 (2005).
21. Wang, W. et al. Panxian Dadong, South China: establishing a record of Middle Pleistocene climatic changes. *Asian Perspect*. **43**, 302–313 (2004).
22. Karkanas, P., Schepartz, L. A., Miller-Antonio, S., Wang, W. & Huang, W. Late Middle Pleistocene climate in southwestern China: inferences from the stratigraphic record of Panxian Dadong Cave, Guizhou. *Quat. Sci. Rev*. **27**, 1555–1570 (2008).
23. Richter, D. et al. The age of the hominin fossils from Jebel Irhoud, Morocco, and the origins of the Middle Stone Age. *Nature* **546**, 293–296 (2017).
24. Hershkovitz, I. et al. The earliest modern humans outside Africa. *Science* **359**, 456–459 (2018).
25. Liu, W. et al. Human remains from Zhirendong, South China, and modern human emergence in East Asia. *Proc. Natl Acad. Sci. USA* **107**, 19201–19206 (2010).
26. Liu, W. et al. The earliest unequivocally modern humans in southern China. *Nature* **526**, 696–699 (2015).
27. Li, Z.-Y. et al. Late Pleistocene archaic human crania from Xuchang, China. *Science* **355**, 969–972 (2017).
28. Fu, Q. et al. DNA analysis of an early modern human from Tianyuan Cave, China. *Proc. Natl Acad. Sci. USA* **110**, 2223–2227 (2013).
29. Yamei, H. et al. Mid-Pleistocene Acheulean-like stone technology of the Bose basin, South China. *Science* **287**, 1622–1626 (2000).
30. Li, H., Kuman, K. & Li, C. What is currently (un)known about the Chinese Acheulean, with implications for hypotheses on the earlier dispersal of hominids. *C. R. Palevol*. **17**, 120–130 (2016).

Acknowledgements This work was supported by the Australian Research Council through Future Fellowships to B.L. (FT140100384) and B.M. (FT140100101), a grant from the National Science Foundation of China to J.-F.Z. (NSFC, 41471003), postgraduate scholarships from the University of Wollongong to Y.H. and X.R. and the China Scholarship Council to X.R. (201506010345), the Chinese Academy of Science (CAS) Strategic Priority Research Program Grants of 'Macroevolutionary Processes and Paleoenvironments of Major Historical Biota' (XDPB05), State Key Laboratory of Loess and Quaternary Geology, Institute of Earth Environment, CAS (SKLLQG1501) and National Science Foundation of China (41272033) to Y.-M.H. We thank S. Lin for assistance with artefact analysis and valuable comments on the manuscript; Y.-M. Hou for assistance with CT scanning on stone artefacts; R. G. Roberts, Z. Jacobs, Y. Jafari and T. Lachlan for support and assistance in the OSL laboratory; M. Otte and P. Zhang for valuable discussions on lithic assemblage; Y.-S. Lou, N. Ma, X.-W. Li and L. Lei for assistance with lithic observation.

Reviewer information *Nature* thanks C. A. Tryon and the other anonymous reviewer(s) for their contribution to the peer review of this work.

Author contributions B.L., Y.H., W.-W.H. and J.-F.Z. conceived and coordinated the study; Y.H., B.M. and J.-P.Y. conducted the stone artefact analysis; B.L., Y.H., J.-F.Z., W.-R.C., W.-W.H. and Y.-M.H. planned and directed field investigations and stratigraphic analysis. Y.H., B.L., J.-F.Z., X.R., W.-W.H. and Y.-M.H. collected samples for dating; Y.H., B.L., J.-F.Z. and X.R. measured OSL samples and analysed the dating results; B.M., B.L. and Y.H. wrote the manuscript, with contributions from the other authors.

Competing interests The authors declare no competing interests.

Additional information
Extended data is available for this paper at https://doi.org/10.1038/s41586-018-0710-1.
Supplementary information is available for this paper at https://doi.org/10.1038/s41586-018-0710-1.
Reprints and permissions information is available at http://www.nature.com/reprints.
Correspondence and requests for materials should be addressed to B.M. or B.L.
Publisher's note: Springer Nature remains neutral with regard to jurisdictional claims in published maps and institutional affiliations.

METHODS

Artefact analysis. The concept of Levallois has a variety of definitions, so here we survey the variation in the use of this concept to establish how we identified artefacts as Levallois in the Guanyindong assemblage. At the centre of most modern definitions of Levallois technology are six technological criteria[31]: (1) exploitation of the volume of raw material is organized in terms of two intersecting planes or flaking surfaces; (2) the two surfaces are hierarchically related, one constituting the striking platform and the other the primary reduction surface; (3) the primary reduction surface is shaped such that the morphology of the product is predetermined, which is fundamentally a function of the lateral and distal convexities of the surface; (4) the fracture plane for removing primary products is sub-parallel to the plane of intersection of the two surfaces; (5) the striking platform size and shape is adjusted to allow removal of flakes parallel to this plane, usually through retouch or faceting; and (6) Levallois flakes are removed by direct hard hammer percussion.

This reduction sequence concept is the prevailing definition of Levallois technology worldwide. As noted previously[32–34], there are many possible core morphologies that are consistent with these six criteria. The specific actions required to achieve these criteria, such as cortex trimming, platform faceting and edge preparation, may be applied in different proportions and at different stages in the life of a core. Further variability is evident in patterns of surface preparation and the orientation of flake removals. Among this variability, three patterns of Levallois reduction have been documented, including flakes removed from along the circumference of the core (centripetal or radial), from two directions (orthogonal or opposed) or one from only direction (unidirectional, parallel or convergent). Within these patterns there are two basic systems: preferential, in which only one large flake is produced per core preparation episode and recurrent, where several large flakes are removed between each core preparation episode[31].

These variations in technical attributes may result in a wide range of shapes, but this does not alter the fundamental model of Levallois reduction. This technical approach to defining and identifying Levallois technology differs from the older Bordesian typological concept of the Levallois. The Bordesian definition is based on the presence of specific, visually distinctive core and flake products, such as the classic turtle-shell core and large detached central flake (that is, preferential Levallois flake) that are often depicted in explanations of Levallois technology[35,36]. A key point of contrast in the two definitions is that for the first, the distinctive innovation in Levallois technology is the result of a process or sequence of actions that produces cores with a distinctive geometry, whereas for the latter, the distinctive idea is the systematic production of artefacts with predetermined, visually distinctive shapes. Predetermination is also important in the first scheme; however, the visual distinctiveness and morphology of the product is less important. The broader implications are similar, that the artefact maker used foresight and planning to create a stone artefact. But the implications for identifying a Levallois assemblage are substantially different. The first concept permits many different flaking strategies within the Levallois and a wide diversity in the form and character of flake products[37]. On the other hand, if we use the more strict Levallois definition, we are constrained to forms that match the Mousterian typology and similarly precise and delicate pieces.

One distinctive technological strategy that is common to both definitions of Levallois is the preparation of the core platform between each flake removal. This is a key point that separates Levallois from discoidal reduction, where there is no intervening phase of remodelling the core between flake removals, and an unhierarchical relation of the surfaces (but see a previous study[38] for some of the debates surrounding discoids and Levallois). Traces of core platform preparation are also important for identifying foresight and planning in stone artefact production, which is the key behavioural implication for early evidence of Levallois. Core preparation for removal of a target flake is also the main concept of mode III technologies, of which the Levallois is the most intensively studied and best known subset. However, evidence of core preparation, although behaviourally important, is not by itself sufficient to identify Levallois technology in an assemblage. Similarly, the hierarchical organization of the surfaces by itself, without signs of preparation, is not sufficient to identify Levallois. For example, Middle Pleistocene hierarchical cores that do not show maintenance of distal and lateral convexities, and only minimal treatment of the preparatory surface is conducted, mainly by large removals, are not identified as Levallois[39,40]. Flakes resulting from these cores tend to be flat in terms of ventral curvature, with mostly plain striking platforms, showing no signs of platform preparation.

We see in previous work that when traces of core preparation are present, as well as some of the six criteria, but the overall artefact morphology is not typical of the Mousterian typology, that researchers hesitate to use the term 'Levallois'. Instead they use terms such as 'proto-Levallois', 'stripped-down Levallois'[41], 'Levallois-like'[10,42–44], 'unsophisticated Levallois'[45], 'para-Levallois'[46,47] or 'reduced Levallois'[48]. These terms are most common when discussing assemblages at the early chronological extreme of the European Middle Palaeolithic or African Middle Stone Age, or at geographical extremes of the classic Levallois area, such as China. In many cases this nomenclature reflects either transitional technologies from simple prepared cores to 'full' Levallois with core preparation and hierarchical surfaces[41] or localized, independent convergences on Levallois technology that have no historical connection to the Bordesian core area of Levallois[49], or simply are pieces that are less intensely modified, representing initial phases of knapping[50]. This raises the question: what are the limits of the Levallois definition?

A particularly problematic detail in establishing the limits of the definition is the means by which the hierarchical relationship between the two core surfaces was established and how the platform was prepared to orient it perpendicular to the axis of flaking. It has previously been noted[32] that the previously published definition[31] gives little guidance on this. Several studies identify cores with a morphology of naturally asymmetric surfaces as Levallois, even though they lack the extensive flake removal to shape the core in preparation for the main flake removals[32,51–55]. Part of the problem here is the use of the six criteria as a checklist rather than a guide. Boëda himself follows the checklist approach and defines cores as non-Levallois when one criterion is absent[56]. In more recent research, we see a move away from this checklist system and instead the adoption of a more holistic approach, using the criteria as a guide[41,57,58].

We follow this more holistic approach, identifying the Levallois in the Guanyindong Cave assemblage as large and flat preferential flakes, sometimes showing faceted platforms, and cores with hierarchical relationships and preferential removals. We do not require traces of extensive shaping, instead following previous work that recognizes naturally asymmetric surfaces as compatible with an identification of Levallois technology. The detailed analysis of Levallois elements in Guanyindong Cave lithic and the previously published results are summarized in the Supplementary Information.

OSL dating. OSL dating provides an estimate of the time since mineral grains such as quartz or feldspars were last exposed to sunlight[59–61]. The burial age is estimated by dividing the equivalent dose (D_e, a measure of the radiation energy absorbed by grains during their period of burial) by the environmental dose rate (the rate of supply of ionizing radiation to the grains over the burial period). Here we determined the sedimentary ages of our sediment samples based on the measurements of the OSL from quartz.

A total of 13 sediment samples were collected for OSL dating from two residual profiles (S1 and S2) at the south wall of the cave entrance (Extended Data Fig. 2), including three samples from layer 1 at S1, four from layer 2 at S2, two from layer 4 at S1 and one from each of the layers 5–8 at S1 (Extended Data Figs. 3, 4). We did not take any sample from Layer 3, because we could not find suitable materials for dating from S1 (see Extended Data Fig. 3). The samples were collected by hammering opaque plastic tubes, each about 5 cm in diameter and around 25 cm long, into the cleaned section face. The tubes were sealed in black plastic bags for safe transport. Apart from the tubes, additional sediment at each sample location was collected and placed in plastic zip-lock bags for measuring their current moisture contents and radioactivity.

The sample tubes were opened and prepared under dim red light in the OSL dating laboratory at the University of Wollongong. The materials at both ends of each tube were discarded because they might have been exposed to sunlight at the time of sample collection. Because insufficient feldspar grains were extracted from our samples, only quartz grains were measured. Quartz grains were extracted using standard preparation procedures[62]. First, the samples were dissolved in 10% hydrochloric acid to remove carbonate before they were subsequently treated with 30% hydrogen peroxide solution to remove organic matter. The remaining sample was dried and then sieved to isolate grains of 90–125, 90–150, 90–180 and 180–212 μm in diameter. Quartz grains were separated from other minerals by density separation using sodium polytungstate solutions of 2.62 and 2.75 specific gravities. The separated quartz grains were etched with 48% hydrofluoric acid for around 40 min to remove the alpha-irradiated rind of each quartz grain and to destroy any remaining feldspars. The etched grains were then rinsed in hydrochloric acid to remove any precipitated fluorides, before being dried and sieved again. All of the samples were dominated by silt (<63 μm), and a limited amount of 180–212 μm quartz grains were extracted from our samples. Therefore, apart from the limited number of 180–212-μm grains, we also determined the D_e using smaller grains (in the range of 90–180 μm) for each sample.

The environmental dose rate for etched quartz is mainly attributable to beta and gamma radiation, from the decay of ^{238}U, ^{235}U, ^{232}Th (and their daughter products) and ^{40}K in the deposits surrounding the dated grains and cosmic rays. Beta dose rates were measured directly by low-level beta counting of dried, homogenized and powdered sediment samples from the dosimetry bags, using a GM-25-5 multi-counter system[63]. Gamma dose rates were measured at each sample location by an in situ gamma spectrometer, to account for any spatial heterogeneity in the gamma radiation field within 30 cm of each OSL sample. To accommodate the gamma detector, after removing the plastic sample tubes, we further drilled the holes to a depth of 30 cm using a hand auger. A two-inch (five-cm diameter) probe was inserted into the hole, and counts were collected for 60 min with a two-inch Na(Tl) crystal. The detector was calibrated using the concrete blocks at Oxford[64] and the gamma dose rate was determined using the 'threshold' technique[65]. The cosmic-ray dose rates were estimated according to a previously published method[66], based on the geomagnetic latitude and altitude of the Guanyindong site, as well as the thickness of sediment above each sample. Because our samples were collected from the cave entrance, we also allowed for the overhead limestone shielding and the configuration of the cave, by making a correction for the zenith angular distribution of cosmic rays[67]. We assigned a relative uncertainty of 10% to account for the systematic uncertainty in the primary cosmic-ray intensity. Because the cosmic ray constitutes only 1–5% of the total dose rate for these samples (Supplementary Table 5), the OSL ages are not highly sensitive to errors associated with the cosmic-ray dose rate.

Each of the measured beta and gamma dose rates and the calculated cosmic-ray dose rate were corrected for attenuation by water. For the samples from S1, the measured water contents of the six samples from group B range from 20% to 24% (with a mean value of 22%) (Supplementary Table 5), but lower values (11–17%) were obtained for the three samples from layer 1. By contrast, higher values (28–32%) were found for all the samples taken from group A at S2. The difference in the water contents between the two profiles is expected as S1 has been exposed for several decades after the last excavation in 1970s, so the measured present-day water contents should be underestimated. By contrast, S2 was protected by stones and covered by vegetation, which should retain water content better than S1. We, therefore, expect that the water content obtained from S2 is more representative to the long-term water content of S1. To assess the water content more reliably, we took additional sedimentary samples from two of the original trenches (profile 2a and 3) inside the cave, where moisture contents are also better retained. For the 15 samples (with burial depth ranging from around 50 to approximately 300 cm) that we measured, water contents ranged from 15 to 40%, and the mean and standard deviation were 30% and 8.5%, respectively. So, instead of using the in situ water content, we used a value of 30% as an estimate of the long-term water content for our OSL samples from groups A and B and a value of 20% for those from layer 1. We assigned a 25% relative standard error to these estimates, to accommodate any likely variations in the water content over the burial period. We noted that the measured in situ water contents are within the 2σ range of the assumed values.

OSL measurements were made on an automated Risø TL-DA-20 luminescence reader equipped with a single-grain laser (532 nm)[68]. Laboratory irradiations were carried out within the luminescence reader using a calibrated $^{90}Sr/^{90}Y$ beta source. All the quartz OSL measurements were made by mounting the grains onto standard Risø single-grain discs (gold-plated aluminium discs drilled with 100 holes that are each 300 mm in diameter and 300 mm deep)[69], where each grain hole contained one grain of 180–212 μm in diameter, or about eight grains of 90–125 μm in diameter. Spatial variation in the dose rate for individual grain positions was calibrated using gamma-irradiated quartz standards from the instrument manufacturer Risø. The ultraviolet OSL emissions were detected by an Electron Tubes 9235QA photomultiplier tube fitted with Hoya U-340 filters.

All OSL measurements were made using a single-aliquot regenerative-dose (SAR) procedure[70,71]. The SAR procedure involves measuring the OSL signals from the natural (burial) dose and from a series of regenerative doses, each of which was preheated at 240 °C for 10 s before optical stimulation by the green laser beam for 2 s at 125 °C. A fixed test dose (around 16 Gy) was given after each natural and regenerative dose, and the induced test-dose OSL signals were used to correct for any sensitivity changes during the SAR sequence. A cut heat to 180 °C was applied to the test dose. A duplicate regenerative dose was included in the procedure, to check on the validity of sensitivity correction, and a 'zero dose' measurement was made to monitor the extent of any 'recuperation' or 'thermal transfer' induced by the 240 °C preheating step. As a check on possible contamination from feldspars, we also applied the OSL infrared depletion-ratio test[72] at the end of the SAR sequence, using an infrared bleach of 40 s at 50 °C.

To test whether the SAR procedure is suitable for our samples, a dose-recovery test was conducted on sample GYD-OSL2 using different combinations of preheat/cutheat (260/180, 240/180, 220/180, 200/160 and 180/160 °C) temperatures. Two single-grain discs were measured for each preheat temperature using the grains of 90–125 μm diameter. The grains were bleached for approximately 30 min using a Dr Hönle solar simulator (model: UVACUBE 400). The bleached grains were then given a dose of around 100 Gy, before being measured using the SAR procedure using different preheat and cutheat temperatures. To select reliable single-grain D_e results, we applied several rejection criteria similar to those proposed previously[73]. Grains were rejected if they exhibited one or more of the following properties. (1) Test-dose signal (T_n) too dim, that is, the initial intensity is below the instrument detection limit (3σ below the background intensity) and/or the relative standard error on the test-dose measurement was more than 20%. (2) High levels of recuperation (that is, the ratio between the sensitivity-corrected OSL signals for the zero dose and the largest regenerative dose is higher than 5%). (3) Poor dose–response curve (DRC), that is, the regenerative signals are too scattered to be well-fitted with suitable functions (for example, a linear or saturating exponential function); note that poor recycling ratio falls into this category. (4) Natural OSL signal statistically equal to or greater than the saturation level of the corresponding DRC.

For each of the preheat temperatures, 39–64 grains were accepted after applying the above rejection criteria. The measured to given dose ratios (or dose-recovery ratios) are summarized as radial plots in Supplementary Fig. 1a–e for each of the preheat temperatures. We applied a central age model[70] to calculate the weighted mean recovery ratios for each preheat temperature, and these are shown in each of the radial plots[70,74]. The dose-recovery results are plotted against the preheat temperature in Supplementary Fig. 1f. The mean ratios are statistically consistent with unity at 1σ for the preheat temperatures at 220, 240 and 260 °C, which suggests that the chosen SAR procedures can accurately recover a known dose under these conditions.

On the basis of the dose-recovery tests, we chose the preheat/cutheat of 240/180 °C for measuring D_e values for all samples. Supplementary Fig. 1g, h shows the natural OSL decay curves of 10 grains each for GYD-OSL2 and GYD-OSL6. On the basis of the measurements from the 180–212-μm diameter grains, we found that the OSL intensity varies significantly from grain to grain, and most (around 90%) of the grains yielded no OSL signal at all (or their signal intensity was below the instrumental limit of detection); fewer than 5% of the measured single grains contributes >90% of the total OSL signal (Supplementary Fig. 1i). Apart from the OSL intensity, the DRCs from different grains also display a wide range of shapes associated with different saturation doses (Supplementary Figs. 1–20).

Depending on the availability of separated grains, 800–4,200 grains of 180–212 μm diameter were measured for GYD-OSL1, 2, 3, 5 and 6 (Supplementary Table 3). However, only about 2% of measured grains could pass the rejection criteria described above, and about 90% of the grains were rejected because the signals were too weak. For this reason, we measured smaller grains in the range of 90–180 μm for all of the samples. For the measurement of small grain size (<180 μm diameter) fractions, each grain hole of the standard single-grain disc may contain several grains (for example, up to eight grains of 90–125 μm diameter), which makes our measurements equivalent to a small aliquot that contains only a few grains. There are several advantages of measuring smaller grains. First, several grains were measured together in each of the holes, so there is a higher probability to find a bright grain in each hole, providing a considerable reduction in instrument time. Second, because of the low percentage (<5%) of bright grains in our samples, the measured OSL signal from each of the grain holes is expected to be dominated by only one or two grains, thereby effectively making these measurements equivalent to single-grain measurements. This is further confirmed by the similar results obtained from the 180–212-μm diameter grains and smaller grains (Supplementary Table 5). Using this method, 500–1,400 small aliquots were measured for each of the samples (Supplementary Table 3). As expected, the percentage of aliquots that have detectable OSL signals was significantly increased, ranging from 18% to 55%. About 20% of the small aliquots produced more than 80% of the total OSL signal (Supplementary Fig. 1i). Correspondingly, the proportion of grains that passed the rejection criteria was considerably increased (Supplementary Table 3).

The distributions of individual D_e values that passed the rejection criteria are shown in radial plots in Supplementary Fig. 2 for all of the samples. All of the samples show a large range in D_e values, ranging from around 0 to about 250 Gy. For those samples for which two grain sizes were measured, similar D_e distributions were observed between the two grain sizes from the same sample. These broad D_e distributions indicate that our samples were contaminated by 'younger' grains, especially in the case of the samples taken from S1. This is not surprising, because the residual profiles have been exposed for several decades since the last excavation in 1970s. As a result, one would expect some degree of bioturbation that could have intruded younger grains into the profiles. Evidence of such post-depositional mixture can be seen from the modern tree roots that penetrate deeply into the profile as shown in Extended Data Fig. 3. Fortunately, such recent bioactivity did not destroy the stratigraphic integrity of the residual profiles, because clear sedimentary beddings are still visible (Extended Data Figs. 3, 4) and these are consistent with the description in the original excavation report.

The numbers of grains or aliquots that were rejected based on each of the rejection criteria are summarized in Supplementary Table 3. There are considerable proportions of grains or aliquots (up to around 40%) that have saturated natural signals, for example, the L_n/T_n value is statistically consistent to or above the saturation level of the corresponding DRCs. As a result, finite D_e estimates cannot be obtained for these grains. Recent studies have suggested that rejecting a large number of 'saturated' grains may result in a significant underestimation of the final D_e estimate due to the truncation of the full D_e distribution[75–79]. To avoid this problem, a new method[80] has been proposed for the analysis of the L_n/T_n distribution and to establish standardized growth curves (SGCs)[81,82] for different grains or aliquots. Using this new method, no grains were rejected because they were 'saturated' and, therefore, a full and untruncated distribution of the L_n/T_n ratios was obtained, which enables reliable D_e estimation beyond the conventional limit of approximately $2D_0$ using the standard SAR procedure. Given the large proportion of 'saturated' grains in our samples, we therefore, applied this method[80] to estimate D_e values for our samples.

We first investigated the variability in the DRCs for our samples and the possibility of establishing SGCs following the previously proposed method[79]. By analysing the L_x/T_x ratios between two regenerative doses, it was previously[79] found that the single-grain and small-aliquot DRCs could be divided into three broad groups termed 'early', 'medium' and 'later', which saturated at different dose levels. It was also shown that each group could be well-defined by a SGC. As suggested previously[79], SGCs should be established using only those aliquots (grains) that are considered to be well-behaved so that reliable growth curves are produced. To do this, we first identified and rejected poorly behaved grains or aliquots using similar rejection criteria to those mentioned above but included all the 'saturated' ones. Supplementary Figure 3a shows comparisons of all the DRCs that pass the rejection criteria for the 90–150-μm quartz grains from GYD-OSL1. The DRCs from the same samples are highly variable among different grains or aliquots, which prevents the establishment of a common SGC. To test whether the samples can be classified into several groups that share the same DRCs, we calculated the ratios between the L_x/T_x values of two regenerative doses of around 280 and about 70 Gy, which reflects the saturation dose levels of the corresponding DRCs[79], for example, higher ratios represent larger saturation doses or later saturation. The ratios are shown in the radial plots in Supplementary Fig. 3b.

To test whether there are several groups that each have a similar saturation dose, we used a finite mixture model (FMM)[74,83,84] to identify the number of groups that have statistically indistinguishable L_x/T_x ratios and estimate the weighted mean ratios for each group and the probability of falling in each group for each grain or aliquot (Supplementary Fig. 3b). The DRCs from each group were analysed using a least-square normalization procedure[79] to establish corresponding SGCs for each of the groups (Supplementary Fig. 3c). The dose–response data from the same groups were fitted using a general-order kinetic function[85] of the form $f(x) = a(1-(1+bcx)^{(-1/c)}) + d$, where x is the dose and parameters a, b, c and d are constants. The different groups have considerably different saturation dose levels, that is, group 1 saturated at around 100 Gy, whereas group 3 showed no sign of saturation up to 500 Gy. The ratio between the measured L_x/T_x and the expected values based on the SGC are statistically consistent with unity for all of the groups; most of these ratios (around 90% or more) are consistent with unity at 2σ (Supplementary Fig. 3d–f), confirming the validity of the grouping and SGC establishment. The same procedure was applied to all of our samples, and we found that most of our samples could be fitted to 2–4 groups (Supplementary Figs. 3–20) despite the large variation in DRCs observed.

Once the SGCs were established for individual groups, the natural signals (L_n/T_n) from each of the groups were renormalized using the same scaling factors obtained during the least-square normalization procedure. The distributions of the least-square-normalized L_n/T_n values for each of the groups that were used to calculate final D_e values for each sample are shown in Supplementary Figs. 3–20 for all the samples. All groups were dominated by a single population, although most of them contain a few grains that have significantly smaller L_n/T_n values. This is similar to the patterns observed in the distribution of the SAR D_e values (Supplementary Fig. 2). However, because all of the grains that were rejected due to 'saturation' are included, it appears that all samples have a dominant population and this population has the highest L_n/T_n (or D_e) values. Therefore, we consider that the dominant population represents the true natural doses of the grains that remained intact since their burial.

The single-grain DRCs, SGCs and distribution of L_n/T_n values for individual groups of different samples are shown in Supplementary Figs. 3–20. For samples showing a single population of L_n/T_n values, we applied a central age model to estimate the weighted mean L_n/T_n values. For those with only a few young grains introduced, we identified and removed these outliers based on the median absolute deviation as a means of screening data for outliers[86,87]. For these cases, we calculated the normalized median absolute deviation using 1.4826 as the appropriate correction factor for a normal distribution, and rejected $\log(L_n/T_n)$ values with a normalized median absolute deviation greater than 1.5. For the other samples for which discrete D_e components could clearly be identified and are statistically supported, we applied the FMM to identify the number of populations for each distribution of least-square-normalized L_n/T_n and to calculate the central value of each population. The FMM was fitted by varying the common overdispersion value (σ_b) between 0 and 0.5 to find the optimum fit when the lowest Bayes Information score was reached[74,88]. The best-fit overdispersion values (or σ_b) for FMM fell within 0.1–0.2 for all samples. The best estimates of the least-square-normalized L_n/T_n for each group were then projected onto the corresponding SGCs to estimate their D_e. The D_e results for all of the samples are summarized in Supplementary Table 4. For some samples (for example, the 180–212 μm grains of sample GYD-OSL5), insufficient number of grains were accepted, so reliable results cannot be obtained. Group 1 (that is, the early saturated group) of most samples yielded infinite D_e values, because the L_n/T_n values were statistically within the saturation level of the corresponding SGC. However, finite results were obtained for the other groups that had higher saturation doses and their D_e values are statistically indistinguishable from each other for the same sample. For the samples for which two different grain sizes were measured, the D_e values from the two fractions were statistically consistent with each other. These results further confirm the validity of the grouping, SGC establishment and D_e estimates based on L_n/T_n and SGCs.

We estimated the D_e values for each grain size fraction of the samples based on the weighted mean of the results for the non-saturated DRC groups that produced finite D_e values. The final D_e and age estimates for the GYD samples are listed in Supplementary Table 5, together with the dose-rate estimates. For the samples for which two grain sizes were measured, the ages obtained from both grain sizes are consistent with each other within 1σ, further supporting our argument that the small-aliquot measurements are analogue to single-grain measurements. Therefore, for the samples for which two different grain sizes were measured, we estimated their ages based on the weighted mean of the ages obtained from the two grain sizes. The final age estimates for all the samples are shown in Fig. 2 and Supplementary Table 5.

Our OSL chronology provides a firm constraint on the sedimentary ages of the artefact-bearing deposits from layer 1, groups A and B. The OSL age for the sample from layer 6 is consistent with the U-series age (around 180 kyr) of the stalagmite sample taken from the same layer (Supplementary Table 1), confirming the reliability of both dates. On the basis of the new OSL ages and previous U-series dating results (see Supplementary Information for a full discussion on U-series results), we conclude that layer 2 (group A) was deposited around 80–90 ka, corresponding to the last interglacial period or MIS 5a. Our age estimate for group A is further supported by sedimentary features. The deposits of group A consist of reddish clay and are indicative of strong paedogenesis process taking place during warm and humid interglacial conditions. The poorly preserved fossils in group A, compared to those in group B, further support that the depositional environment of group A was relatively warm and humid. Layers 4–8 (group B) were deposited between 160 and 170 ka. The age of the Guanyindong lithic assemblage can, therefore, be safely constrained to between approximately 170 and 80 ka.

Code availability. All custom R scripts used to produce the results presented here are available online at https://doi.org/10.17605/OSF.IO/ERNTJ.

Reporting summary. Further information on research design is available in the Nature Research Reporting Summary linked to this paper.

Data availability

All data are available from the corresponding authors upon reasonable request.

31. Boëda, E. in *The Definition and Interpretation of Levallois Technology* (eds Dibble, H. & Bar-Yosef, O.) 41–68 (Prehistory Press, Madison, 1995).
32. Brantingham, P. J. & Kuhn, S. L. Constraints on Levallois core technology: a mathematical model. *J. Archaeol. Sci*. **28**, 747–761 (2001).
33. Eren, M. I. & Lycett, S. J. Why Levallois? A morphometric comparison of experimental 'preferential' Levallois flakes versus debitage flakes. *PLoS ONE* **7**, e29273 (2012).
34. White, M., Ashton, N. & Scott, B. in *The Ancient Human Occupation of Britain* (eds Ashton, N. et al.) 53–66 (Elsevier, Amsterdam, 2011).
35. Van Peer, P. *The Levallois reduction strategy* (Prehistory Press, Madison, 1992).
36. Schlanger, N. Understanding Levallois: lithic technology and cognitive archaeology. *Camb. Archaeol. J*. **6**, 231–254 (1996).
37. Mellars, P. A. *The Neanderthal Legacy: An Archaeological Perspective from Western Europe* (Princeton Univ. Press, Princeton, 1995).
38. Monnier, G. F. & Missal, K. Another Mousterian Debate? Bordian facies, chaîne opératoire technocomplexes, and patterns of lithic variability in the western European Middle and Upper Pleistocene. *Quat. Int*. **350**, 59–83 (2014).
39. Malinsky-Buller, A. The muddle in the Middle Pleistocene: the Lower–Middle Paleolithic transition from the Levantine perspective. *J. World Prehist*. **29**, 1–78 (2016).
40. Barzilai, O., Malinsky-Buller, A. & Ackermann, O. Kefar Menachem West: a Lower Paleolithic site in the southern Shephela, Israel. *J. Israel Prehist. Soc*. **36**, 7–38 (2006).
41. White, M. & Ashton, N. Lower Palaeolithic core technology and the origins of the Levallois method in north-western Europe. *Curr. Anthropol*. **44**, 598–609 (2003).
42. Niu, D. et al. The initial Upper Palaeolithic in northwest China: new evidence of cultural variability and change from Shuidonggou locality 7. *Quat. Int*. **400**, 111–119 (2016).
43. Shimelmitz, R., Weinstein-Evron, M., Ronen, A. & Kuhn, S. L. The Lower to Middle Paleolithic transition and the diversification of Levallois technology in the Southern Levant: evidence from Tabun Cave, Israel. *Quat. Int*. **409**, 23–40 (2016).
44. Brantingham, P. J., Kuhn, S. L. & Kerry, K. W. *The Early Upper Paleolithic beyond Western Europe* (California Univ. Press, 2004).
45. Cahen, D. Les industries préhistoriques des nappes alluviales de Petit-Spiennes et de Mesvin. *Notae Praehistoricae* **1**, 70–74 (1981).
46. Cahen, D., Haesaerts, P. & Watteyne, D. La nappe alluviale de Petit-Spiennes et le début du débitage levallois dans la vallée de la Haine. *Archaeologia Belgica Bruxelles* **1**, 7–16 (1985).

47. Watteyne, D. Petit-Spiennes: industrie (s) a débitage Levallois et para-Levallois. *Notae Praehistoricae* **5**, 95–104 (1985).
48. Roe, D. A. *The Lower and Middle Palaeolithic Periods in Britain Vol*. **46** (Routledge, London, 2014).
49. Otte, M. in *The Definition and Interpretation of Levallois technology* (eds Dibble, H. & Bar-Yosef, O.) 117–124 (Prehistory Press, Madison, 1995).
50. Ryssaert, C. Some new insights in an old collection: lithic technology at Mesvin IV. *Notae Praehistoricae* **26**, 91–99 (2006).
51. Kuhn, S. L. *Mousterian Lithic Technology* (Princeton Univ. Press, Princeton, 1995).
52. Delagnes, A. in *The Definition and Interpretation of Levallois technology Monographs in World Archaeology* Vol. 23 (eds Bar-Yosef, O. & Dibble, H.) 201–212 (Prehistory Press, Madison, 1995).
53. Chazan, M. Redefining Levallois. *J. Hum. Evol*. **33**, 719–735 (1997).
54. Picin, A. Technological adaptation and the emergence of Levallois in Central Europe: new insight from the Markkleeberg and Zwochau open-air sites in Germany. *J. Quat. Sci*. **33**, 300–312 (2018).
55. Boëda, E. & Pelegrin, J. Approche technologique du nucleus levallois a éclat. *Etudes Préhistoriques Lyon* **15**, 41–48 (1979).
56. Boëda, E. Approche technologique du concept Levallois et évaluation de son champ d'application: étude de trois gisement saaliens et weichseliens de la France septentrionale. PhD thesis, Université de Paris X (1986).
57. Scott, R. The Early Middle Palaeolithic of Britain; origins, technology and landscape. PhD thesis, Durham University (2006).
58. Bolton, L. Assessing the Origins of Levallois through Lower Palaeolithic Core Variation: A Comparative Study of Simple Prepared Cores in Northwest Europe. PhD thesis, University of Southampton (2015).
59. Huntley, D. J., Godfrey-Smith, D. I. & Thewalt, M. L. W. Optical dating of sediments. *Nature* **313**, 105–107 (1985).
60. Aitken, M. J. *An Introduction to Optical Dating* (Oxford Univ. Press, Oxford, 1998).
61. Roberts, R. G. et al. Optical dating in archaeology: thirty years in retrospect and grand challenges for the future. *J. Archaeol. Sci*. **56**, 41–60 (2015).
62. Wintle, A. G. Luminescence dating: laboratory procedures and protocols. *Radiat. Meas*. **27**, 769–817 (1997).
63. Bøtter-Jensen, L. & Mejdahl, V. Assessment of beta dose-rate using a GM multicounter system. *Int. J. Rad. Appl. Instrum. D* **14**, 187–191 (1988).
64. Rhodes, E. J. & Schwenninger, J.-L. Dose rates and radioisotope concentrations in the concrete calibration blocks at Oxford. *Ancient TL* **25**, 5–8 (2007).
65. Mercier, N. & Falguères, C. Field gamma dose-rate measurement with a NaI(Tl) detector: re-evaluation of the "threshold" technique. *Anc. TL* **25**, 1–4 (2007).
66. Prescott, J. R. & Hutton, J. T. Cosmic-ray contributions to dose rates for luminescence and ESR dating: large depths and long-term time variations. *Radiat. Meas*. **23**, 497–500 (1994).
67. Smith, M. A., Prescott, J. R. & Head, M. J. Comparison of ^{14}C and luminescence chronologies at Puritjarra rock shelter, central Australia. *Quat. Sci. Rev*. **16**, 299–320 (1997).
68. Bøtter-Jensen, L., Andersen, C. E., Duller, G. A. T. & Murray, A. S. Developments in radiation, stimulation and observation facilities in luminescence measurements. *Radiat. Meas*. **37**, 535–541 (2003).
69. Bøtter-Jensen, L., Bulur, E., Duller, G. A. T. & Murray, A. S. Advances in luminescence instrument systems. *Radiat. Meas*. **32**, 523–528 (2000).
70. Galbraith, R. F., Roberts, R. G., Laslett, G. M., Yoshida, H. & Olley, J. M. Optical dating of single and multiple grains of quartz from Jinmium rock shelter, northern Australia: part 1, experimental design and statistical models. *Archaeometry* **41**, 339–364 (1999).
71. Murray, A. S. & Wintle, A. G. Luminescence dating of quartz using an improved single-aliquot regenerative-dose protocol. *Radiat. Meas*. **32**, 57–73 (2000).
72. Duller, G. A. T. Distinguishing quartz and feldspar in single grain luminescence measurements. *Radiat. Meas*. **37**, 161–165 (2003).
73. Jacobs, Z., Duller, G. A. T. & Wintle, A. G. Interpretation of single grain D_e distributions and calculation of D_e. *Radiat. Meas*. **41**, 264–277 (2006).
74. Galbraith, R. F. & Roberts, R. G. Statistical aspects of equivalent dose and error calculation and display in OSL dating: an overview and some recommendations. *Quat. Geochronol*. **11**, 1–27 (2012).
75. Gliganic, L. A., Jacobs, Z., Roberts, R. G., Domínguez-Rodrigo, M. & Mabulla, A. Z. P. New ages for Middle and Later Stone Age deposits at Mumba rockshelter, Tanzania: optically stimulated luminescence dating of quartz and feldspar grains. *J. Hum. Evol*. **62**, 533–547 (2012).
76. Duller, G. A. T. Improving the accuracy and precision of equivalent doses determined using the optically stimulated luminescence signal from single grains of quartz. *Radiat. Meas*. **47**, 770–777 (2012).
77. Thomsen, K. J. et al. Testing single-grain quartz OSL methods using sediment samples with independent age control from the Bordes-Fitte rockshelter (Roches d'Abilly site, Central France). *Quat. Geochronol*. **31**, 77–96 (2016).
78. Guo, Y.-J. et al. New ages for the Upper Palaeolithic site of Xibaimaying in the Nihewan Basin, northern China: implications for small-tool and microblade industries in north-east Asia during Marine Isotope Stages 2 and 3. *J. Quat. Sci*. **32**, 540–552 (2017).
79. Li, B., Jacobs, Z. & Roberts, R. G. Investigation of the applicability of standardised growth curves for OSL dating of quartz from Haua Fteah cave, Libya. *Quat. Geochronol*. **35**, 1–15 (2016).
80. Li, B., Jacobs, Z., Roberts, R. G., Galbraith, R. & Peng, J. Variability in quartz OSL signals caused by measurement uncertainties: problems and solutions. *Quat. Geochronol*. **41**, 11–25 (2017).
81. Roberts, H. M. & Duller, G. A. T. Standardised growth curves for optical dating of sediment using multiple-grain aliquots. *Radiat. Meas*. **38**, 241–252 (2004).
82. Li, B., Roberts, R. G., Jacobs, Z. & Li, S. H. Potential of establishing a 'global standardised growth curve' (gSGC) for optical dating of quartz from sediments. *Quat. Geochronol*. **27**, 94–104 (2015).
83. Roberts, R. G., Galbraith, R. F., Yoshida, H., Laslett, G. M. & Olley, J. M. Distinguishing dose populations in sediment mixtures: a test of single-grain optical dating procedures using mixtures of laboratory-dosed quartz. *Radiat. Meas*. **32**, 459–465 (2000).
84. Galbraith, R. F. & Green, P. F. Estimating the component ages in a finite mixture. *Int. J. Rad. Appl. Instrum. D* **17**, 197–206 (1990).
85. Guralnik, B. et al. Radiation-induced growth and isothermal decay of infrared-stimulated luminescence from feldspar. *Radiat. Meas*. **81**, 224–231 (2015).
86. Rousseeuw, P. J. & Croux, C. Alternatives to the median absolute deviation. *J. Am. Stat. Assoc*. **88**, 1273–1283 (1993).
87. Rousseeuw, P. J., Debruyne, M., Engelen, S. & Hubert, M. Robustness and outlier detection in chemometrics. *Crit. Rev. Anal. Chem*. **36**, 221–242 (2006).
88. Arnold, L. J. & Roberts, R. G. Stochastic modelling of multi-grain equivalent dose (D_e) distributions: implications for OSL dating of sediment mixtures. *Quat. Geochronol*. **4**, 204–230 (2009).

a

b

Extended Data Fig. 1 | Photos showing the landscape and location of the Guanyindong Cave. a, Southward view of the Guanyindong Cave. **b**, The main entrance of the cave.

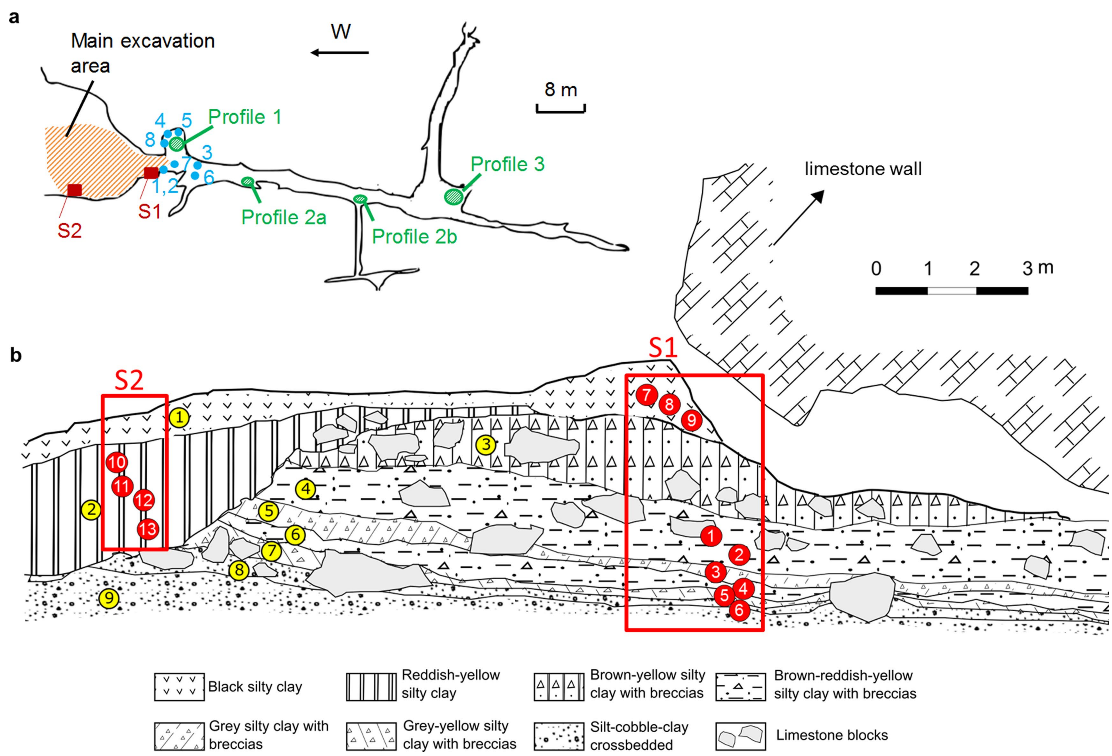

Extended Data Fig. 2 | Plan view and stratigraphy of the Guanyindong Cave. **a**, Plan view of the cave, main excavation area and the residual profiles from the south wall. The blue dots and the numbers next to each of the dots represent the locations of U-series dating samples have been taken previously[17] (see Supplementary Information for discussion of the U-series results); sample codes from 1 to 8 are QGC-19-1, QGC-19-2, QGC-4, QGC-21, QGB-4, QGC-7 and QGC-23, respectively. The green circles are the locations of profiles 1, 2a, 2b and 3. The red squares show the locations of the residual profiles S1 and S2, where the OSL samples were taken. **b**, Detail of the numbered stratigraphic layers at the main entrance of the cave. The stratigraphic layer numbers are shown in yellow circles. The red rectangles show the locations of the two south-wall sections (S1 and S2) where OSL samples were taken. The locations of OSL samples are shown in red circles, with the sample code shown inside (for example, number 1 represents GYD-OSL1; see Extended Data Figs. 3, 4 for more details). **a**, **b**, Images were adapted from a previous study[16], copyright 1986.

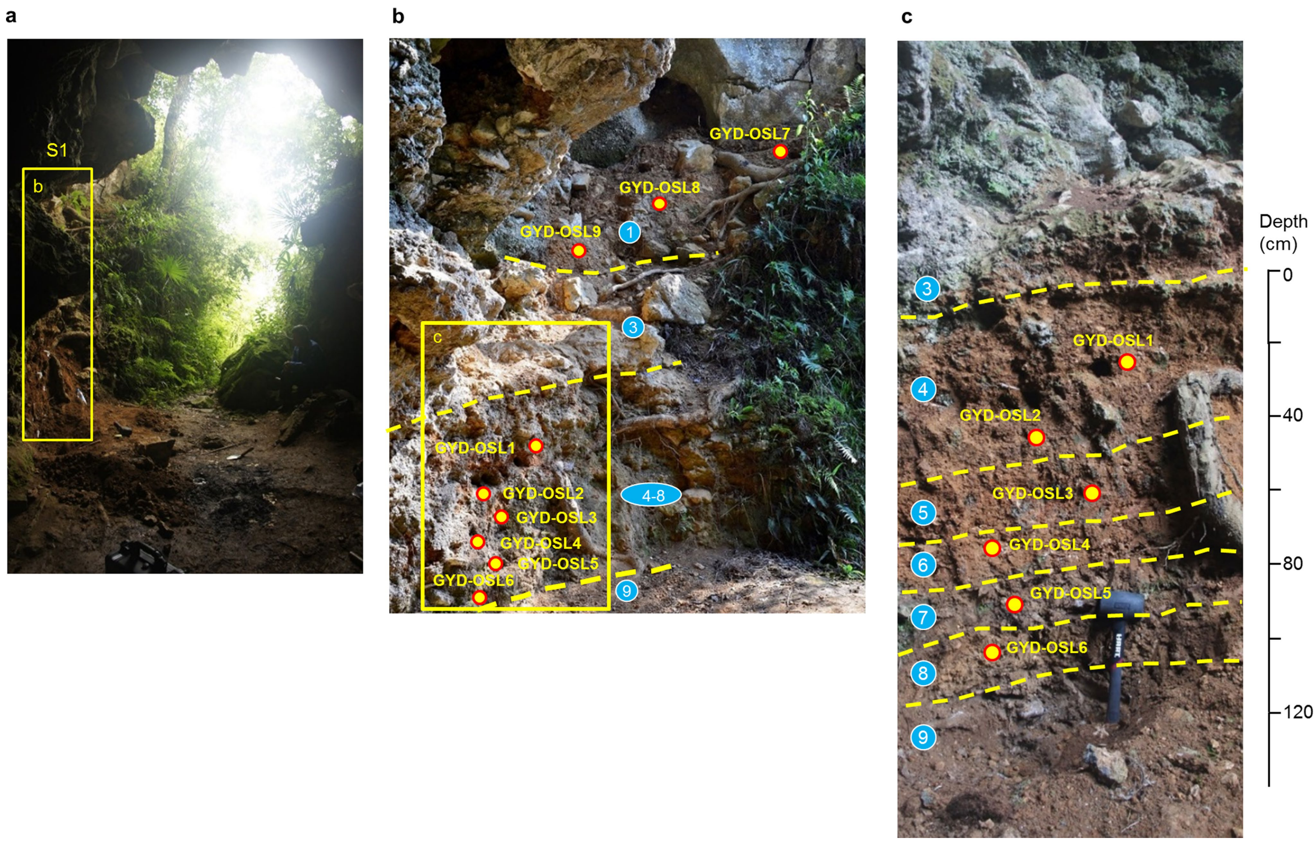

Extended Data Fig. 3 | General view of the residual profile S1 from the cave entrance. a, Photo taken from the interior of the cave, showing the location of the residual profile S1 at the south wall (marked by a rectangle with details shown in **b** and **c**). **b**, Photo showing details of the residual profile S1 at the south wall and the location of all OSL samples from layer 1 and layers 4–8. The details of layers 3–9 inside the yellow rectangle are shown in **c**. **c**, Photo showing the details of sedimentary layers 3–9 of group B, and the location of OSL samples. The stratigraphic layer numbers are shown in blue circles and the location of OSL samples are marked by yellow circles with sample names shown next to each of them. The dashed yellow lines in **b** and **c** show the boundaries between the layers.

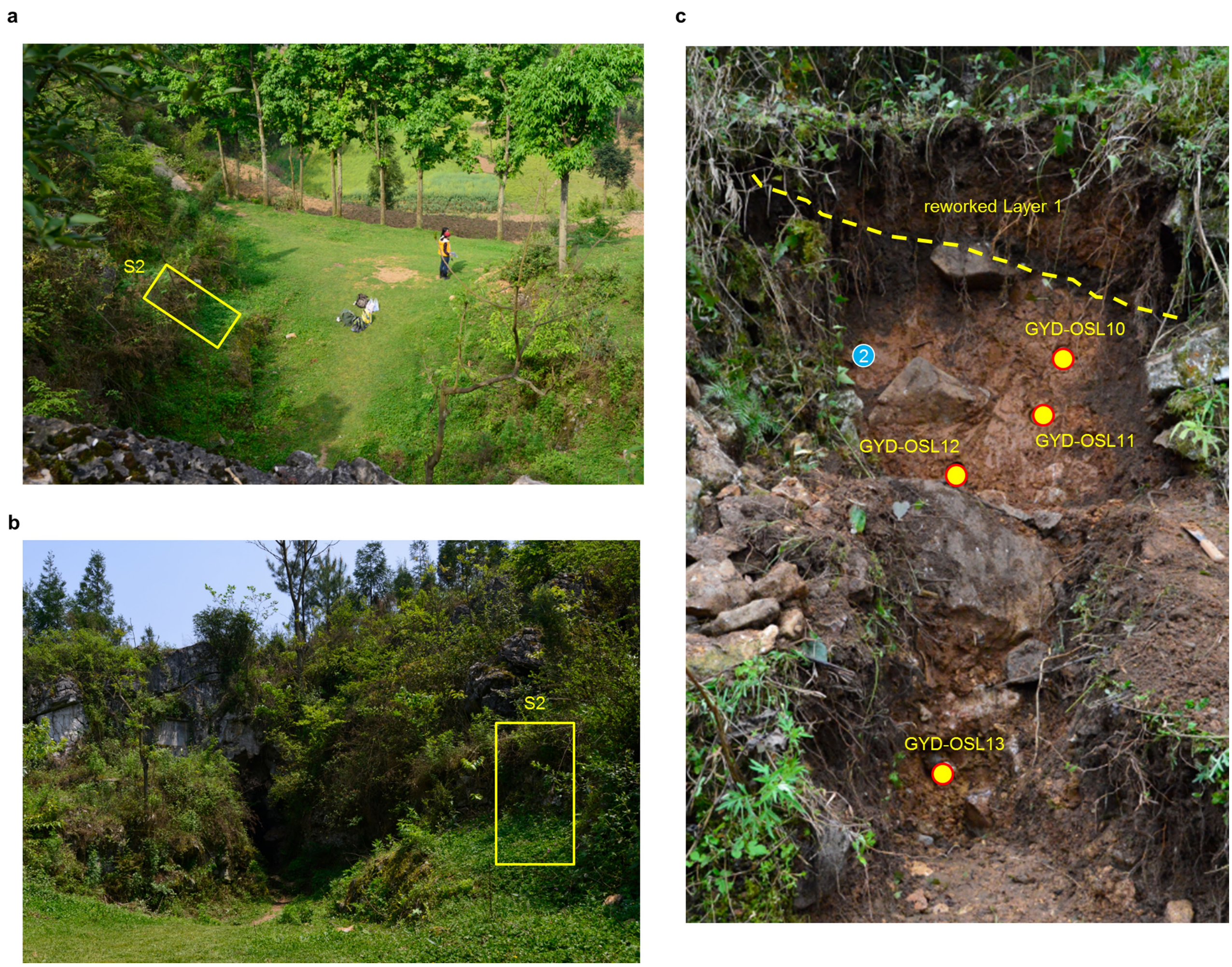

Extended Data Fig. 4 | General view of the residual profile S2 outside the cave entrance. **a**, Photo taken from top of the cave, showing the location of the residual profile S2 (indicated by the rectangle). **b**, Photo taken from outside the cave, showing the location of the residual profile S2 (indicated by the rectangle). **c**, Photo showing the details of sedimentary layers (layer 2 and reworked layer 1) of residual profile S2, and the location of OSL samples. The dashed yellow line shows the boundary between layers 1 and 2. The stratigraphic layer numbers are shown in blue circles and the location of OSL samples are marked by yellow circles with sample names shown next to each of them.

Extended Data Fig. 5 | Photographs of selected Levallois cores. **a**, **d**, **f**, Levallois recurrent cores. **b**, **c**, **e**, Levallois preferential cores. The line drawings of these artefacts are shown in Fig. 3a–f. The artefacts shown in **b** and **c** were recovered from group A.

Extended Data Fig. 6 | Photographs of selected Levallois flakes and tools. g–k, **n**, Levallois flakes. **l**, Débordant. **m**, Tools made on Levallois blanks. **o**, **p**, Pseudo-Levallois points. The line drawings of these artefacts are shown in Fig. 3g–p.

Extended Data Fig. 7 | Photographs of selected Levallois tools and flakes with prepared platform. q–s, Tools made on Levallois blanks. **t–z**, Flakes with prepared platforms. The line drawings of these artefacts are shown in Fig. 3q–z. The artefact shown in **q** was recovered from group A, and those shown in **r** and **s** were from group B.

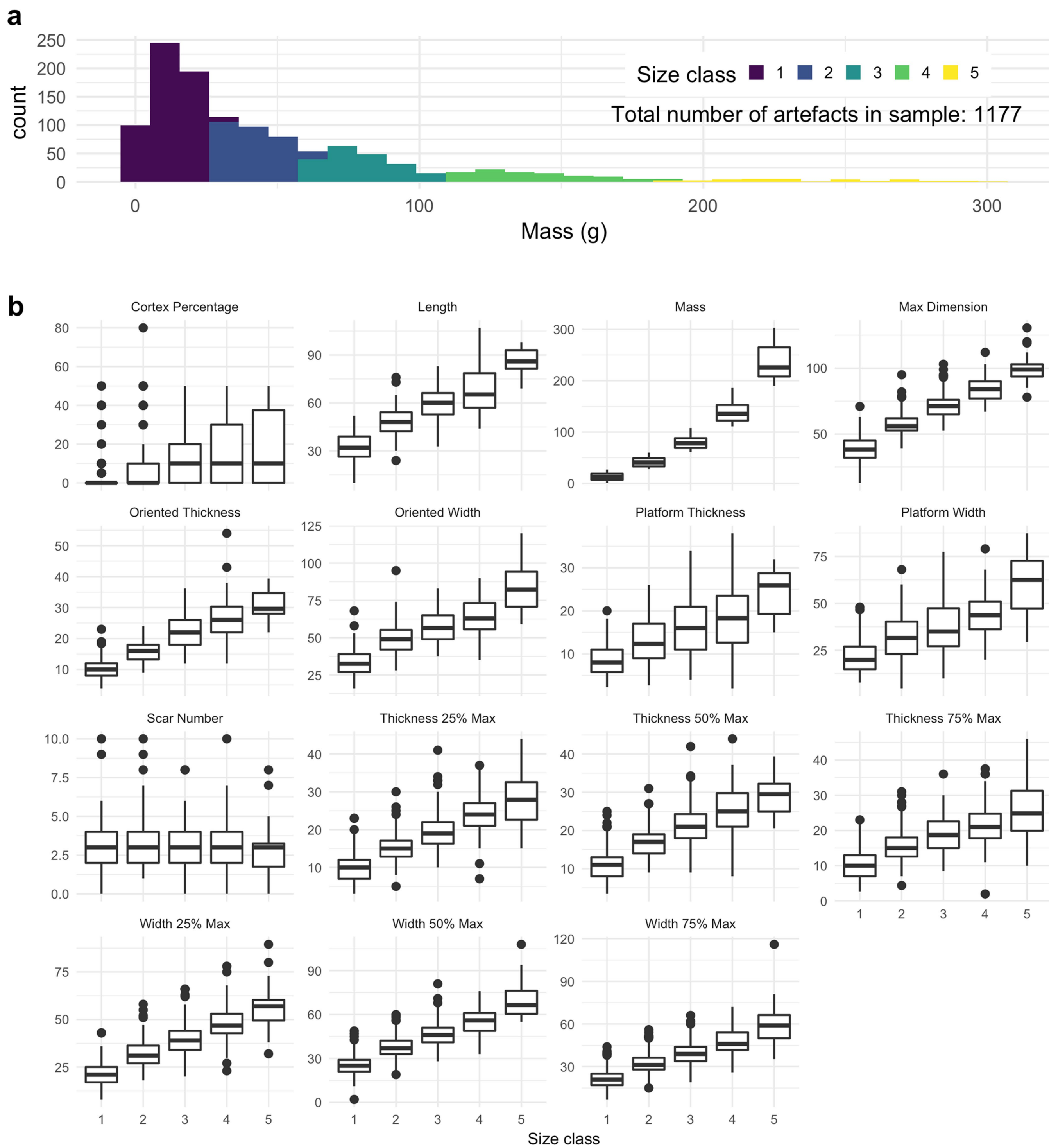

Extended Data Fig. 8 | Distributions of metric variables on flakes. **a**, Histogram of flake lengths, coloured by size class. **b**, Box-and-whisker plots of a selection of metric variables to show technological variation across the size classes to reveal the lithic reduction sequence ($n = 1,177$ flakes). Centre lines show data median, boxes show first and third quartiles (the 25th and 75th percentiles), and the whiskers extend from the upper and lower hinge to the largest and smallest values that are no further than 1.5 times the interquartile range from the hinge (which is the distance between the first and third quartiles). Data beyond the end of the whiskers are outlying points and are plotted individually. Linear dimensions are measured in mm, mass in g.

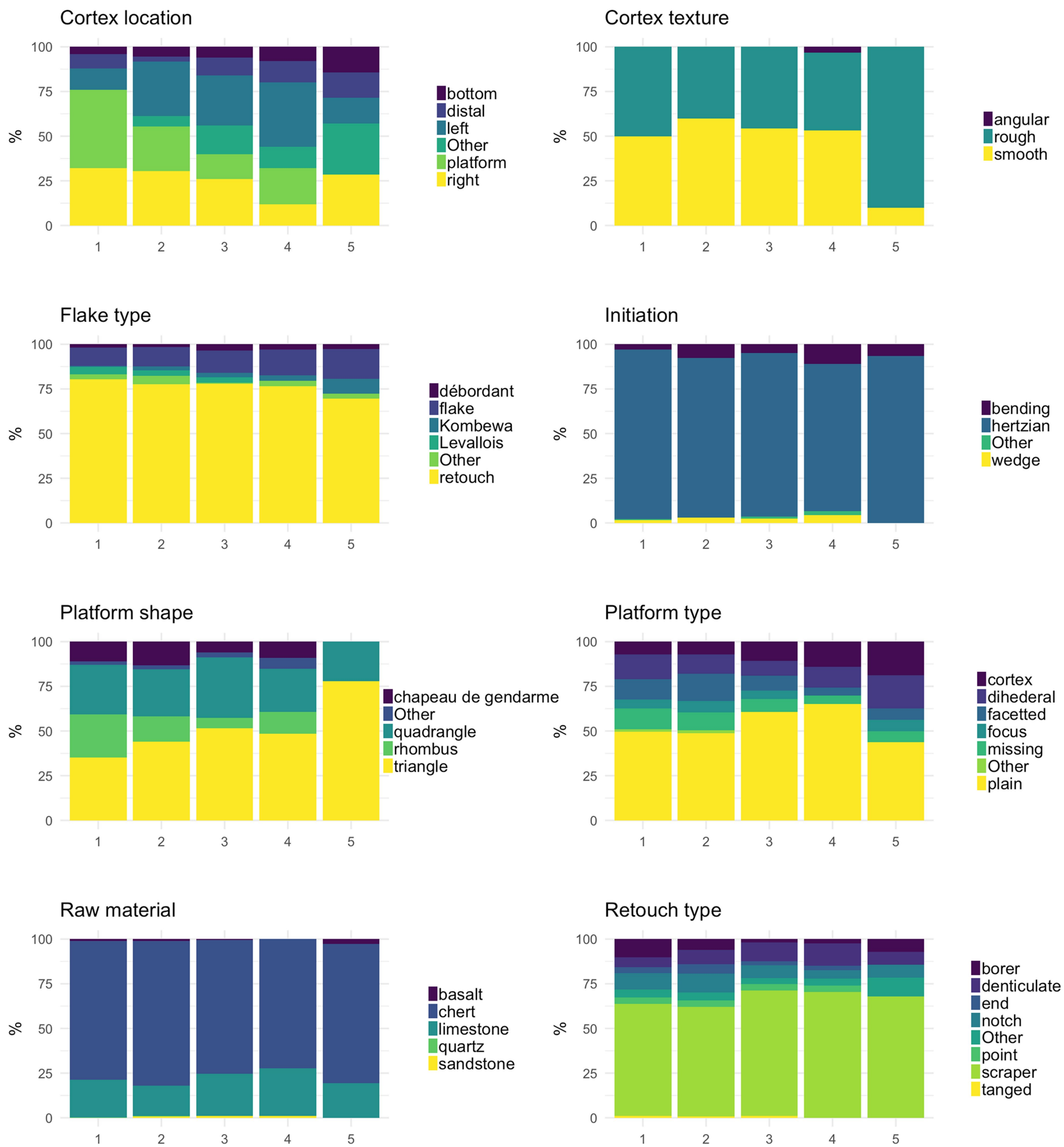

Extended Data Fig. 9 | Distributions of technological attributes of flakes across the five size classes. $n = 1{,}177$ flakes.

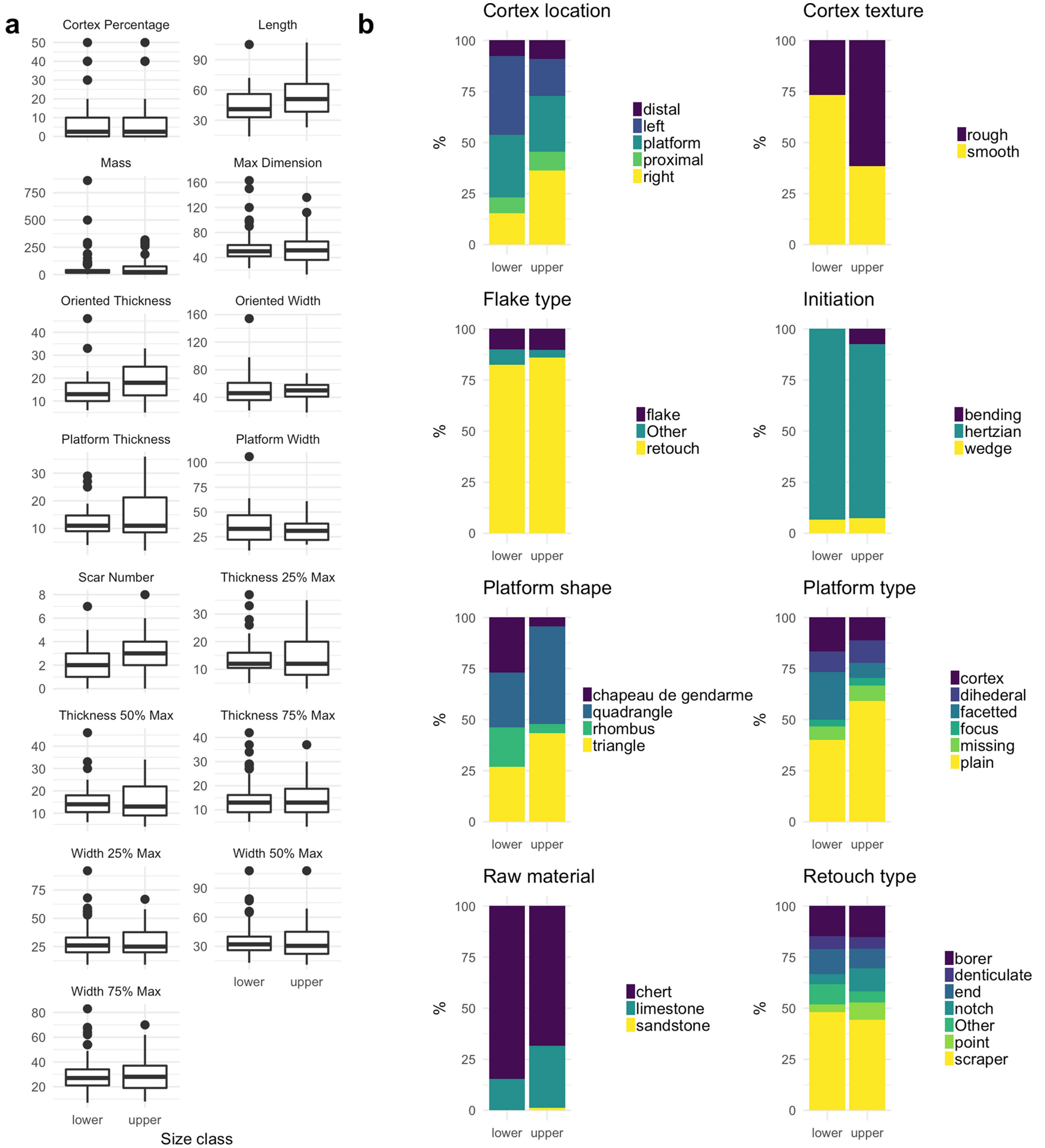

Extended Data Fig. 10 | Comparison of flakes from the upper (group A) and lower (group B) layers of the deposit ($n = 204$), with 117 pieces from the lower layers (dated to 170–160 ka) and 87 from the upper layer (dated to approximately 90–80 ka). a, Metric variables. Linear dimensions are measured in mm, mass in g. **b**, Technological variables. Centre lines show data median, boxes show first and third quartiles (the 25th and 75th percentiles), and the whiskers extend from the upper and lower hinge to the largest and smallest values no further than 1.5 times the interquartile range from the hinge. Data beyond the end of the whiskers are outlying points and are plotted individually.

nature research

Corresponding author(s): Bo Li

Reporting Summary

Nature Research wishes to improve the reproducibility of the work that we publish. This form provides structure for consistency and transparency in reporting. For further information on Nature Research policies, see Authors & Referees and the Editorial Policy Checklist.

Statistical parameters

When statistical analyses are reported, confirm that the following items are present in the relevant location (e.g. figure legend, table legend, main text, or Methods section).

n/a	Confirmed	
☐	☒	The exact sample size (n) for each experimental group/condition, given as a discrete number and unit of measurement
☐	☒	An indication of whether measurements were taken from distinct samples or whether the same sample was measured repeatedly
☐	☒	The statistical test(s) used AND whether they are one- or two-sided *Only common tests should be described solely by name; describe more complex techniques in the Methods section.*
☒	☐	A description of all covariates tested
☒	☐	A description of any assumptions or corrections, such as tests of normality and adjustment for multiple comparisons
☐	☒	A full description of the statistics including central tendency (e.g. means) or other basic estimates (e.g. regression coefficient) AND variation (e.g. standard deviation) or associated estimates of uncertainty (e.g. confidence intervals)
☒	☐	For null hypothesis testing, the test statistic (e.g. F, t, r) with confidence intervals, effect sizes, degrees of freedom and P value noted *Give P values as exact values whenever suitable.*
☒	☐	For Bayesian analysis, information on the choice of priors and Markov chain Monte Carlo settings
☒	☐	For hierarchical and complex designs, identification of the appropriate level for tests and full reporting of outcomes
☒	☐	Estimates of effect sizes (e.g. Cohen's d, Pearson's r), indicating how they were calculated
☐	☒	Clearly defined error bars *State explicitly what error bars represent (e.g. SD, SE, CI)*

Our web collection on statistics for biologists may be useful.

Software and code

Policy information about availability of computer code

Data collection	Analyst (Risoe OSL/TL customised software for OSL analysis), Excel
Data analysis	Analyst (Risoe OSL/TL customised software for OSL analysis), Excel, R-studio (R code available in Github, link provided in ms)

For manuscripts utilizing custom algorithms or software that are central to the research but not yet described in published literature, software must be made available to editors/reviewers upon request. We strongly encourage code deposition in a community repository (e.g. GitHub). See the Nature Research guidelines for submitting code & software for further information.

Data

Policy information about availability of data

All manuscripts must include a data availability statement. This statement should provide the following information, where applicable:

- Accession codes, unique identifiers, or web links for publicly available datasets
- A list of figures that have associated raw data
- A description of any restrictions on data availability

All custom R scripts used to produce the results presented here is available online at http://doi.org/10.17605/OSF.IO/ERNTJ. All other relevant data are available from the corresponding authors on request.

Field-specific reporting

Please select the best fit for your research. If you are not sure, read the appropriate sections before making your selection.

☐ Life sciences ☐ Behavioural & social sciences ☒ Ecological, evolutionary & environmental sciences

For a reference copy of the document with all sections, see nature.com/authors/policies/ReportingSummary-flat.pdf

Ecological, evolutionary & environmental sciences study design

All studies must disclose on these points even when the disclosure is negative.

Study description	Chronology and lithic study of a Paleolithic site in southwest China
Research sample	Samples include 13 sedimentary samples for OSL dating, and over 2000 stone tools for lithic analysis.
Sampling strategy	The OSL samples were taken to bracket the cultural layers. The lithic assemblage was studied as a whole.
Data collection	OSL and lithic data were collect and analysed by H.Y. and co-authors
Timing and spatial scale	The data collection stars from 2015 until 2018. This is part of the PhD project of H.Y.
Data exclusions	All data are analysed and contributed to final conclusion.
Reproducibility	OSL dating procedure was validated using a series of laboratory-controlled experiments, such as dose recovery, preheat plateau and various well-established rejection criteria.
Randomization	N.A.
Blinding	N.A.

Did the study involve field work? ☒ Yes ☐ No

Field work, collection and transport

Field conditions	Two field trips were conducted in the Guizhou province, China, one in summer 2015 and the other in winter 2018.
Location	Guanyindong Cave (26°51′26″N, 105°58′7″E, 1464 m a.s.l.)
Access and import/export	We were working under the permission of the Bureau of Cultural Relics Protection, Qianxi County, Bijie, Guizhou Province, China
Disturbance	This site has been excavated for ~40 years, so only residual profiles were available, and we did not conduct further excavation but just took OSL samples for dating. The opened profile was sealed for further protection after sampling.

Reporting for specific materials, systems and methods

Materials & experimental systems

n/a	Involved in the study
☒	☐ Unique biological materials
☒	☐ Antibodies
☒	☐ Eukaryotic cell lines
☒	☐ Palaeontology
☒	☐ Animals and other organisms
☒	☐ Human research participants

Methods

n/a	Involved in the study
☒	☐ ChIP-seq
☒	☐ Flow cytometry
☒	☐ MRI-based neuroimaging

nature
SUPPLEMENTARY INFORMATION
https://doi.org/10.1038/s41586-018-0710-1
In the format provided by the authors and unedited.

Late Middle Pleistocene Levallois stone-tool technology in southwest China

Yue Hu[1], Ben Marwick[1,2]*, Jia-Fu Zhang[3], Xue Rui[1], Ya-Mei Hou[4,5], Jian-Ping Yue[4,5], Wen-Rong Chen[6], Wei-Wen Huang[4] & Bo Li[1,7]*

[1]Centre for Archaeological Science, School of Earth and Environmental Sciences, University of Wollongong, Wollongong, New South Wales, Australia. [2]Department of Anthropology, University of Washington, Seattle, WA, USA. [3]MOE Laboratory for Earth Surface Processes, Department of Geography, College of Urban and Environmental Sciences, Peking University, Beijing, China. [4]Key Laboratory of Vertebrate Evolution and Human Origins, Institute of Vertebrate Paleontology and Paleoanthropology, Chinese Academy of Sciences, Beijing, China. [5]CAS Centre for Excellence in Life and Paleo-environment, Beijing, China. [6]Qianxi County Bureau of Cultural Relics Protection, Bijie, China. [7]ARC Centre of Excellence for Australian Biodiversity and Heritage, University of Wollongong, Wollongong, New South Wales, Australia. *e-mail: bmarwick@uw.edu; bli@uow.edu.au

SUPPLEMENTARY INFORMATION

SI section 1

Supplementary Discussion | Geological and archaeological background

Introduction to Guanyindong Cave

Guanyindong Cave (26°51′26″N, 105°58′7″E, 1464 m a.s.l.) is located in the Qianxi county of Guizhou province, the eastern end of the Yungui Plateau, Southwest China (Fig. 2). This region has a typical karst landscape (Extended Data Fig. 1) with a general elevation of 1400–2000 m, and is composed of carboniferous and Permian limestones, cataclastic rocks, basalt, and coal deposits. The main ecosystem types include evergreen broad-leaved forest, coniferous and broad-leaved mixed forest, and montane elfin forest. With a subtropical humid climate (humid in summer and dry in spring), this region is controlled by the East Asian summer monsoon and the cold fronts of the winter monsoon and the southwest warm-wet air masses [1]. The mean annual temperature is about 14 °C, with the highest monthly mean temperature (20–21 °C) in summer and the lowest (4–5 °C) in winter. Mean annual precipitation in this region is ~1400 mm.

Guanyindong Cave is a limestone cave developed during the Late Tertiary or beginning of the Quaternary [2], and is one of the highest and most developed karst caves in this region. The cave, extending from east to west, was developed from a fracture that was mainly formed by an east-west strike, joint with several south-north branches (Extended Data Fig. 2a). The main entrance, which is also the main excavation area, is located at the west end of the cave. The cave, about 90 m long and 2–4 m wide, has a narrow roof that gradually broadens down to the floor. The distance from floor to roof is about 2–8 m high. The cave floor is about 15 m above the bottom of the depression.

The sedimentary deposits slope down from the entrance to the inside of the cave (Extended Data Fig. 2b), and there is a general trend of decreasing grain size of sediments from outside to inside [2], indicating that the source of the deposit came mainly from the outside. Stalactites and stalagmites are well developed inside the cave, and some of them are connected, forming stalagnates. Thick flowstone plates were developed surrounding the stalagnates at various areas in the cave, these plates cover the majority of sediment in the cave, but the thickness of the plates varies.

The Guanyindong Cave site was first discovered in 1964 by a field team organised by the Institute of Vertebrate Paleontology and Paleoanthropology and the Provincial Museum of Guizhou. Four excavation seasons were conducted in 1964, 1965, 1972 and 1973, respectively. Several trenches (Profiles 1, 2a, 2b and 3) were opened within the cave (Extended Data Fig. 2a) in the 1960s, which yielded about a hundred stone artefacts. The main excavation was conducted in the 1970s at the west cave entrance (Extended Data Fig. 2a), where most of the fauna fossils and stone artefacts were found [2].

Stratigraphy and fossil assemblage

The deposits at the site are mainly sandy/silty clays with limestone and breccia fragment inclusions. According to the excavation report by the original excavators [2,3], the stratigraphy of the sediments at the main entrance was divided into 9 layers (Layers 1–9) (Extended Data Fig. 2a) and 3 groups: Group A (Layer 2), Group B (including Layers 3–8) and Group C (Layer 9) [2]. While Layer 1 and Group B extend from the outside to the inside of the cave, Layer 2 (Group A) was found in front of the cave entrance only (Extended Data Fig. 2b). Most sediments from Layer 1, Groups A and B in the main excavation area had been removed during the previous excavations. In 2015, we visited the cave and found a ~3m residual profile, named S1, which is located at the south-wall near the cave entrance (Extended Data Figs 2b and 3a).The Layer 1, Groups B and

C were still visible at S1 (Extended Data Figs. 3b, c). In 2018, we re-visited the site and found another residual profile, S2, at the south wall, about 14 m away from the cave entrance (Extended Data Figs 2b and 4), where the Layer 1 and Layer 2 are exposed. The stratigraphic features of the two profiles are consistent with those described by the excavators [3]. The features of each layer are described in Supplementary Table 1.

The fossils from Group A are mostly fragments [2], indicating that the material of Group A was probably reworked before deposition. Only a few species were identified, including *Rhinoceros sinensis Owen*, *Stegodon sp.*, *Hystrix sp.* and *Bovinae*. In contrast to Group A, the fossils from Group B were much better preserved, and abundant species can be identified, including 23 families [*Eulota (Cathaica) sp.*, Testudinidae indet., *Macaca sp.*, *Hystrix cf. subcristata Swinhoe*, *Rhizomys cf. sinensis Gray*, *Vulpes cf. vulgaris* L., *Ursus thibetanus kokeni* M. et G., *Ailuropoda melanoleuca fovealis* M. et G., *Mustelidae indet.*, *Crocuta ultima Matsumoto*, *Panthera cf. tigris* L., *Gomphotheriidae indet.*, *Stegodon cf. orientalis* Owen, *Stegodon guizhouensis* Li et Wen sp. nov., *Equus sp., Megatapirus augustus* M. et *G.*, *Rhinoceros sinensis* Owen, *Sus cf. scrofa L.*, *Muntiacus sp.*, *Cervus (cf. Pseudaxis) sp.*, *Rusa sp.,* Bovinae, and *Capricornis sumatraensis* Bechstein] and 13 species (*Gastropoda*, *Chelonia*, *Primates*, *Rodentia*, *Carnivora*, *Proboscidea*, *Perissodactyla* and *Artiodactyla*). Most of these species belong to the Middle Pleistocene *Ailuropoda-Stegodon* fauna group, which is commonly found at cave sites in South China.

<u>Previous chronological studies</u>

There were a few attempts to date the Guanyindong site since the 1980s. The first dating work was conducted by Yuan et al. [4] using U-series dating on fossil teeth recovered directly from the stratigraphic units of the site. In their study, a total of 6 fossil teeth were dated, including one from Layer 2 (Group A), one from Layer 4, three from Layer 5 and one from Layer 8 (Supplementary Table 1). Given the complexity and difficulty of quantifying uranium migration into and out of skeletal tissues, the U-series results on bones and teeth should be regarded as minimum age estimates [5]. The U-series age of the fossil tooth from Layer 2 is 55 ± 3 ka, hence, providing a minimum estimate for the age of Group A. The other U-series ages obtained for the fossil teeth from Group B range from ~75 to ~120 ka, placing a minimum age of ~120 ka for the Layer 4 and those below.

The second atempt was conducted by Shen and Jin [6], based on U-series dating on carbonate and fossil teeth. In their study, samples were taken from three locations (named Profiles 1, 2a and 3 by Pei et al. [3]) inside the cave (Extended Data Fig. 2c). Profile 1 is located at the cave entrance. Profiles 2a and 3 are two of the earliest test pits excavated by Pei et al. [3] in the 1960s. They are located further inside the cave, where very few artefacts (~100 stone artefacts) were found and many of them were collected from the surface. Since the artefacts excavated inside the cave are not analysed in our study, we focus our discussion on Shen and Jin's dating results for the samples from the cave entrance only. A total of 8 samples were collected from the cave entrance (see Extended Data Fig. 2a for their plane locations). The first two samples (QGC-19-1 and QGC-19-2) were taken from the bottom tip of a hanging stalactite, yielding ages of 58 ± 3 and 42 ± 2 ka, respectively. The authors claimed that this stalactite "has sign of residual red clay on the bottom surface", indicating that this stalactite was in contact with the red-clay deposits from Layer 2 and, hence, should provide a maximum age estimate for Layer 2. However, this age is younger than the U-series age (~55 ka) of the fossil tooth extracted in-situ from Layer 2 reported by Yuan et al. [4]; the latter should be viewed as a minimum age of Layer 2. Furthermore, according to the stratigraphic description by Li and Wen [2] (see Extended Data Fig. 2b), the deposits of Layer 2 terminated outside the cave, so the 'red-clay attachement' on the stalactite should not be linked to the Layer 2, and, therefore, its age should not be used to constrain the age of Layer 2. Our OSL age of ~80 ka for Layer 2 also confirms that their age estimates for Layer 2 are underestimated.

The third sample (QGC-4) is a piece of broken stalactite sitting on top of "some residual deposits" at the north wall, which yielded an age of > 350 ka, and it should not be linked to any stratigraphic unit of the site. The fourth sample (QGC-12) is "a piece of flowstone sitting on top of some residual deposits attached to the north wall of the cave". This sample yielded an age of 52 ± 2 ka. According to Shen and Jin, this sample has the same elevation as Layer 4, and they regarded this age as an estimate of the age of Layer 4. However, this age is significant younger than the minimum age (~119 ka) obtained from the fossil teeth directly taken from Layer 4 reported by Yuan et al. [4], suggesting that the correlation of the sample and Layer 4 simply based on their elevation is unreliable.

The fifth sample (QGC-21) is a piece of carbonate 'curtain' taken on the north wall but a few tens of centimeters below QGC-12. This sample yielded an age of 147 ± 14 ka. Given the failed correlation of the overlying sample QGC-12 mentioned above, the stratigraphic location of QGC-21 remains unclear. The sixth sample (QGB-4) is a rhinoceros tooth recovered from Layer 6 in the residual sediment profile at the south wall (where our OSL samples were taken). The U-series age of this sample is 73 ± 3 ka, and should be viewed as a minimum age for this layer. The seventh sample (QGC-7) is 'a small piece of stalagmite sitting on top of the flowstone from Layer 6' of the residual profile at the south wall. The age of this sample is 185 ± 15 ka, providing a reliable constraint of the age for this layer. The last sample (QGC-23) is an in-situ stalagmite from the bottom of the profile at the north wall, which yielded an age of 260 ± 30 ka. This age should provide a reliable constraint of the maximum age for Layer 8 or Group B.

In conclusion, previous U-series dating on fossil teeth and carbonate have provided controversial results, mainly because many of the analysed carbonate samples lack firm stratigraphic control. As a result, only those samples with a reliable stratigraphic control can provide useful constraints on the chronological framework of this site (Supplementary Table 1). For this reason, all of the U-series ages of fossil teeth extracted directly from sediments should be viewed as minimum ages for the associated layers, and only one stalagmite sample (QGC-7) taken directly from Layer 6 from the residual profile at the south wall yielded reliable age estimate for this layer (~180 ka).

SI section 2

Supplementary Discussion │ Guanyindong Cave lithic analysis

Previous analyses of Guanyindong Cave lithics

The classification of Levallois products remains a subjective matter, on which analysts often disagree [7-9]. As one of the most important Palaeolithic sites in Southern China, Guanyindong is no exception to this, with previous studies coming to differing conclusions about the presence of Levallois in the Guanyindong Cave assemblage.

One of the earliest English-language sources [10] describes casts of five artefacts and identifies one as a transverse concave scraper made on a pseudo-Levallois point. Anticipating additional Levallois products, Freeman concludes that he 'would venture to guess that the collection will prove to have some proto-Levallois or true Levallois flakes when it is finally studied' (p. 101). Li et al. [11] came to a different conclusion after detailed examination of 1108 stone artefacts housed in the IVPP collections. They employ the chaîne opératoire concept to conduct a 'technological reading' of the assemblage. They identified three categories of cores representing three technological systems. Neither of these 'involve intentional preparation' (p. 3869) so they conclude that the Guanyindong Cave artefacts are 'quite distinct from the concept of Levallois' and reflect 'different modes of cognition' (p. 3870). A third report mentioning Guanyindong stone artefacts summarises the assemblage and notes that 'a few Levallois-like flakes were identified' [12].

Of the three previous English-language reports on the Guanyindong Cave stone artefacts, two claim to have observed traces of Levallois in the assemblage, and one argues that it is absent. We interpret the artefacts differently than past researchers and we have made 3D models for anyone else to examine and interpret (see Supplementary Data). In our view, the analysis of Li et al., which concluded that Levallois concepts are absent from Guanyindong, is problematic because of their relying on chaîne opératoire-related methods that contribute to the irreproducibility of their results. The clarity and objectivity of chaîne opératoire methods have been widely questioned by stone artefact analysts. For example, Bar-Yosef and Van Peer argued that chaîne opératoire is '*overformalized and provides but an illusion of reading the minds of prehistoric knapper*'[13]. Similarly, Monnier and Missel [14] have noted that use of chaîne opératoire concept is '*highly subjective; being based upon the analyst's experience and intuition*" (p. 3). A well-known example of this problem can be found in the analysis of the assemblage from Biache Saint-Vaast level IIA. Boëda [15] identified unidirectional and bidirectional recurrent Levallois core reduction, but Dibble [16] found that the core reduction strategy changed from unidirectional to bidirectional as cores were more extensively reduced. This example highlights the difficulty of using the chaîne opératoire concept to obtain a result that can be reproduced by another analyst.

In their chaîne opératoire analysis, Li et al. describe three cores from Guanyindong Cave in detail (P4114, P4122, P15948). We concur with their assessment of P4114 and P4122 that these cores are not Levallois. Contrary to Li et al, however, we identify P15948 as Levallois (see Fig. 3a, Extended Data Fig. 5a and the 3D structure in Supplementary Data), and we will discuss this piece in detail as an example of how our approach differs from Li et al. We disagree with Li et al. on details of the analysis of this piece: Li et al. claimed that 1) each flaking sequence is unrelated; 2) there is only one flaking sequence; 3) all the flake scars come from the same direction, 4) convexity is obtained by the flake ventral surface; and 5) the platform is not prepared. They, however, offer no explanation for one critical assumption, why they found each flaking sequence to be unrelated. On the contrary, we found each sequence to be hierarchically related. First, through faceting along the edge, the striking platform size and shape was adjusted to allow removal of flakes parallel to the plane of intersection of the upper and lower surfaces. Then, convexities were shaped and maintained with removals based on the previously prepared striking platform. Finally, the Levallois products were split off by using a centripetal recurrent method along the fracture plane that is parallel or sub-parallel to the plane of the intersection. We consider each of these flaking sequences to be related because one sequence could not start before the other was completed. In our view there are three flaking sequences, not one, as claimed by Li et al.. In addition, rather than originating from the same direction, these scars run from multiple directions by using the Levallois recurrent centripetal method. There are two flake scars for which they did not explain the sequence ascription

Their fourth claim, that the blank of the core is a flake, is not convincing because this core is a slab or nodule with part of the cortex left on the lower surface. The most distant ends of the piece have a similar thickness of about 20–30mm. It is not like a typical Guanyindong flake which is thick at the proximal end and thin at the distal end. There are many cores that are made from flakes in Guanyindong and we describe these with the term “truncated faceting”. From these cores, we can see that the scars are either too small or too scarce to be classified as Levallois, and most of them are on the edge without extending across the whole ventral surface. Even if the ventral surface was flaked, we cannot say that it was not prepared. For example, at Orgnac 3 in France, slabs are a common component of the Levallois assemblage, and half of Levallois cores take advantage of the natural convexity of a flake’s ventral surface to maintain the distal and literal convexities[17,18].

Finally, we observed signs of preparation on the platform of this piece, which is not a cortical surface as reported by Li et al.. Our analysis found Levallois attributes on P15948, which presents all stages of reduction and manufacture of a Levallois core. The upper surface is covered with several scars come from different directions forming a centripetal scar pattern. Before flaking on the debitage surface, the core had been knapped along the edge to prepare the striking platform. The fractures of the predetermined flakes are parallel to the plane of the flake release surface and the striking platform surface.

Our detailed description of P15948, above, is typical of how our analysis of the Guanyindong assemblage differs from Li’s. In Li's Ph.D. thesis [19] she describes 18 cores. Besides P15948, there are two more artefacts that we identified as Levallois cores (P5262 and P16311), but Li did not. For P5262, Li’s conclusion is based on the assumption that the core was knapped from a naturally convex surface. But we did not find a natural convex surface, and instead observed preparation scars on its lateral and distal convexity, creating this geometry. Furthermore we found a prepared platform, contrary to Li’s observation of a cortical platform. For P16311, which has the least clear scar pattern of the three pieces noted here, Li identified a joint face, but in our view there are scars resulting from upper and lower surface structures typical of Levallois pieces. The key issue for each of their pieces remains the same: we did not make assumptions about the blank’s geometry, but observed it directly. We report a summary of our analysis in the following sections.

Whole assemblage characteristics: cores, flakes & retouch

We analysed 2273 artifacts in the whole assemblage which consists of 267 cores, 1195 flake pieces, 42 retouched pebbles & chunks and 769 chunks & debris (see examples shown in Extended Data Figs 5 and 6 and Supplementary Figs 21–24). The R code used to produce the results presented here is available online at http://doi.org/10.17605/OSF.IO/ERNTJ.

Chert is the dominant raw material for the assemblage (~80%). The 1195 flake pieces include a large number of retouched flakes and retouched flake breaks (n=1008), complete flakes (n=182) and a small quantity of flake fragments (n=5). While all stages of reduction and manufacture are represented, final stages are most abundant. The average maximum length of the flakes pieces is 55.5 mm, the average thickness is 16.3 mm.

Plain platform is the major type of flake platforms. The average number of scars on the dorsal side of complete flakes is three. Flakes with three dorsal scars are the largest proportion and more than 80% of flakes have four scars or less. Most of the cortex is limited, ranging from 0 to 10%. It suggests that before hominins brought knapping products into the cave they had knapped the blank outside of the cave, and, therefore, the flakes were on the later stages of knapping, with less cortex.

In total, we found 267 cores in the lithic assemblage. The average max dimension is 74.8 mm and with an average mass of 165 g. This dimension is slightly larger than the flakes. The flaking technique of Guanyindong Cave is free-hand percussion with hard hammer. The raw material of cores is dominated by chert (85%) followed by limestone (14%). There are various geometries of cores, including irregular (80%), conic (9.6%), column (6.8%) and small amounts of wedged and circle. Most cores (~80%) produced 1–4 flake scars before being discarded. Cores that have more than eight scars are rare (n = 4). The average scar length is 33 mm. Most cores are covered with zero (46.5%) or 5–20% cortex (31.5%). The majority of platform type is plain (52%), which suggests that using former scars as platform to continue flaking is the main strategy of knapping.

Five discoid cores were identified in the assemblage (see examples from Supplementary Figs 21.3, 21.4, 22.3 and 22.4). Morphologically, some of these discoid cores resemble several features with Levallois cores, but they are rejected based on the criteria of Levallois technology, mostly because either the direction of flaking is secant to the line of the plane of the upper and lower surfaces or the two surface are exchangeable. In the Guanyindong Cave assemblage, toolmakers usually selected a flat surface from the blank and then knapped around the edge forming geometries varying from conic to irregular. The average maximum dimension of discoid cores is ~64 mm. The average number of flakes obtained from a discoid core is four. Three of them have a surface covered with cortex and the platforms are mainly plain.

A total of 1050 retouched pieces were found in the assemblage (see examples from Supplementary Fig. 24), accounting for 46% of entire lithic assemblage. The average max dimension of retouched pieces is about 56 mm. Side scrapers and denticulates dominate the sub-division of retouched pieces (74%), followed by notches (9%) and borers (7%). Over 50 % (n=525) of the retouched pieces have more than one retouched edge. The shapes of 1683 retouched edges include convex, concave, straight, denticulate, end, notch, and borer. Among them, straight edge constitutes the largest proportion of the retouched edge (n=523) followed by convex (n=348) and concave (n=250).

Assemblage characteristics: prepared elements, cores and flakes

In addition to the Levallois assemblage, cores and flakes with prepared platforms, blade cores and truncated-faceted pieces are also found in the assemblage. Eighteen cores are found with prepared platforms. This type of core features facetted scars on the striking platform in order to preparing a proper angle before knapping. Shapes of these cores are mainly irregular (67%) and conic (22%). Most of them (~56%) have only one platform. The average max dimension is 79.6 mm.

There are 43 flakes with faceted platforms, 72% of which were retouched to make tools. The majority of platform shapes are quadrangle (364%) and triangle (20.5%). The average platform width and thickness is 35.2 × 11.4 mm. The average max dimension of these flakes is 62.3 mm. Only a few flakes show traces of dorsal cortex (20%) and most of them have one or more previous flake scars remaining on the dorsal surface. A small amount of blade cores were also found (see examples from Supplementary Figs 21–23). Compared with blade cores from the European Upper Palaeolithic [20], these blade cores present distinctive features. The geometries of these cores vary from flat circle to cylinder, and are not as regular as those found in typical Upper Palaeolithic assemblages, where blade cores usually present prismatic shapes. Some of their platforms are facetted and only a few blades were obtained from each core.

Core preparation is also present on 60 truncated-faceted pieces [21-24]. These pieces usually started from a flake that was then knapped on the ventral side, ending up as cores with the flake scars on ventral side, indicating the production of invasive flakes from platforms along the dorsal edge (Supplementary Figs 21–23). Other than on cores themselves, attributes indicating core preparation are also found on flakes (see examples from Figs 3t–3z and Extended Data Figs 6–7). Furthermore, evidence for maintaining core convexities is observed from 26 débordants (Fig. 3l and Extended Data Fig. 6), blanks that remove a large part of a core's lateral edge and are typically considered to be byproducts of core maintenance [25].

Patterns in artefact reduction

To understand the technological sequences that produced the artefacts at Guanyindong Cave we investigated how flake attributes vary across different sized pieces. The distribution of flake mass is strongly right-skewed with a long tail, typical of many flaked stone artefact assemblages (Extended Data Fig. 8). The unimodal quality of this distribution does not indicate any obvious size classes suitable to use as analytical categories to compare flake attributes in different reduction stages. To divide the flakes in the assemblage into analytical categories we used a dynamic programming algorithm for optimal one-dimensional k-means clustering[26]. This method selects optimal number of clusters of flake sizes based on the Gaussian mixture model using the Bayesian information criterion (BIC). After limiting cluster membership to 30 or more artefacts, we found five clusters of size classes in the Guanyindong Cave flakes that we can use to investigate changes in flaking behaviours relative to size.

Raw materials are uniformly distributed across each size class (Extended Data Fig. 9). Cortex location shifts markedly from the left, right and distal areas of the dorsal surface for larger flakes (size class 5), to be found mostly on the platform and right side of the dorsal surface of smaller flakes (size classes 1, 2 and 3). This indicates that most small flakes result from advanced stages of the reduction process. The high proportion of flakes with cortex on the right indicates a repeated sequence of flake removals moving left to right across the face of a core. Platform shape shows a trend of an increasing proportion of rhombus platforms as flake size decreases. The “gull-wing” [27] platform (also called "platform beveling" [28]) is increasingly represented in the smaller size classes. This shape of platform resulted from the detachment of a flake directly behind the location of a previously detached flake, and has been frequently found in Levallois points [29], as well as Nubian Complex [30] and tula adze blanks [27]. This pattern in the Guanyindong assemblage indicates a high degree of precision when producing the smaller flakes.

Platform types are highly diverse throughout the reduction sequence. Missing platforms are more common on the smallest flakes. Faceting is only evident on mid- and small-sized flakes (size classes 1, 2, and 3), consistent with a Levallois strategy of preparing cores by flaking across their platforms, resulting in flakes with facetted platforms. The low proportions of faceting on large flakes indicate that this was not a generic technique applied at all reduction stages, but only preferentially applied to certain-sized flakes produced via Levallois processes. We can see further support for this in the distribution of flake types, with Levallois flakes also appearing only in the mid- and small-sized flakes. This indicates a well-controlled reduction strategy where the production of Levallois flakes was constrained to a specific size range. Kombewa flakes are most abundant in the largest size class. This type of flake is distinctive due to having two opposed bulbs of percussion because it is detached at the intersection of the platform and ventral surface of a larger flake. The rarity of Kombewa flake in the smaller sized flakes reflects the high levels of inertia and precision required to detach a flake from a larger flake

The distribution of retouch types shows complex variation across the reduction sequence. Only subtle changes in proportions are evident across the size classes. The three smaller size classes have the greatest diversity and most even distribution of retouch types. This indicates how retouch types present in the larger size class, such as scrapers, notched pieces, borers and denticulate pieces, are transformed into new types, such as tanged pieces, points, and end-scrapers, as reduction of a piece proceeds further and the mass of the pieced is reduced by reduction.

Extended Data Fig. 8 shows that as for larger flakes sizes, the oriented thickness and flake thickness (at 25%, 50% and 75% of the length axis) all increase only very slightly, relative to increases in mass, length, oriented width, platform width and platform thickness, which increase substantially. For the most part, flake thickness is thus less than expected for larger flakes. This indicates that the thickness of larger flakes was controlled by the knappers at the start of the reduction sequence, consistent with a deliberate strategy to produce flakes with desirable features in tools, such as capacity for retouch and reduction of torque. The percentage of dorsal cortex varies little, from a median of 10% to 0%, but with a higher range in the larger flakes. This indicates even the largest flakes often do not have much cortex on their dorsal surface, so some pre-processing of the artefacts must have happened before they arrived at Guanyindong Cave. The median and range in the number of flake scars is nearly constant across size classes.

Artefact taphonomy

Among the flake pieces in the assemblage, 63% (n = 748) are broken, among which most of them are retouched. Two processes are likely responsible for this high percentage: manufacturing failures during the knapping activity, and energetic taphonomic processes that have damages the artefacts after discard. The generally homogenous nature of the stone indicates that failures during knapping should be expected at a low frequency, assuming a competent knapper. The sedimentary feature of the deposits (characterised by well stratified and sorted silt and sand layers) inside the cave indicates a low-energy depositional process. Thus, many of the breakages may be attributed to post-depositional processes such as ground surface breakage due to trampling. We found two artefacts that can be refitted (Supplementary Fig. 22.12). Many of the artifacts show considerable edge rounding/chipping, indicating some form of taphonomic influence. For example, trampling and post-depositional processes may have damaged artefact edges in ways that resemble light retouch, which may partly explain the high percentage (46%) of retouched pieces in the whole assemblage. With just two artefacts showing signs of heat treatment, we conclude that artefact damage due to excess heating occurred at a negligible rate at Guanyindong Cave. The surface texture of the artefacts is generally fresh, indicating limited weathering from exposure to pedogenic processes. This is probably a result of the cool, dry environment within the rockshelter.

Chronological change in the lithic assemblage

The artefacts that we analyzed were collected during excavations in 1964–1973, when it was not typical to record artefact provenance at high spatial resolutions. Thus, only a small amount of the stone artefact assemblage contains provenance information that allows us to determine what period of time is represented. A total of 204 pieces of the studied stone artefacts have clear stratigraphic information, with 117 pieces from the lower layer (Group B, 170–160 ka) and 87 from the upper layer (Group A, ~90–80 ka). Only five Levallois pieces included information about which layer they were recovered from (3 from the upper layer, 2 from the lower layers). This small number of artefacts with chronological context limits the robustness of any claims we can make about change over time at Guanyindong Cave. Nevertheless, the patterns that are evident provide support to our main claim for Levallois technology appearing here at 170–80 ka.

Extended Data Fig. 10 shows that flakes are slightly larger in the upper layer, and more variable in the thickness dimensions. Limestone is more frequently utilized as a raw material in the upper layer, as well as a small amount of sandstone, which does not appear in the lower level assemblage. This minor increase in raw material breadth in the upper layer may relate to a decrease in the availability of chert on the landscape, perhaps due to increased vegetation cover during MIS 5 that may result in changes in forager mobility strategies. Most of the technological attributes show little difference between the upper and lower layers, indicating that the technological strategies were similar across the two periods. Notable differences include platform shape, where we see higher proportions of rhombus and gull-wing platforms in the lower layer. We also see a much higher proportion of facetted platforms in the lower layer. The high frequency of platform faceting in the lower layer is notable because faceting is a key step in the preparation of striking platforms on Levallois cores. While this attribute by itself is not sufficient to identify a piece as Levallois, the high frequency of it in the lower layer is consistent with this period (170–80 ka) as a time when the cave's occupants were producing Levallois technology.

SI section 3

Supplementary Table 1 | Description of stratigraphic layers, number of stone artefacts, together with ages (±1σ error) obtained from samples that have reliable stratigraphic age control and associated dating methods. Note that the U-series ages of fossils should be regarded as minimum age estimates.

Layer	Thickness (cm)	Sedimentary features	Number of stone artefacts	Age (ka) / Method / Reference
1	~15–70	Archaeologically sterile and consists of black silty clay	0	• 40–70 (OSL on 3 sediment samples) (this study)
Group A				
2	~40–240	Reddish-yellow silty clay, containing abundant rock debris and plenty of stone artefacts and fragments of mammal fossils. This layer sits unconformably on top of Group B (Extended Data Fig. 2b).	879	• 57 ± 3 (U-series on a rhinoceros tooth) [4] • 87 ± 3 (weighted mean of 4 OSL samples) (this study)
Group B				
3	~50–100	A loose layer with brown-yellow and grey-yellow silty clay, containing fragments of limestone and breccias. According to the excavation report, this layer yielded only a small number of stone artefacts and fossils.	20	
4	~40–50	Brown-yellow and red-yellow silty clay with some fragments of limestone breccias. The top of this layer is capped by a flowstone layer (3–5 cm in thickness). Many stone artefacts and fossils were found from this layer.	68	• 119 ± 10 (U-series on a unknown fossil tooth) [4] • 163 ± 12 (weighted mean of 2 OSL samples) (this study)
5	~20	Grey silty clay with abundant limestone fragments, which yielded plenty of stone artefacts and fossils.	801	• 84 ± 5 (U-series on a *Bovinae* tooth) [4] • 76 ± 4 (U-series on a unknown fossil tooth) [4] • 104 ± 6 (U-series on a rhinoceros tooth) [4] • 163 ± 12 (OSL on sediment) (this study)
6	~10	Similar to Layer 4 but with the absence of large limestone fragments. This layer yielded more stone artefacts and fossils than Layer 4.	236	• 73 ± 3 (U-series on a rhinoceros tooth) [6] • 181 ± 16 (U-series on stalagmite) [6] • 175 ± 32 (OSL on sediment) (this study)
7	~15	A grey-yellow silty clay layer containing stone artefacts and fossils with abundant small limestone fragments.	139	• 167 ± 12 (OSL on sediment) (this study)
8	~10	Yellow silty clay, containing limestone and breccias fragments. Stone artefacts and fossils were found from this layer too.	20	• 115 ± 7 (U-series on a *Cervidae* tooth) [4] • 169 ± 14 (OSL on sediment) (this study)
Group C				
9	> 10 cm	Archaeologically sterile and consists of layers of sand, gravels and breccias.	0	• 260 ± 30 (U-series on stalagmite) [6]

Supplementary Table 2 | Summary of the sites shown in Fig. 1, together with their corresponding ages and dating methods used. For some sites, precise numerical ages are not available because absolute dating methods were not applied and their ages were only roughly estimated by stratigraphic correlation, so only MIS stages were provided for these sites. All uncertainties are expressed at 1σ.

ID	Site	Country	Age (ka)	MIS stage	Dating method	Reference
1	Guanyindong	China		6–4	OSL/U-series	This study
	AFRICA					
2	Bundu farm	South Africa	190–340	9	ESR	[31]
3	Kathu Pan	South Africa	291 ± 45	9	OSL/ESR/U-seires	[32]
4	Kibish formation	Ethiopia	~195	7	Ar/Ar	[33,34]
5	ETH72-8B & Kulkuletti (Gademotta formation)	Ethiopia	~280	8	Ar/Ar	[33]
6	Florisbed	South Africa	268 ± 26	8	ESR, OSL	[35]
7	Sterkfontein cave	South Africa	252 ± 42	8	ESR/stratigraphy	[31]
8	Gademotta	Ethiopia	180–280	8	Ar/Ar	[31,36]
9	Kulkuletti	Ethiopia	~280 ± 8	8	Ar/Ar	[31,36]
10	Border cave	South Africa	217–238	7	ESR	[31]
11	Kapthurin formation	Kenya	200–250	7	Tephra	[33,37]
12	Kharga oasis & site REF-4	Egypt	220 ± 20	7	U-series	[38]
13	Sai island	Sudan	152–223	7	OSL	[39]
	EUROPE					
14	Achenheim	France	258 ± 23	9	stratigraphy	[40]
15	Ambrona	Spain	336 ± 36	9	ESR / U-series	[41]
16	Aridos 1	Spain		9	stratigraphy	[42]
17	Atapuerca	Spain	345 ± 26	9	ESR / U-series	[43]
18	Dall'Olio Cave	Italy		9	stratigraphy	[44]
19	Domeny	Spain	> 317 ± 49	9	Ar/Ar, stratigraphy	[45]
20	Gentelles base	France		9	stratigraphy	[44]
21	La Micoque	France	288–350	9	ESR/U-series	[46]
22	Cagny Lépinette	France		9	stratigraphy	[47]
23	Orgnac 3	France	> 303	9	Ar/Ar, U-Th	[48]
24	Petit bost	France	325 ± 30	9	TL	[49]
25	Puig den Roca	Spain	< 317 ± 49	9	Ar/Ar, stratigraphy	[45]
26	Purfleet	UK	~ 324	9	TL, stratigraphy	[50]
27	Solent River	UK		9	stratigraphy	[51]
28	Torralba	Spain	> 243 ± 18	9	U-series, stratigraphy	[52]
29	Torre in Pietra	Italy		9	stratigraphy	[53]
30	Argoeuves	France		8	stratigraphy	[54]
31	Baume Bonne	France		8	stratigraphy	[55]
32	Kesselt -Op de Schanz	Belgium		8	stratigraphy	[48]
33	Les Bossés	France	274 ± 12	8	TL	[56]
34	Markkleeberg	Germany		8	stratigraphy	[57]
35	Mesvin	Belgium	283 ± 30	8	U-Th	[58]
36	Raspide 2	France		8	stratigraphy	[59]
37	Rheindahlen	Germany		8	stratigraphy	[60]
38	Abri Vaufrey	France	208 ± 8	7	U-series	[61]
39	Bapaume les (Pas-De-Calais)	France	~195	7	IRSL	[62]
40	Bečov I	Czech Republic		7	stratigraphy	[63]
41	Biache-Saint-Vaast	France	230 ± 18	7	ESR/U-series/TL	[64]
42	Biśnik Cave	Poland	230 ± 51	7	TL	[65]
43	Bonneval	France	240	7	TT-OSL	[66]
44	Campsas	France		7	stratigraphy	[67]
45	Cantalouette	Ukraine	223 ± 20	7	TL/stratigraphy	[68]

ID	Site	Country	Age (ka)	MIS stage	Dating method	Reference
46	Dzierżysław	Poland		7	stratigraphy	[69]
47	Galeria Pesada	Portugal	241 ± 22	7	ESR/U-series	[70]
48	Gran Rois	France		7	stratigraphy	[62]
49	Hundisburg	Germany		7	stratigraphy	[71]
50	Korolevo	Ukraine	220 ± 35	7	OSL	[72]
51	La Cotte de St.Brelade	UK	238 ± 35	7	TL	[73]
52	Le Pucheuil	France		7	stratigraphy	[74]
53	Le Rissori(MSJ)	Belgium		7	stratigraphy	[75]
54	Maastricht Belvédère	Netherlands	258 ± 19	7	TL/ESR	[76]
55	Nové Mesto nad Váhom	Slovakia		7	stratigraphy	[69]
56	Raciborz Studienna 2	Poland		7	stratigraphy	[69]
57	Salouël	France	> 200 ± 57	7	ESR/U-series	[77]
58	San Bernardino	Italy	184 ± 6	7	ESR	[78]
59	Thames valley	UK		7	stratigraphy	[79]
60	Therdonne	France	178 ± 11	7	TL/stratigraphy	[80]
61	Weimar-Ehringsdorf	Germany	230	7	U-Th	[81]
62	Susiluola Cave	Finland	> 100	5	OSL, TL, stratigraphy	[82]
	ASIA					
63	Attirampakkam	India	385 ± 64	9	OSL	[83]
64	Nor Geghi	Armenia	335–325	9	Ar/Ar, stratigraphy	[71]
65	Denisova Cave	Russia	220–280	8	TL	[84]
66	Hayonim	Israel	~ 220	7	TL/ESR	[85]
67	Misliya Cave	Israel	177–194	6	ESR/U-series	[86]
68	Hummal	Syria	150–220	7	TL	[87]
69	Jebel Qattar JQ-1	Saudi Arabia	211 ± 16	7	OSL	[88]
70	Karain cave	Turkey	250–200	7	TL/ESR	[89]
71	Misliya cave	Israel	166–212	7	TL	[90]
72	Tabun(Mount Carmel)	Israel	256 ± 26	7	TL/ESR	[91]
73	Mikhailovskoe	Russia		9–7	stratigraphy	[92]
74	Obi-Rakhmat Grotto	Uzbekistan	55–73	6	ESR, OSL	[93]
75	Ust-Karakol 1	Russia	133 ± 33	6–5	TL	[94,95]
76	Aybut al Auwal	Oman	106	5	OSL	[96]
77	Bogdanovka	Russia		5	stratigraphy	[97]
78	Garchi I	Russia	~115	5	OSL	[98,99]
79	Jwalapuram (JPW 3a)	India	74–77	5	OSL	[100]
80	Katoati	India	50–100 or older	5	OSL	[101]
81	Khotyk	Russia		5	TL	[82]
82	Myshtulagty Lagat	Russia	70–250	5–7	Ar/Ar, stratigraphy	[102]
83	Ust'-Izhul	Russia	~125	5	IRSL	[103]
84	Kara-Bom	Russia	~62	4	ESR	[95,104]
85	Shergarh Tri-Junction	India	60–43	4	OSL	[105,106]
86	Jinsitai	China	41–28	3	C-14	[107]
87	Okladnikov Cave	Russia	45–33	3	U-series, C-14	[104,108]
88	Shuidonggou Locality I	China	38–34	3	C-14	[109-111]
89	Tsagaan Agui	Mongolia	<70–90	5–3	TL	[112,113]

Supplementary Table 3 | Number of single grains or aliquots measured, rejected and accepted for each sample, together with the reasons for their rejection.

Sample	Grain size (μm)	Number of measured	Rejection criteria						Rejected	Accepted D_e values [b]	Proportion of saturated [c]
			T_n below 3σ above BG [a]	RSE of T_n > 20% [a]	Recuperation > 5%	Poor DRC [a]	D_e by extrapolation	No L_n/T_n intersection			
GYD-OSL1	90–150	800	224	221	3	199	22	32	701	99 (12%)	35%
	180–212	1000	619	272	1	85	1	8	986	14 (1%)	39%
GYD-OSL2	90–125	800	148	210	2	203	42	15	620	180 (23%)	24%
	180–212	4200	2820	979	11	291	2	12	4115	85 (2%)	14%
GYD-OSL3	90–125	600	138	134	0	187	19	24	502	98 (16%)	30%
	180–212	800	505	210	1	59	1	4	780	20 (3%)	20%
GYD-OSL4	90–180	1400	680	346	5	225	7	29	1292	108 (8%)	25%
GYD-OSL5	90–180	1500	631	451	4	274	19	29	1408	92 (6%)	34%
	180–212	1000	662	217	1	94	1	6	981	19 (2%)	27%
GYD-OSL6	90–180	1000	441	284	3	190	9	18	945	55 (6%)	33%
	180–212	800	558	170	1	56	0	0	785	15 (2%)	0%
GYD-OSL7	90–125	600	308	147	6	54	0	15	530	70 (12%)	18%
GYD-OSL8	90–125	500	147	116	16	92	0	25	396	104 (21%)	19%
GYD-OSL9	90–125	500	149	114	12	93	0	39	407	93 (19%)	30%
GYD-OSL10	90–125	1000	390	317	43	147	16	24	937	63 (6%)	39%
GYD-OSL11	90–125	600	248	222	15	77	6	9	577	23 (4%)	39%
GYD-OSL12	90–125	1000	412	269	28	148	14	24	895	105 (11%)	27%
GYD-OSL13	90–125	500	204	159	8	69	9	14	463	37 (7%)	38%

[a] BG, RSE and DRC represent background, relative standard error and dose response curve, respectively.
[b] The proportion of grains with acceptable D_e values is shown in the parentheses and was calculated as a ratio to the total number of measured grains.
[c] The proportion of saturated grains was calculated as the number of grains with D_e obtained by extrapolation and those without L_n/T_n intersection divided by the total number of grains that passed the first four criteria (columns 4–7).

Supplementary Table 4 | Summary of number of grains with saturated natural signal and D_e estimation results based on LS-normalised L_n/T_n for individual DRC groups and different grain sizes of each sample. All uncertainties are expressed at 1σ.

Sample	Grain size (μm)	DRC Group	Number of accepted DRCs	Number of saturated grains	Over-dispersion (%)	Age model [a]	D_e (Gy) [b]	Final D_e (Gy) [d]
S1								
GYD-OSL1	90–150	1	49	25	92 ± 9	FMM-2 (84%)	saturated	208 ± 14
		2	57	23	75 ± 7	FMM-2 (95%)	238 ± 31	
		3	47	7	114 ± 12	FMM-3 (72%)	199 ± 15	
	180–212	1	9	3	144 ± 36	nMAD (78%)	saturated	211 ± 27
		2	14	2	70 ± 14	nMAD (71%)	211 ± 27	
GYD-OSL2	90–125	1	21	11	40 ± 6	nMAD (90%)	saturated	224 ± 18
		2	66	26	69 ± 6	FMM-3 (89%)	204 ± 30	
		3	68	12	74 ± 7	FMM-4 (72%)	198 ± 20	
		4	82	9	99 ± 8	FMM-4 (67%)	260 ± 20	
	180–212	1	4	1	-	- [c]	-	198 ± 16
		2	32	10	59 ± 8	FMM-2 (91%)	157 ± 29	
		3	27	3	98 ± 14	FMM-3 (59%)	203 ± 33	
		4	36	2	139 ± 17	FMM-4 (53%)	211 ± 22	
GYD-OSL3	90–125	1	67	23	76 ± 7	FMM-4 (73%)	saturated	237 ± 13
		2	51	17	80 ± 8	FMM-2 (78%)	226 ± 15	
		3	23	4	50 ± 8	FMM-3 (65%)	258 ± 24	
	180–212	1	5	2	11 ± 5	CAM (100%)	saturated	206 ± 42
		2	20	3	207 ± 34	FMM-3 (55%)	206 ± 42	
GYD-OSL4	90–180	1	53	20	202 ± 22	FMM-4 (55%)	saturated	292 ± 50
		2	94	23	204 ± 16	FMM-4 (41%)	292 ± 50	
		3	2	0	135 ± 69	-	- [c]	
GYD-OSL5	90–180	1	16	9	14 ± 3	nMAD (75%)	saturated	224 ± 12
		2	72	28	29 ± 3	nMAD (88%)	232 ± 30	
		3	52	12	67 ± 7	FMM-3 (79%)	222 ± 13	
	180–212	1	7	5	3 ± 9	CAM (100%)	saturated	217 ± 36
		2	12	3	71 ± 16	FMM-2 (75%)	217 ± 36	
		3	7	0	126 ± 37	- [c]	-	
GYD-OSL6	90–180	1	42	20	74 ± 8	FMM-2 (93%)	saturated	168 ± 12
		2	40	7	81 ± 9	FMM-3 (80%)	168 ± 12	
	180–212	1	7	1	125 ± 39	- [c]	-	
		2	8	0	98 ± 26	- [c]	-	
GYD-OSL7	90-125	1	22	14	12 ± 3	nMAD (82%)	saturated	81 ± 4
		2	34	2	37 ± 5	nMAD (91%)	85 ± 5	
		3	29	0	59 ± 8	FMM-3 (72%)	74 ± 6	

Sample	Grain size (μm)	DRC Group	Number of accepted DRCs	Number of saturated grains	Over-dispersion (%)	Age model [a]	D_e (Gy) [b]	Final D_e (Gy) [d]
GYD-OSL8	90-125	1	31	22	12 ± 2	nMAD (87%)	saturated	99 ± 4
		2	36	3	24 ± 3	nMAD (78%)	109 ± 4	
		3	40	0	16 ± 2	nMAD (83%)	93 ± 3	
		4	22	0	36 ± 6	nMAD (82%)	93 ± 6	
GYD-OSL9	90-125	1	22	18	21 ± 4	nMAD (86%)	saturated	115 ± 5
		2	46	18	14 ± 2	nMAD (85%)	129 ± 39	
		3	39	4	23 ± 3	nMAD (87%)	122 ± 7	
		4	25	0	35 ± 5	nMAD (88%)	106 ± 7	
S2								
GYD-OSL10	90-125	1	25	18	9 ± 2	nMAD (96%)	saturated	272 ± 11
		2	34	13	27 ± 4	nMAD (88%)	248 ± 37	
		3	30	7	28 ± 4	nMAD (83%)	258 ± 29	
		4	14	2	36 ± 8	nMAD (79%)	276 ± 12	
GYD-OSL11	90-125	1	11	8	19 ± 5	CAM (100%)	saturated	201 ± 24
		2	16	3	45 ± 8	FMM-2 (75%)	181 ± 41	
		3	11	4	104 ± 23	nMAD (82%)	209 ± 29	
GYD-OSL12	90-125	1	32	16	16 ± 3	nMAD (88%)	saturated	202 ± 17
		2	41	12	27 ± 3	FMM-2 (37%)	saturated	
		3	50	8	29 ± 3	FMM-2 (66%)	192 ± 20	
		4	20	2	55 ± 9	FMM-3 (60%)	220 ± 30	
GYD-OSL13	90-125	1	14	7	11 ± 3	nMAD (93%)	saturated	214 ± 16
		2	24	14	20 ± 4	nMAD (71%)	290 ± 132	
		3	20	3	15 ± 3	nMAD (85%)	212 ± 16	
		4	2	0	9 ± 6	- [c]	-	

[a] The percentage of grains used for D_e estimation is shown in parentheses.
[b] The D_e shown as 'saturated' means that the weighted mean of LS-normalised L_n/T_n is statistically consistent with the saturation level of the corresponding SGC.
[c] The number of accepted grains are insufficient for reliable statistical analysis, i.e., there is less than 5 grains that are statistically identified from the same D_e component.
[d] The final D_e were obtained based on the weighted mean of the finite D_e values obtained from each of the groups.

Supplementary Table 5 | Dose rate data, equivalent doses (D_e) and OSL ages for sediment samples from the Guanyindong site.

Sample	Layer / Group	Depth (cm)	Grain size (μm)	Water content (%) [a]	Gamma dose rate (Gy/ka)	Beta dose rate (Gy/ka)	Cosmic dose rate (Gy/ka) [b]	Total dose rate (Gy/a)	D_e (Gy) [c]	Age (ka) [c]	Final age (ka) [c,d,e]
S1											
GYD-OSL7	1	10	90–125	20 ± 5 (17)	0.97 ± 0.03	0.99 ± 0.05	0.031	2.00 ± 0.05	81 ± 4	41 ± 2	41 ± 2
GYD-OSL8	1	50	90–125	20 ± 5 (14)	0.89 ± 0.02	1.18 ± 0.09	0.030	2.10 ± 0.09	99 ± 4	47 ± 3	47 ± 3
GYD-OSL9	1	75	90–125	20 ± 5 (11)	0.60 ± 0.02	1.04 ± 0.08	0.027	1.66 ± 0.08	115 ± 5	69 ± 5	69 ± 5
GYD-OSL1	4/B	210	90–150	30 ± 8 (20)	0.59 ± 0.05	0.69 ± 0.04	0.024	1.30 ± 0.07	208 ± 14	160 ± 14	161 ± 12
			180–212		0.59 ± 0.05	0.66 ± 0.04	0.024	1.28 ± 0.07	211 ± 27	165 ± 23	
GYD-OSL2	4/B	235	90–125	30 ± 8 (21)	0.39 ± 0.04	0.89 ± 0.06	0.023	1.30 ± 0.07	224 ± 18	173 ± 17	165 ± 12
			180–212		0.39 ± 0.04	0.84 ± 0.06	0.023	1.25 ± 0.07	198 ± 16	158 ± 15	
GYD-OSL3	5/B	245	90–125	30 ± 8 (24)	0.44 ± 0.04	0.97 ± 0.06	0.023	1.43 ± 0.08	237 ± 13	165 ± 13	163 ± 12
			180–212		0.44 ± 0.04	0.92 ± 0.06	0.023	1.38 ± 0.08	206 ± 42	149 ± 32	
GYD-OSL4	6/B	260	90–180	30 ± 8 (23)	0.49 ± 0.04	1.16 ± 0.08	0.022	1.67 ± 0.09	292 ± 50	175 ± 31	175 ± 32
GYD-OSL5	7/B	270	90–180	30 ± 8 (20)	0.42 ± 0.04	0.89 ± 0.06	0.022	1.34 ± 0.07	224 ± 12	167 ± 12	167 ± 12
			180–212		0.42 ± 0.04	0.87 ± 0.06	0.022	1.31 ± 0.07	217 ± 36	166 ± 29	
GYD-OSL6	8/B	290	90–180	30 ± 8 (20)	0.42 ± 0.04	0.54 ± 0.03	0.022	0.99 ± 0.05	168 ± 12	170 ± 14	170 ± 14
S2											
GYD-OSL10	2/A	80	90–125	30 ± 8 (28)	1.25 ± 0.03	1.59 ± 0.10	0.132	2.96 ± 0.11	272 ± 11	92 ± 5	92 ± 5
GYD-OSL11	2/A	95	90–125	30 ± 8 (32)	1.04 ± 0.02	1.54 ± 0.11	0.126	2.70 ± 0.11	201 ± 24	75 ± 9	75 ± 9
GYD-OSL12	2/A	120	90–125	30 ± 8 (31)	0.87 ± 0.02	1.28 ± 0.09	0.120	2.28 ± 0.09	202 ± 17	89 ± 8	89 ± 8
GYD-OSL13	2/A	190	90–125	30 ± 8 (30)	1.11 ± 0.02	1.36 ± 0.10	0.108	2.57 ± 0.10	214 ± 16	83 ± 7	83 ± 7

[a] Values used for dose rate and age calculations, with measured (field) water contents shown in parentheses.
[b] Values after correction for the zenith angular distribution of cosmic rays.
[c] The uncertainties provided after the ± symbol represent the uncertainty at 1σ.
[d] A systematic error of 2% was added (in quadrature) to the propagated random errors in the final ages to allow for any bias associated with the calibration of the laboratory beta sources.
[e] For samples with two grain sizes measured, their final ages were obtained based on the weighted mean of the ages obtained from each of the two grain sizes.

SI section 4

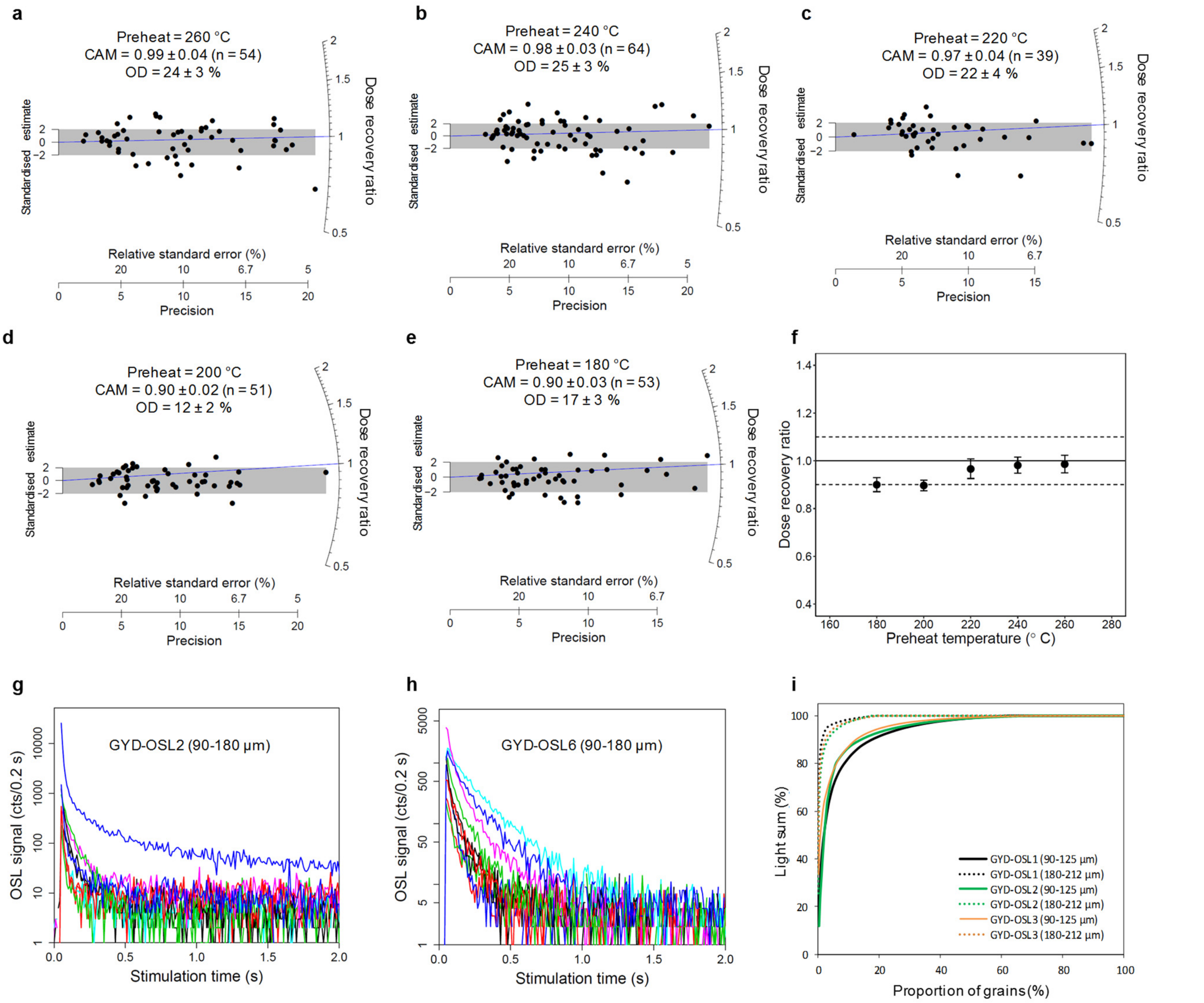

Supplementary Figure 1 | Dose recovery results and luminescence characteristics. a–e, Radial plots showing the distributions of dose recovery ratios for individual grains from GYD-OSL2 using different preheat temperatures (from 260 to 180 °C, respectively) and the corresponding CAM and OD values. **f,** The weighted mean dose recovery ratios obtained from panels a–e plotted against preheat temperature. The vertical bars represent 1σ standard error. **g–h,** Selected typical natural OSL decay curves of 10 grains from each of samples GYD-OSL2 and -OSL6, respectively. **i,** Distribution of OSL signal intensities for individual quartz grains for different grain sizes from samples GYD-OSL1, -OSL2 and -OSL3. Data are plotted as the proportion of the total light sum that originates from the specified percentage of grains.

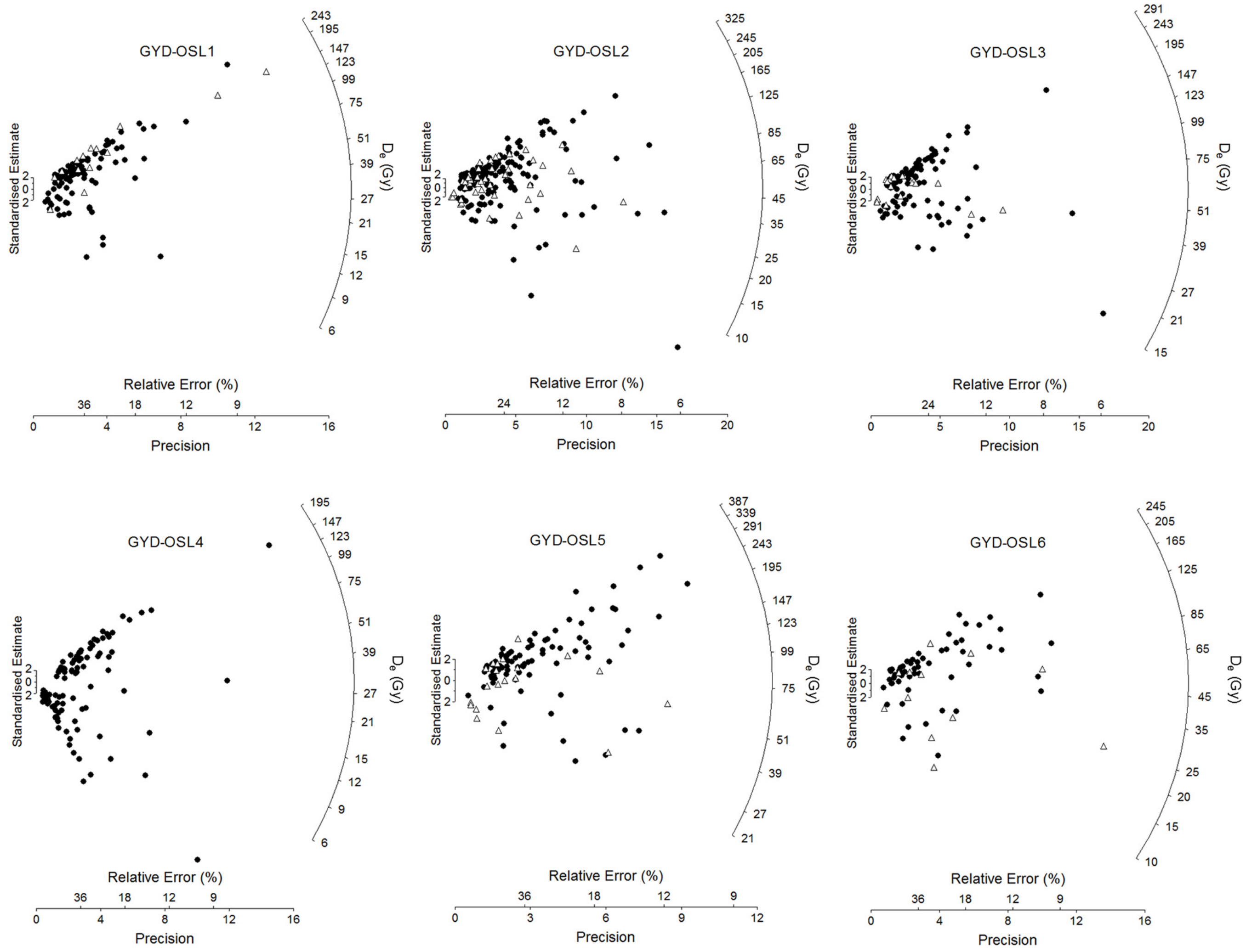

Supplementary Figure 2 | Single-grain SAR D_e results for all the OSL samples. For those samples (GYD-OSL1, 2, 3, 5 and 6) where two grain sizes were measured, the filled circles are the results from the 180–212 µm size fraction and the open triangles are those from the smaller grain size (< 180 µm). See the next page for more figures.

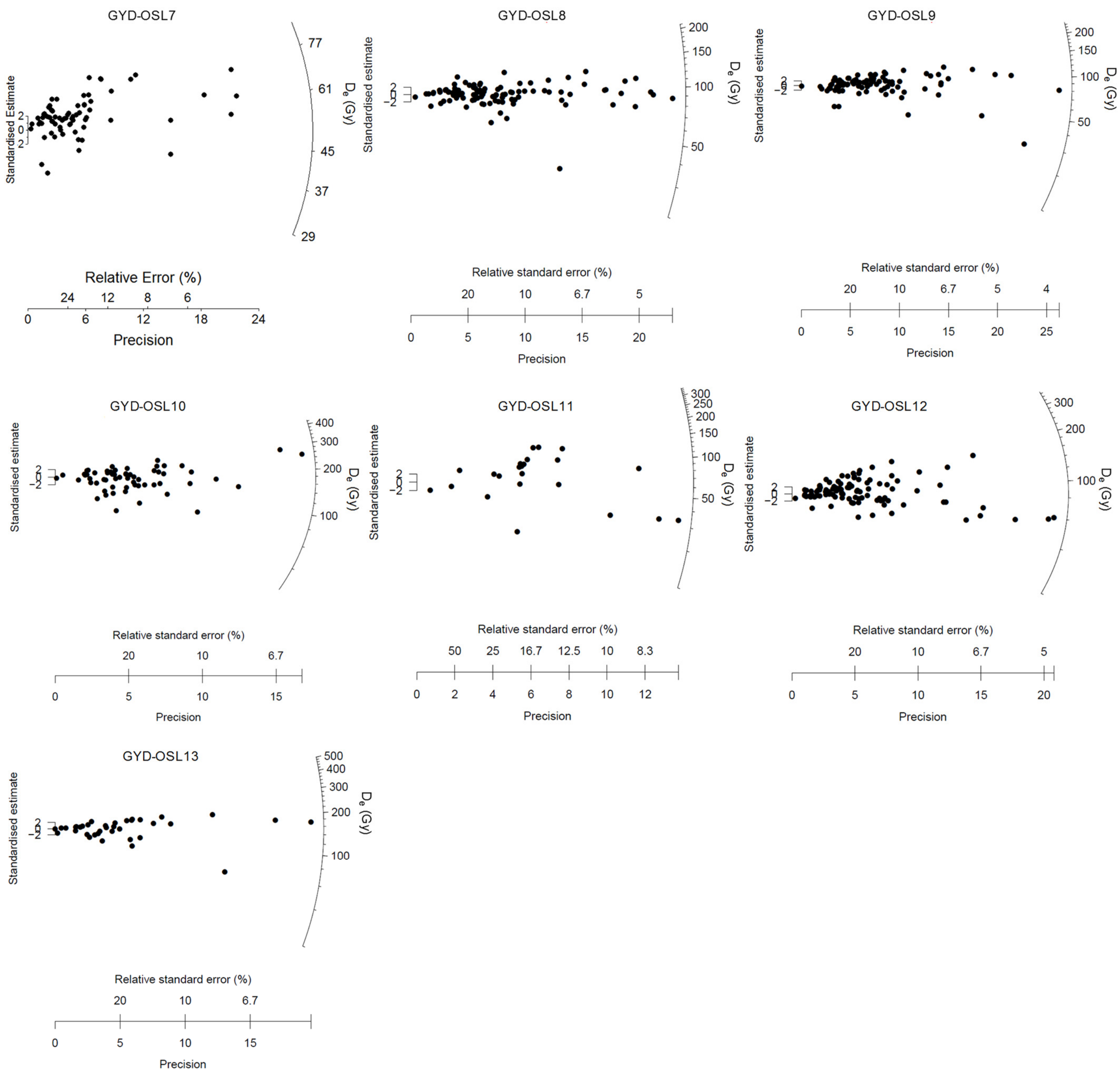

Supplementary Figure 2 continued | see the previous page for caption.

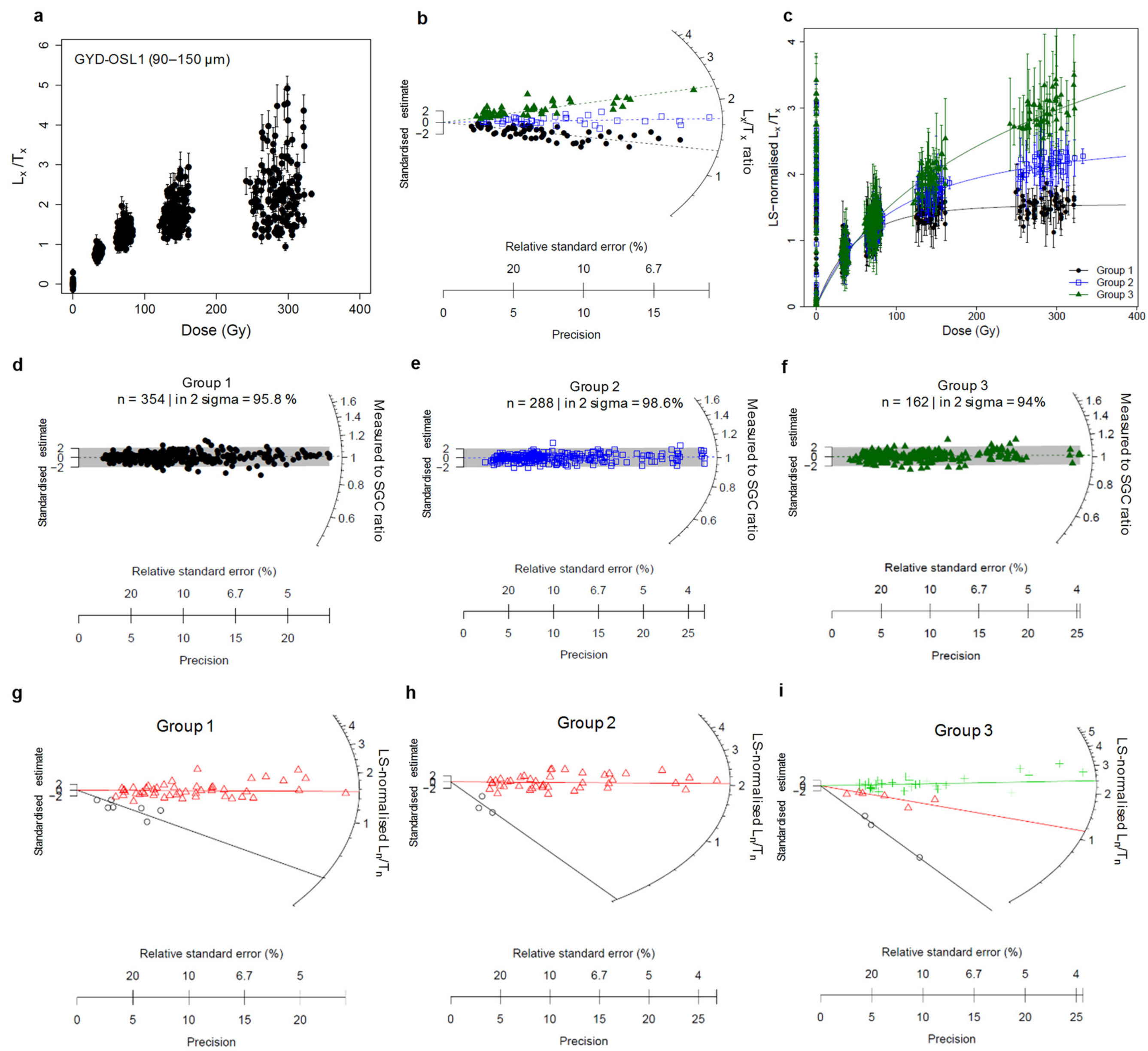

Supplementary Figure 3 | Single-grain DRCs and SGC results for the 90–150 µm grains of sample GYD-OSL1. a, Comparisons of all the DRCs that pass the rejection criteria. **b,** Radial plot showing the distribution of the ratios of L_x/T_x values between two regenerative doses of ~280 and ~70 Gy for all the accepted grains. Different symbols represent different groups of grains identified using FMM. **c,** Comparison of the LS-normalised L_n/T_n and L_x/T_x for different groups. The data set for each group were fitted using a GOK function (full lines) and then normalised to unity at 50 Gy. **d–f,** Radial plots showing the ratios between the LS-normalised L_x/T_x and the expected values from the best-fit SGCs shown in panel c; the shaded band captures 2σ range from unity. The total number of grains (n) and percentage falling inside the 2σ band are shown for each group. **g–i,** Radial plots showing the LS-normalised natural signals (L_n/T_n); different age groups were identified using FMM and distinguished using different symbols. The full lines represent the central values of individual groups obtained using FMM. All the figures and data analysis were based on the building functions in R packages "Luminescence" [114] and "numOSL" [115]. All the error bars in panels a and c represent 1σ standard error.

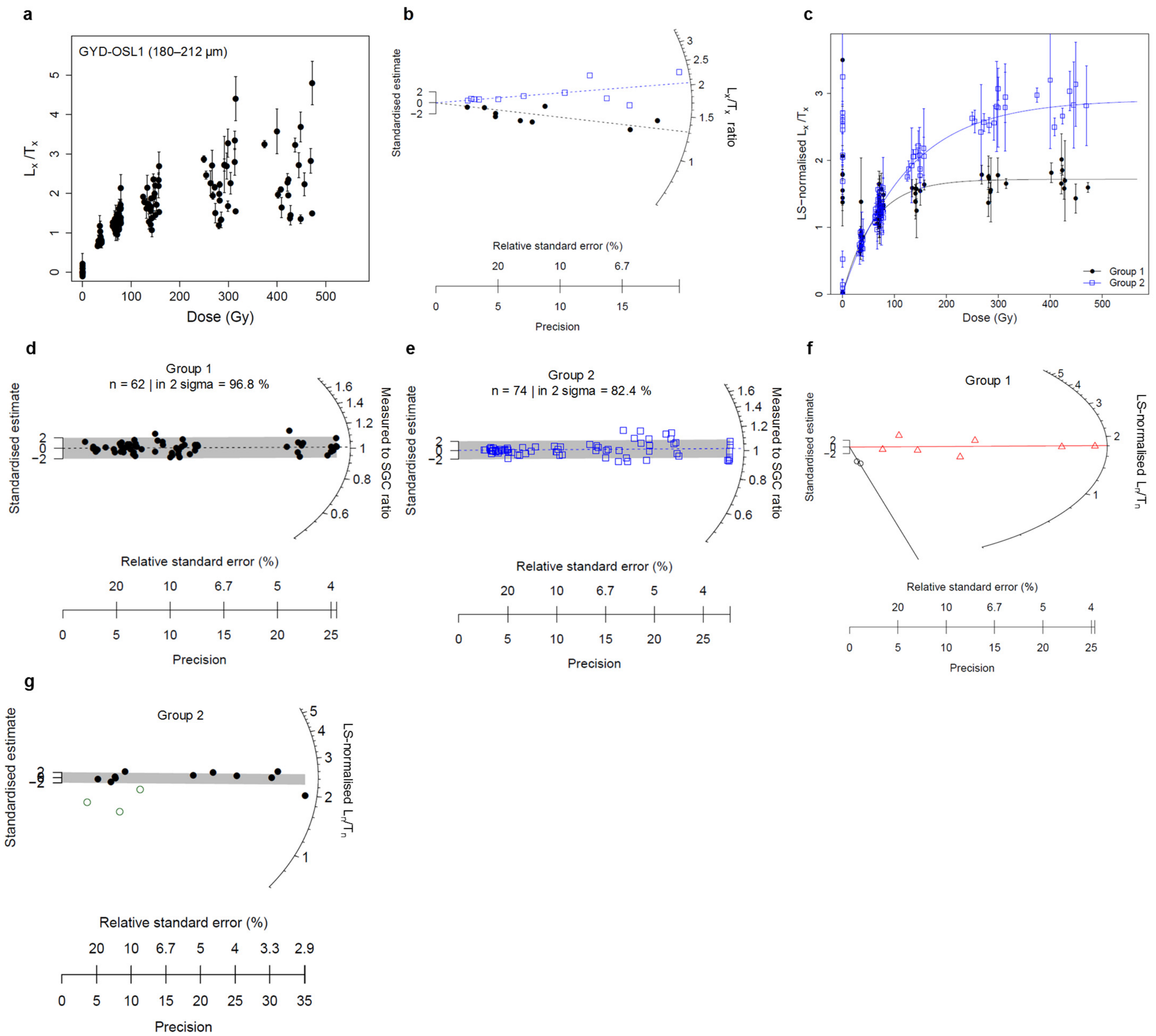

Supplementary Figure 4 | Single-grain measurement results for the 180–212 µm fraction of sample GYD-OSL1. a–c, Results similar to those described in Supplementary Figs 3a–c. **d–e,** Results similar to those described in Supplementary Figs 3d–f. **f,** Results similar to those described in Supplementary Figs 3g–i. **g,** Radial plots showing the LS-normalised natural signals (L_n/T_n) for group 2; this distribution contains a small number of intrusive grains (open circles) identified as outliers using nMAD, so only the data points shown in filled circles were included in the final weighted mean L_n/T_n value calculated using the CAM.

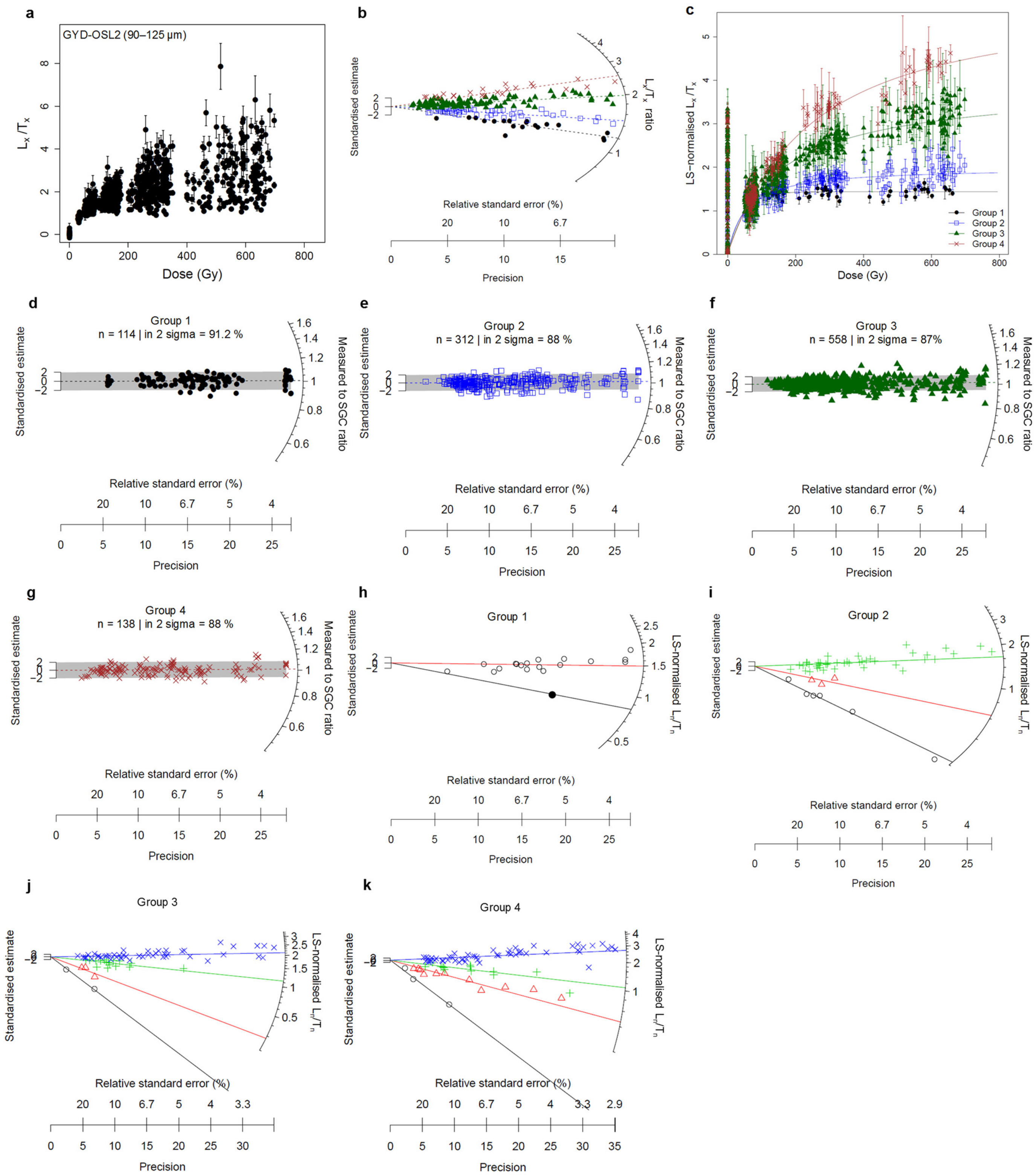

Supplementary Figure 5 | Single-grain measurement results for the 90–125 µm fraction of sample GYD-OSL2. a–c, Results similar to those described in Supplementary Figs 3a–c. **d–g,** Results similar to those described in Supplementary Figs 3d–f. **h–k,** Results similar to those described in Supplementary Figs 3g–i.

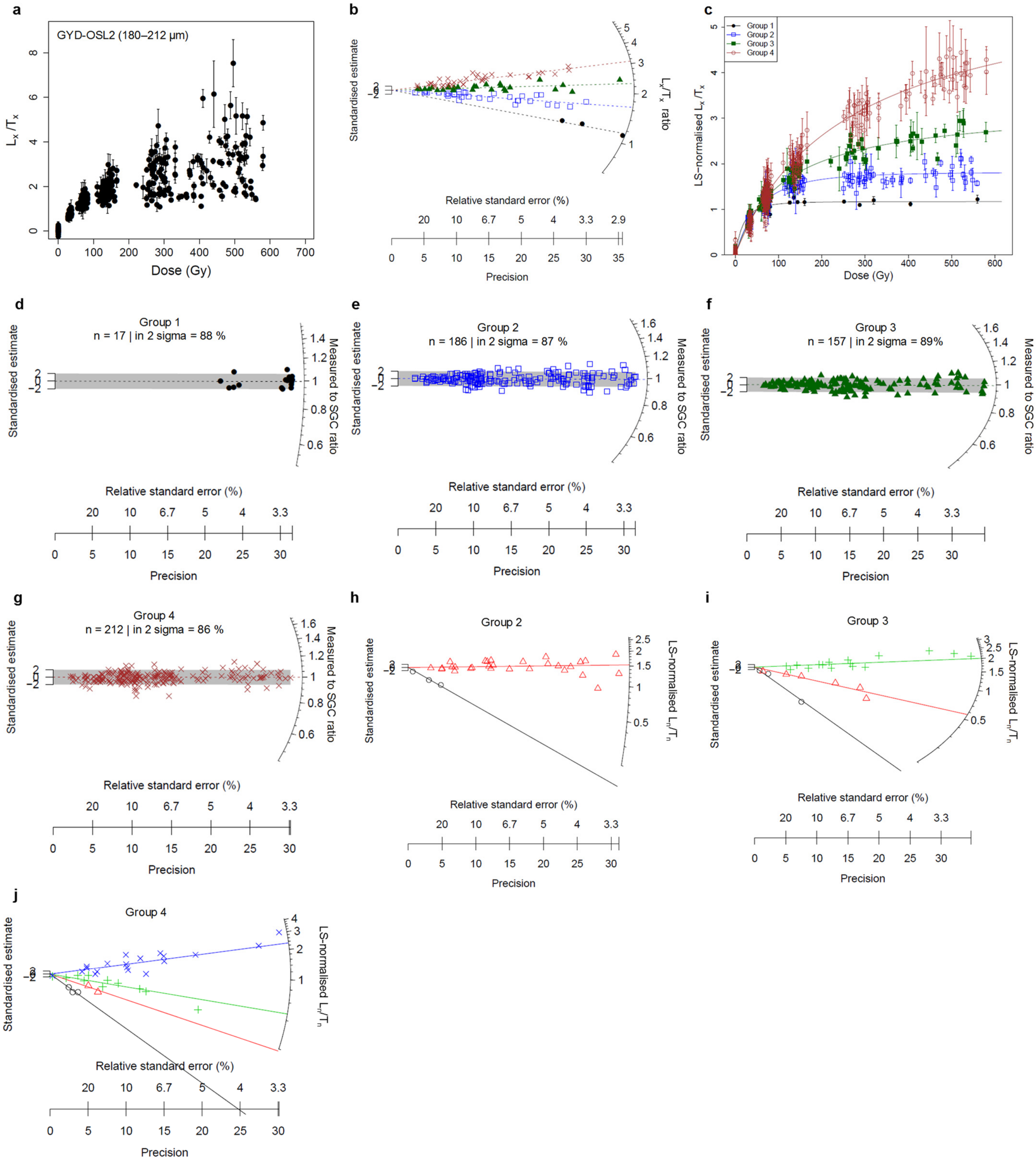

Supplementary Figure 6 | Single-grain measurement results for the 180–212 µm fraction of sample GYD-OSL2. a–c, Results similar to those described in Supplementary Figs 3a–c. **d–g,** Results similar to those described in Supplementary Figs 3d–f. **h–j,** Results similar to those described in Supplementary Figs 3g–i. Note that only 3 grains were identified as group 1 and all are 'modern' grains, so their natural signals are not plotted here.

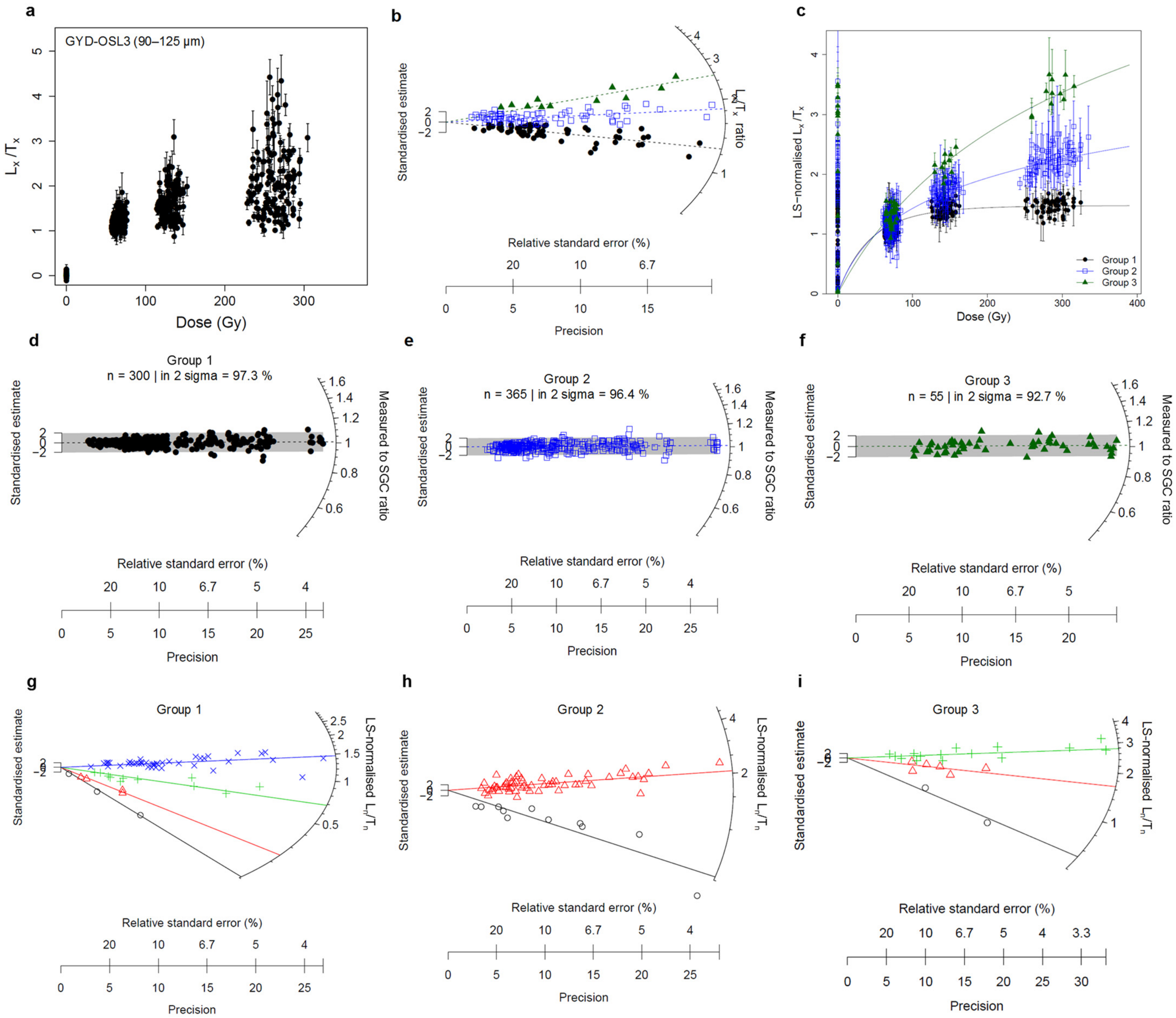

Supplementary Figure 7 | Single-grain measurement results for the 90–125 µm fraction of sample GYD-OSL3. a–c, Results similar to those described in Supplementary Figs 3a–c. **d–f,** Results similar to those described in Supplementary Figs 3d–f. **g–i,** Results similar to those described in Supplementary Figs 3g–i.

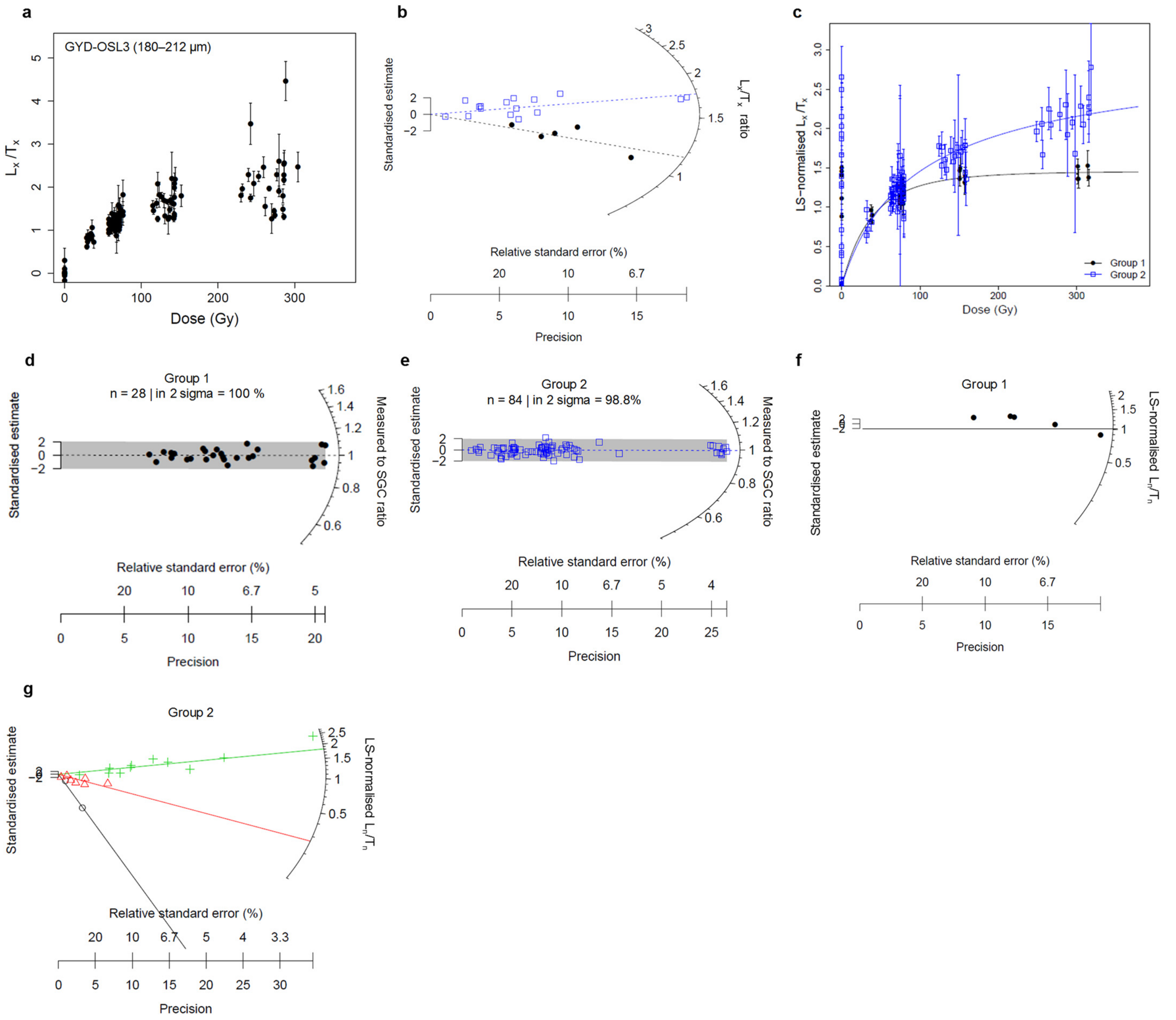

Supplementary Figure 8 | Single-grain measurement results for the 180–212 μm fraction of sample GYD-OSL3. a–c, Results similar to those described in Supplementary Figs 3a–c. **d–e,** Results similar to those described in Supplementary Figs 3d–f. **f–g,** Results similar to those described in Supplementary Figs 3g–i.

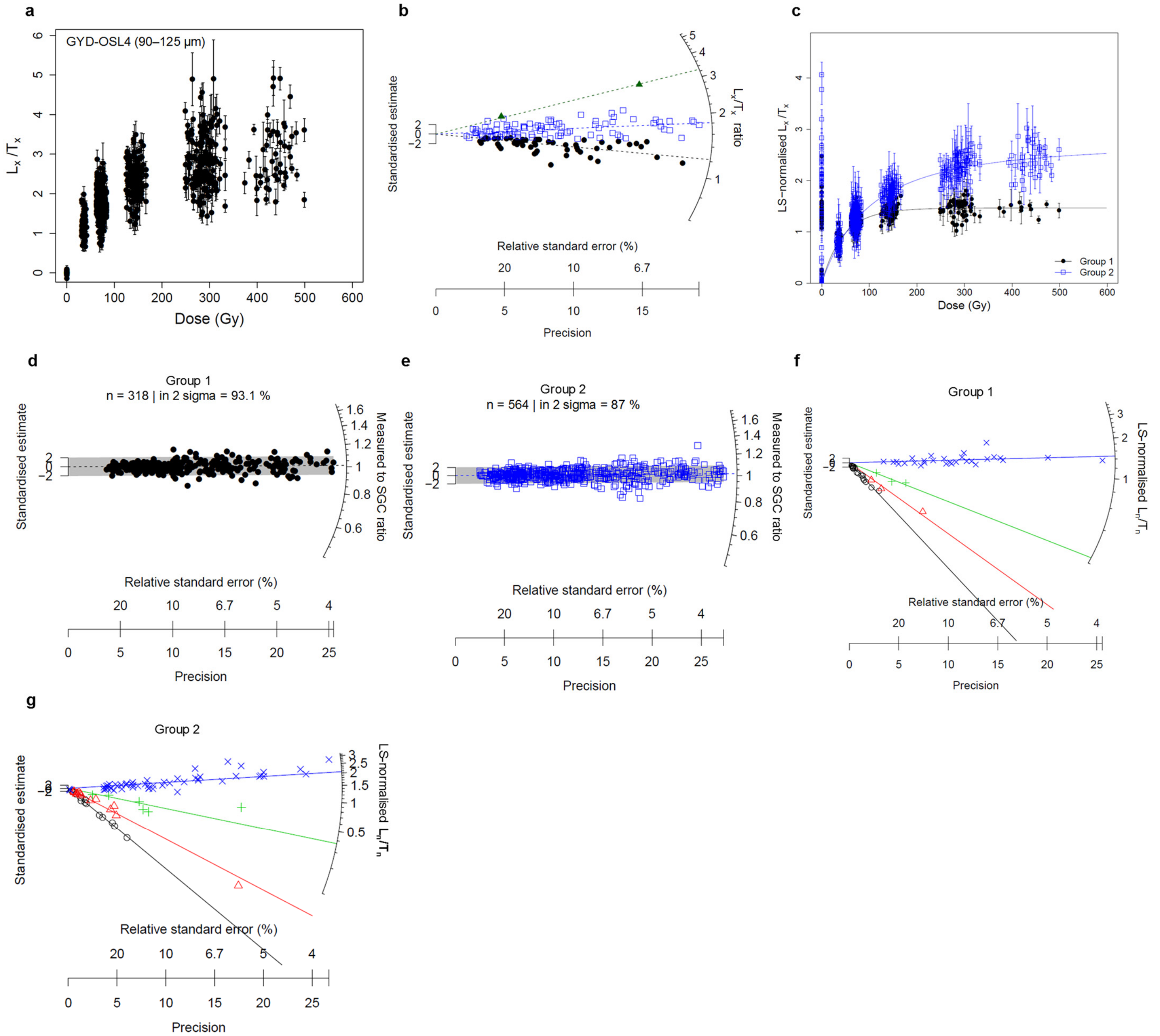

Supplementary Figure 9 | Single-grain measurement results for the 90–125 µm fraction of sample GYD-OSL4. a–c, Results similar to those described in Supplementary Figs 3a–c. **d–e,** Results similar to those described in Supplementary Figs 3d–f. **f–g**, Results similar to those described in Supplementary Figs 3g–i.

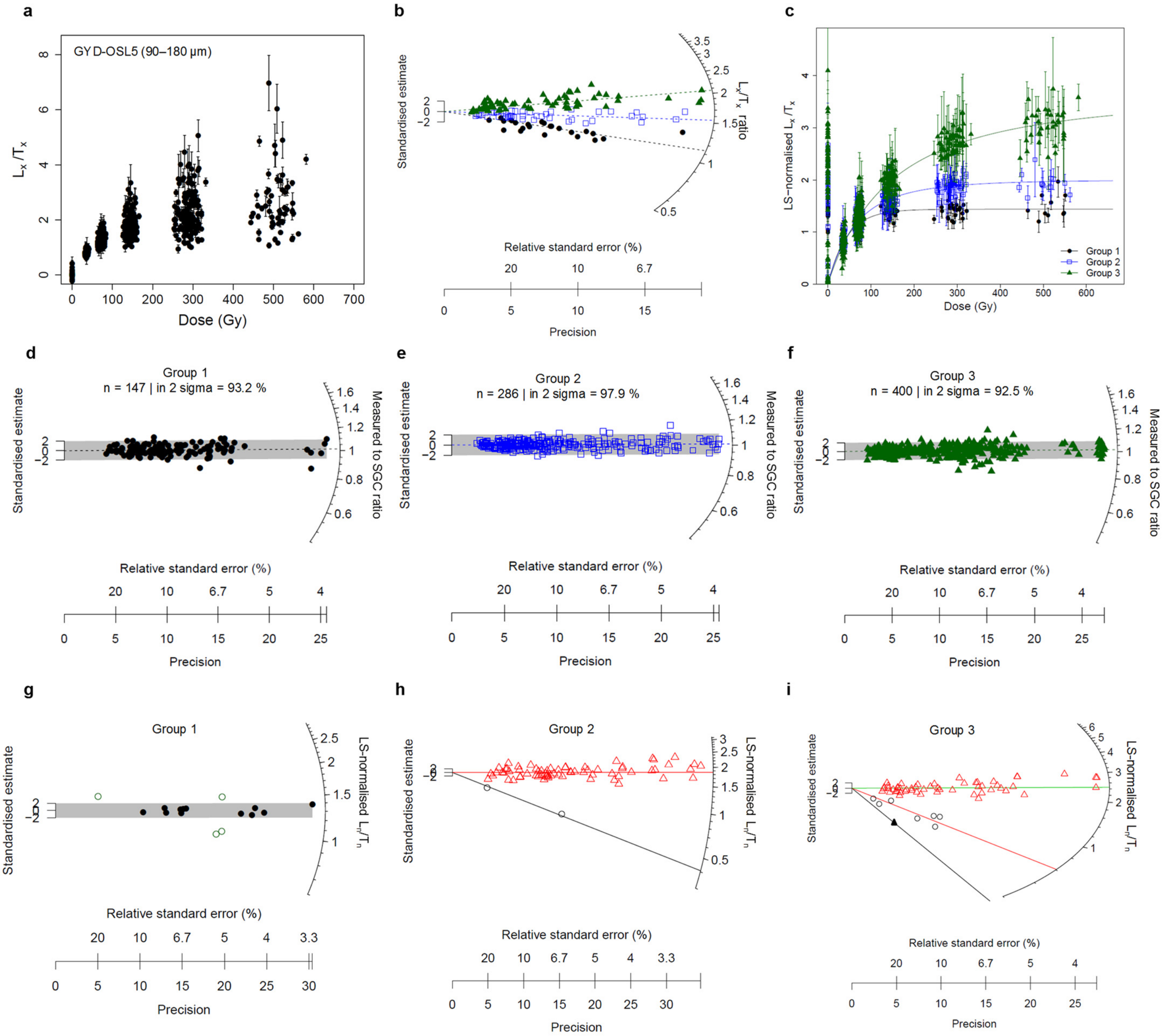

Supplementary Figure 10 | Single-grain measurement results for the 90–180 µm fraction of sample GYD-OSL5. a–c, Results similar to those described in Supplementary Figs 3a–c. **d–f,** Results similar to those described in Supplementary Figs 3d–f. **g,** Results similar to those described in Supplementary Fig. 4g. **h–i,** Results similar to those described in Supplementary Figs 3g–i.

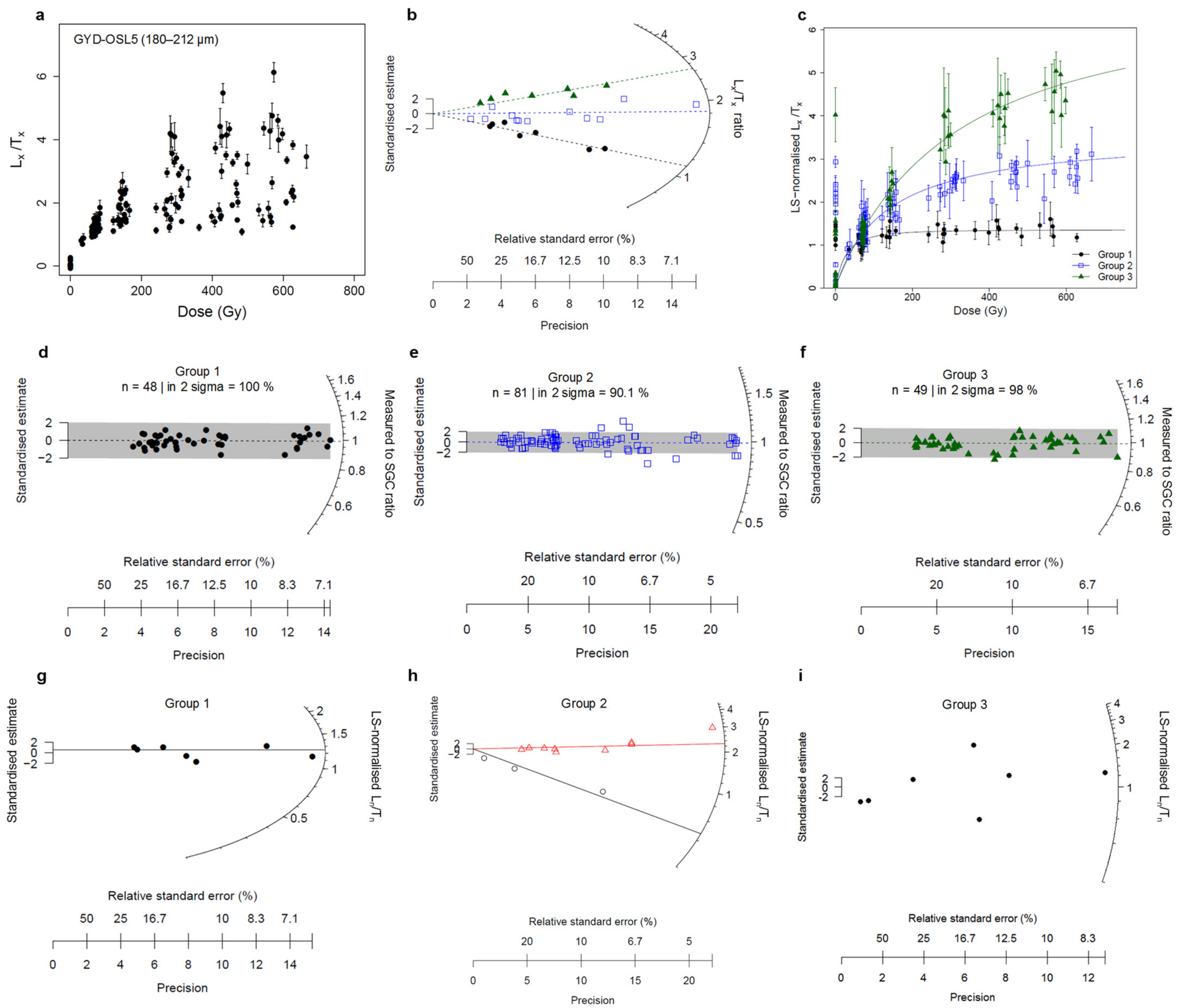

Supplementary Figure 11 | Single-grain measurement results for the 180–212 μm fraction of sample GYD-OSL5. a–c, Results similar to those described in Supplementary Figs 3a–c. **d–f,** Results similar to those described in Supplementary Figs 3d–f. **g–h,** Results similar to those described in Supplementary Figs 3g–i. **i,** Radial plots showing the LS-normalised natural signals (L_n/T_n) for group 3; the data sets of this group are too scattered and too few to apply any age model reliably.

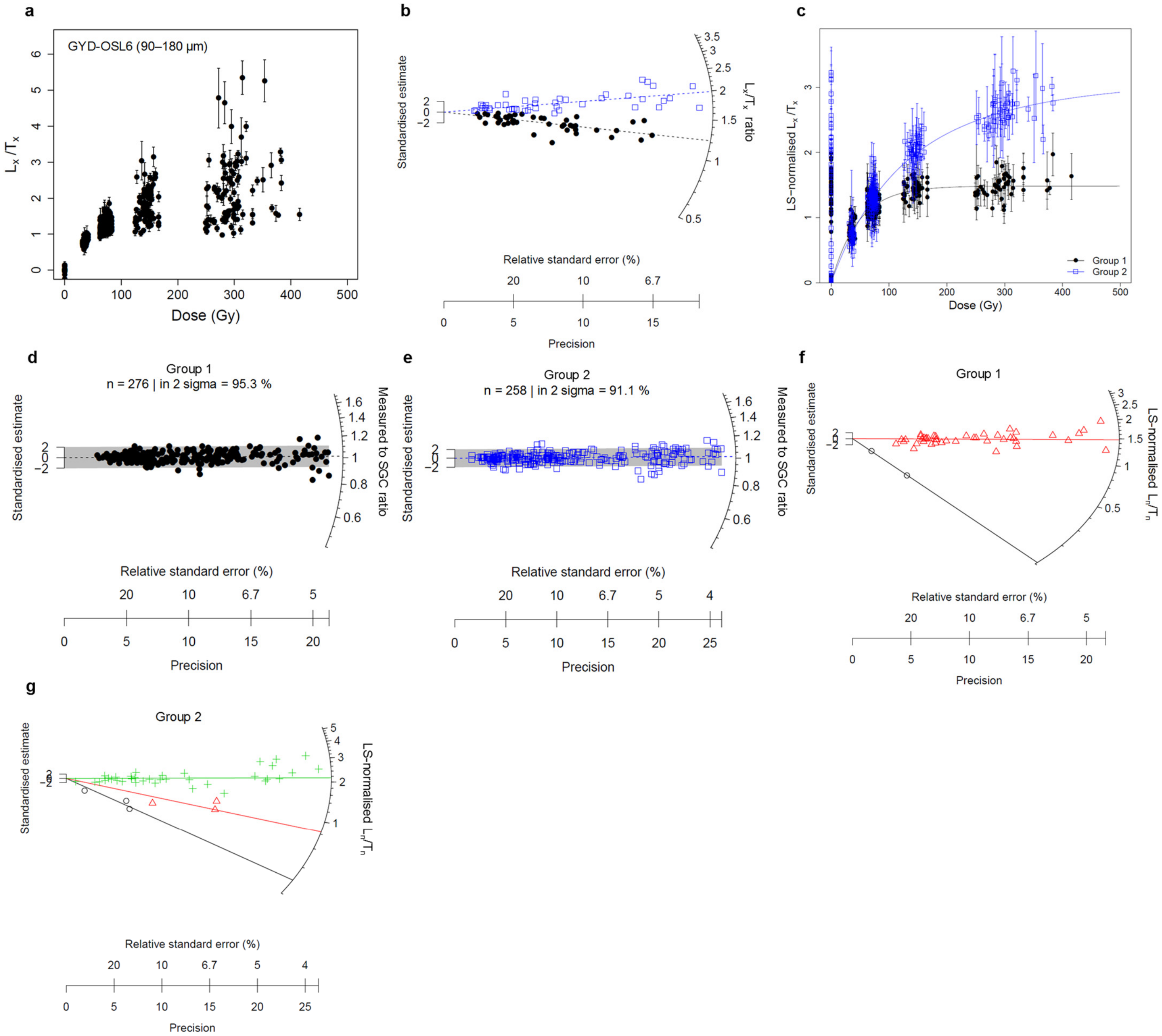

Supplementary Figure 12 | Single-grain measurement results for the 90–180 µm fraction of sample GYD-OSL6. a–c, Results similar to those described in Supplementary Figs 3a–c. **d–e,** Results similar to those described in Supplementary Figs 3d–f. **f–g,** Results similar to those described in Supplementary Figs 3g–i.

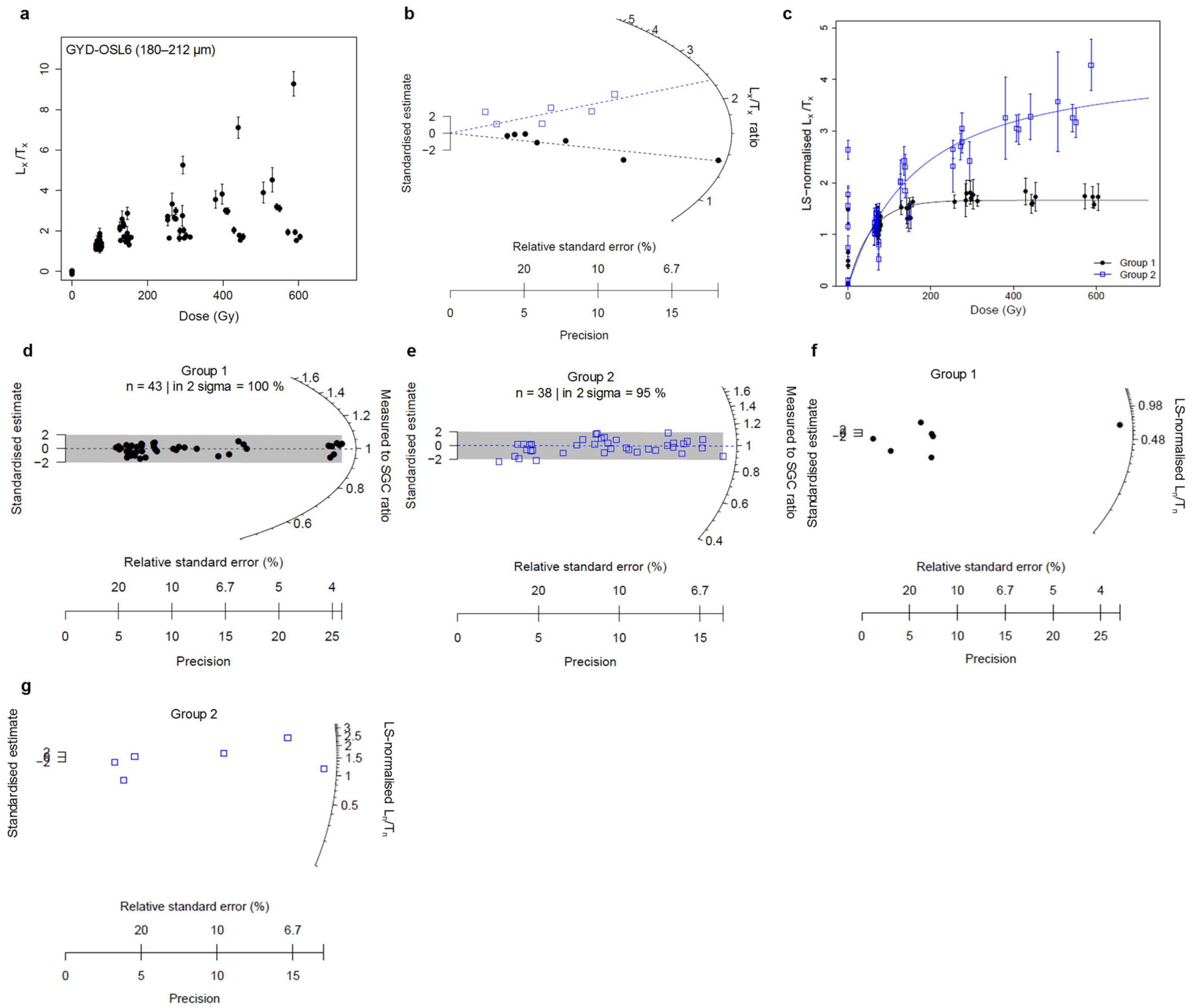

Supplementary Figure 13 | Single-grain measurement results for the 180–212 µm fraction of sample GYD-OSL6. a–c, Results similar to those described in Supplementary Figs 3a–c. **d–e,** Results similar to those described in Supplementary Figs 3d–f. **f–g,** Results similar to those described in Supplementary Fig. 11i.

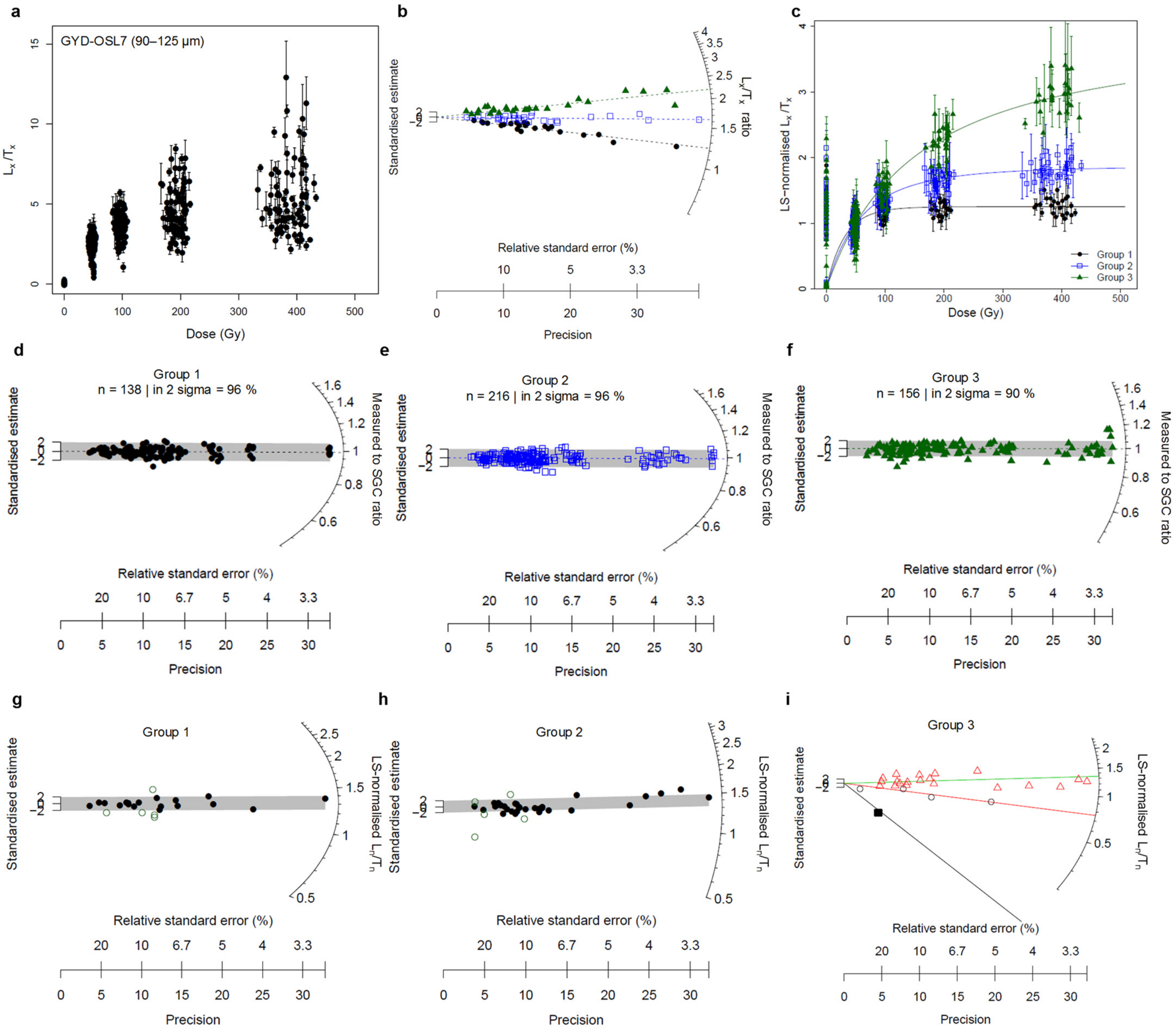

Supplementary Figure 14 | Single-grain measurement results for the 90–125 µm fraction of sample GYD-OSL7. a–c, Results similar to those described in Supplementary Figs 3a–c. **d–f,** Results similar to those described in Supplementary Figs 3d–f. **g–h,** Results similar to those described in Supplementary Fig. 4g. **i,** Results similar to those described in Supplementary Figs 3g-i.

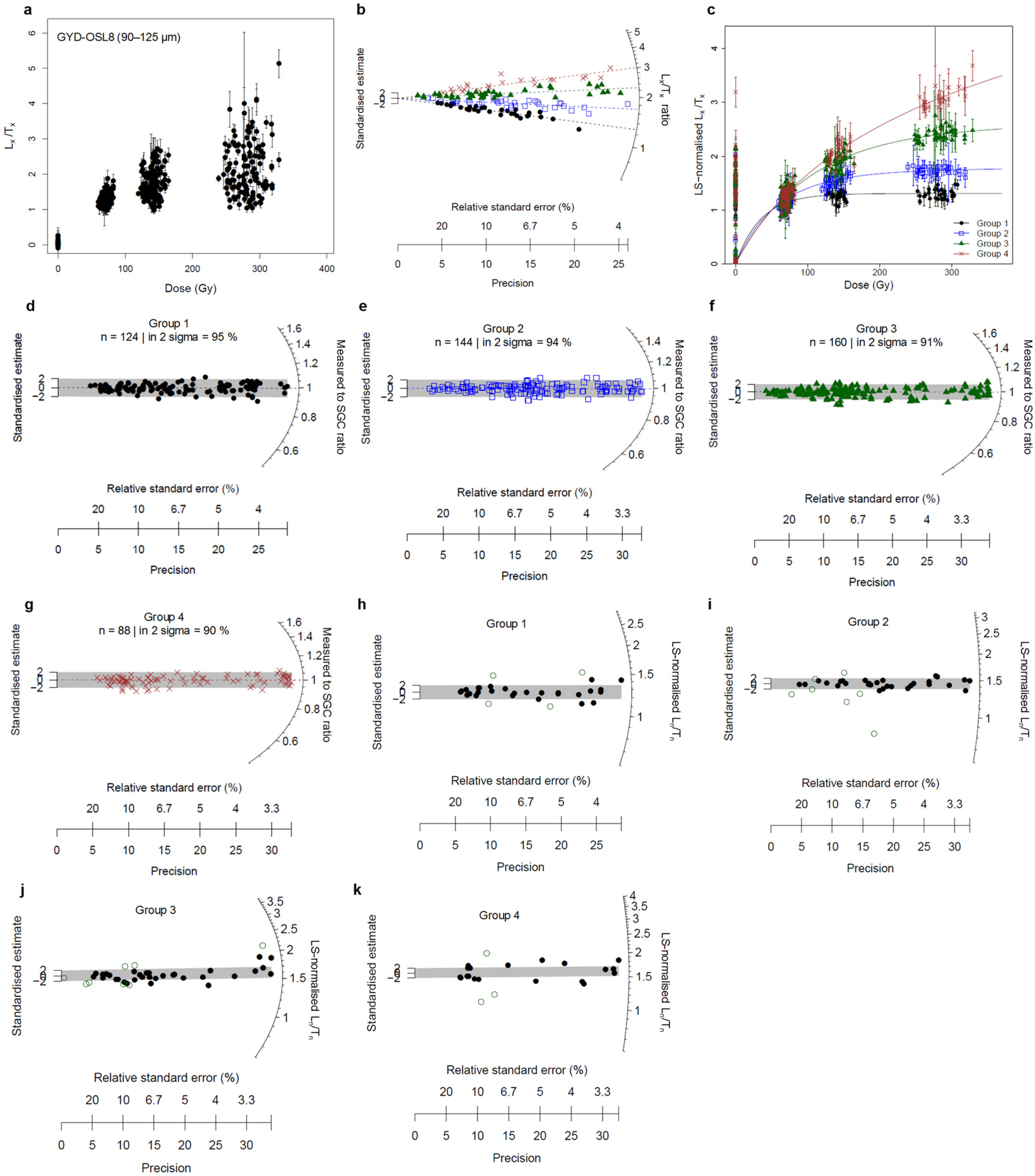

Supplementary Figure 15 | Single-grain measurement results for the 90–125 µm fraction of sample GYD-OSL8. a–c, Results similar to those described in Supplementary Figs 3a–c. **d–g**, Results similar to those described in Supplementary Figs 3d–f. **h–k,** Results similar to those described in Supplementary Fig. 4g.

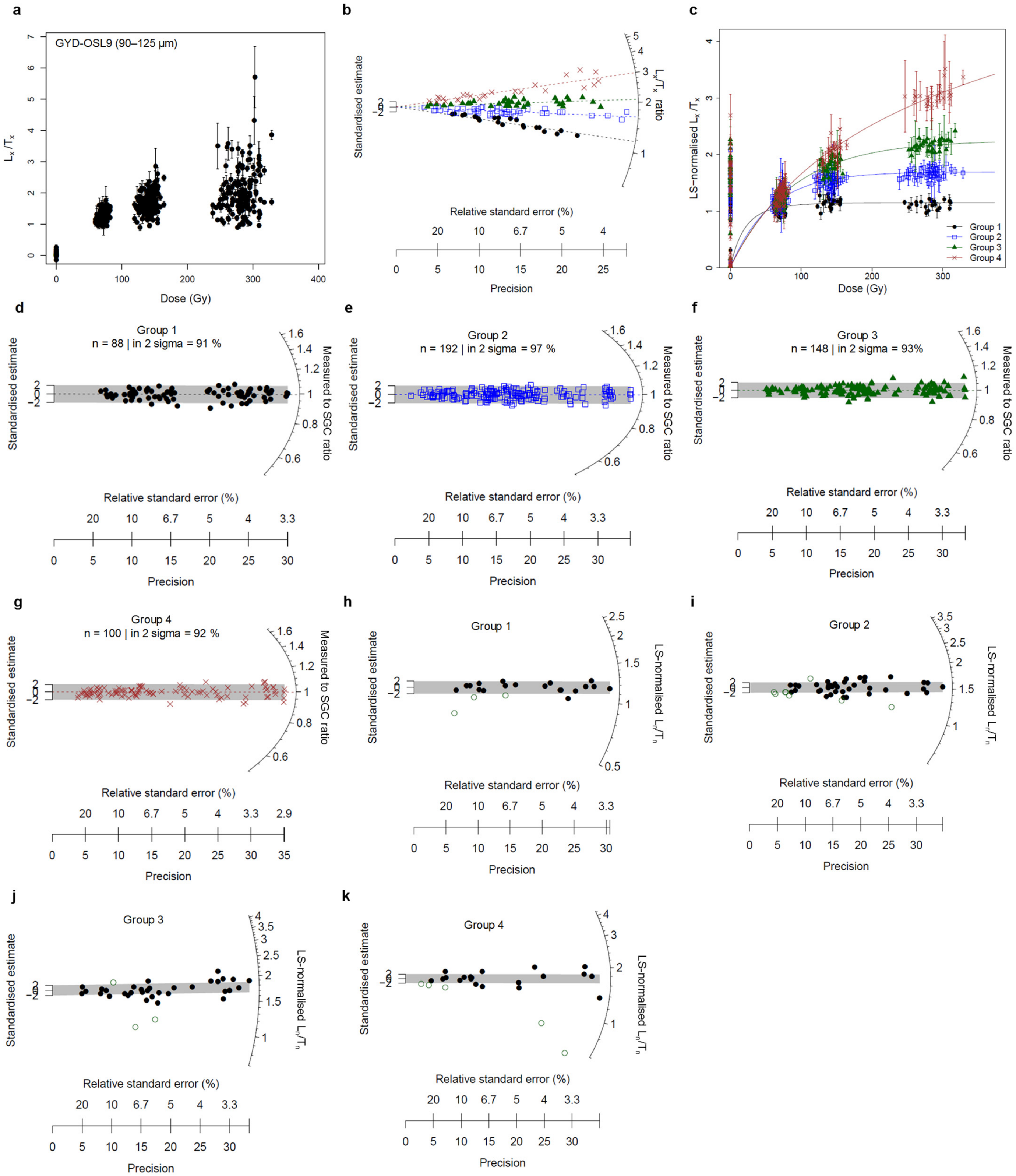

Supplementary Figure 16 | Single-grain measurement results for the 90–125 µm fraction of sample GYD-OSL9. a–c, Results similar to those described in Supplementary Figs 3**a–c**. **d–g,** Results similar to those described in Supplementary Figs 3**d–f**. **h–k,** Results similar to those described in Supplementary Fig. 4g.

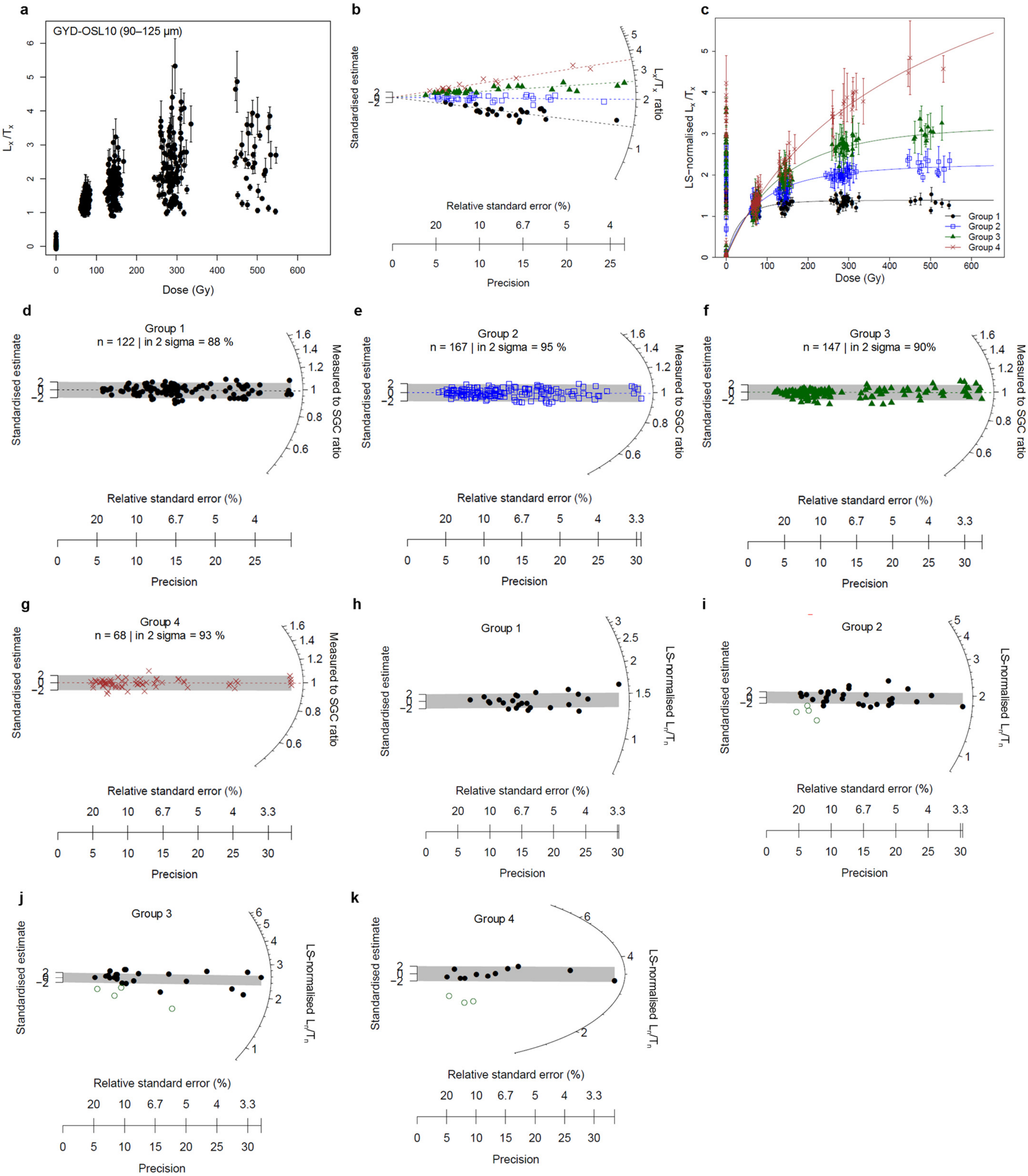

Supplementary Figure 17 | Single-grain measurement results for the 90–125 µm fraction of sample GYD-OSL10. a–c, Results similar to those described in Supplementary Figs 3a–c. **d–g,** Results similar to those described in Supplementary Figs 3d–f. **h–k,** Results similar to those described in Supplementary Fig. 4g.

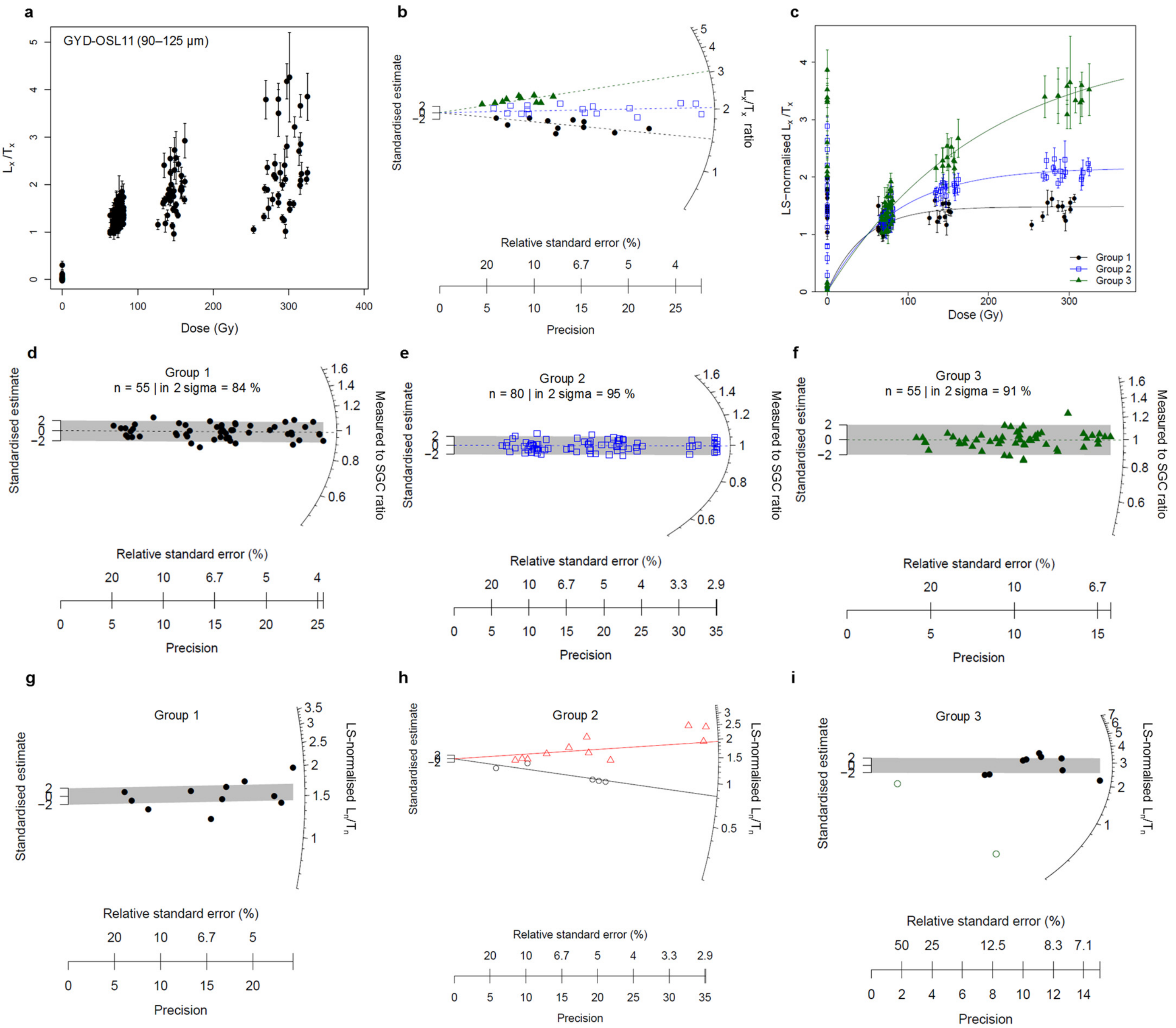

Supplementary Figure 18 | Single-grain measurement results for the 90–125 µm fraction of sample GYD-OSL11. a–c, Results similar to those described in Supplementary Figs 3a–c. **d–f,** Results similar to those described in Supplementary Figs 3d–f. **g–i,** Results similar to those described in Supplementary Figs 3g–i and 4g.

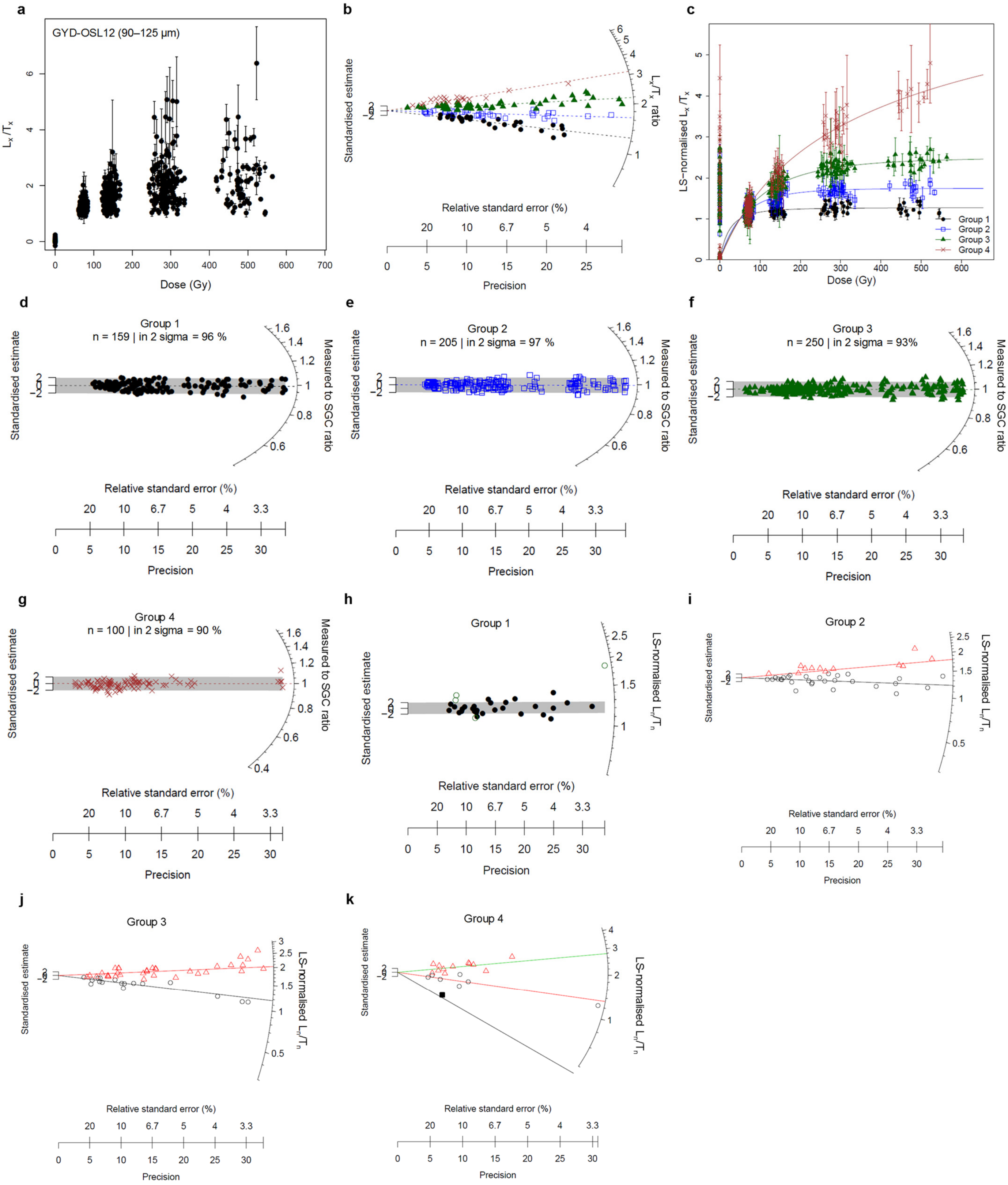

Supplementary Figure 19 | Single-grain measurement results for the 90–125 µm fraction of sample GYD-OSL12. a–c, Results similar to those described in Supplementary Figs 3a–c. **d–g,** Results similar to those described in Supplementary Figs 3d–f. **h–k,** Results similar to those described in Supplementary Figs 3g–i and 4g.

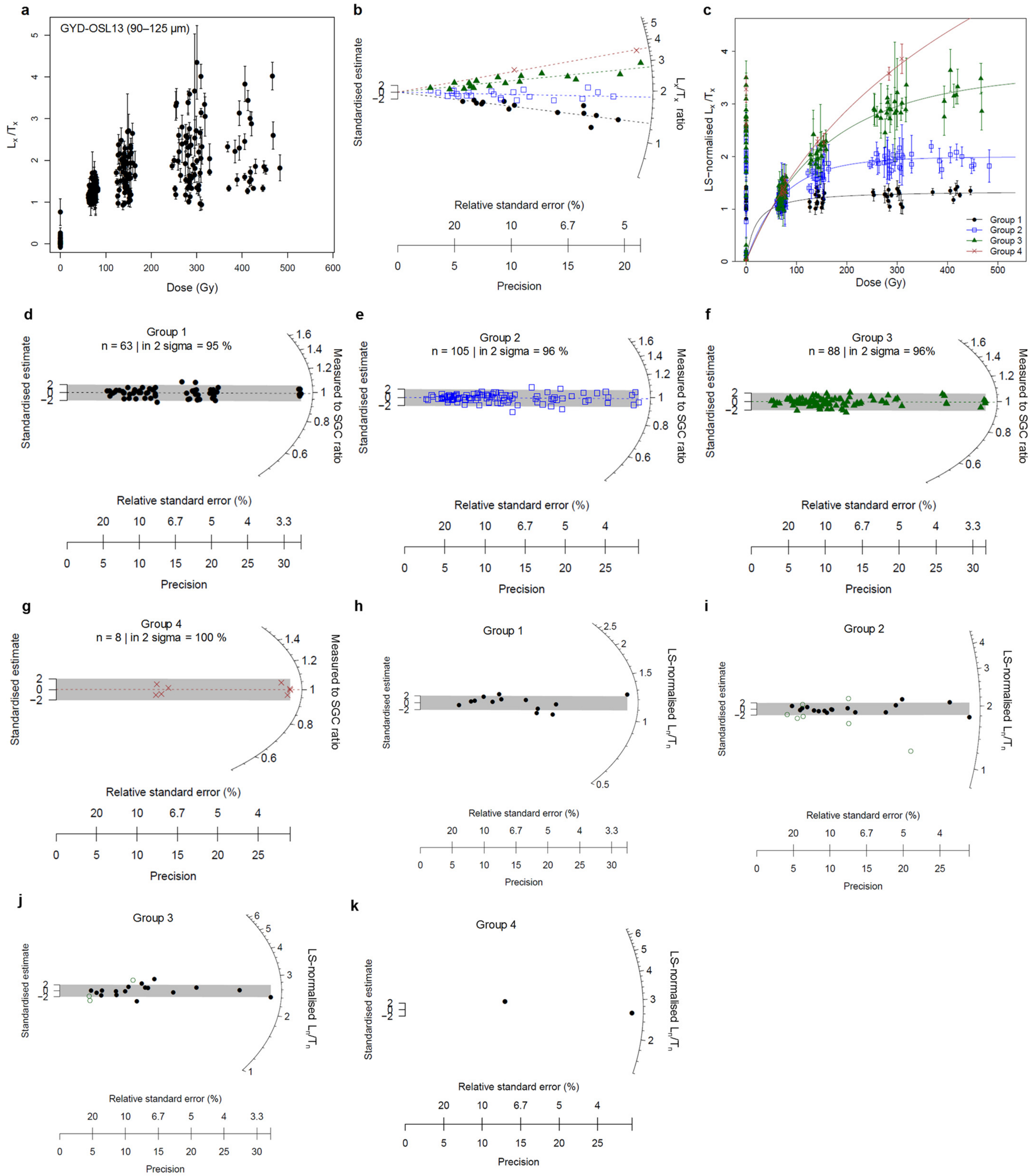

Supplementary Figure 20 | Single-grain measurement results for the 90–125 μm fraction of sample GYD-OSL13. a–c, Results similar to those described in Supplementary Figs 3a–c. **d–g,** Results similar to those described in Supplementary Figs 3d–f. **h–j,** Results similar to those described in Supplementary Fig. 4g. **k,** Results similar to those described in Supplementary Figs 11i.

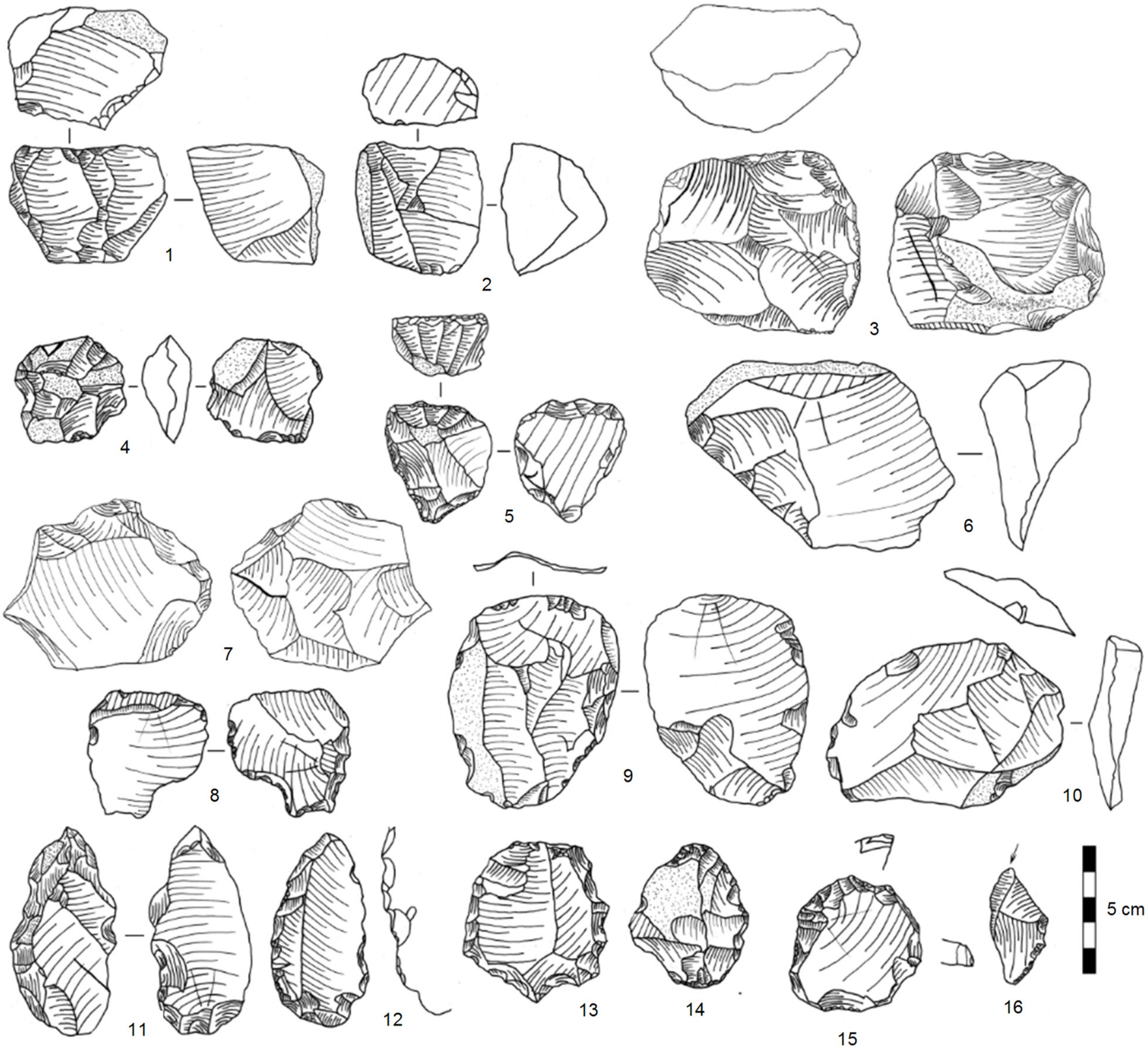

Supplementary Figure 21 | Line drawings of selected non-Levallois artefacts. 1, Single platform core. **2,** Double platform core. **3–4,** Discoid cores. **5,** Blade core. **6, 7,** Truncated facetted pieces. **8,** Kombewa flake. **9, 10, 14,** Flakes. **11 and 13,** Denticulates. **12,** Convergent scraper. **15,** Double scrapers. **16,** Burin. The photos of these artefacts are shown in Supplementary Fig. 22.

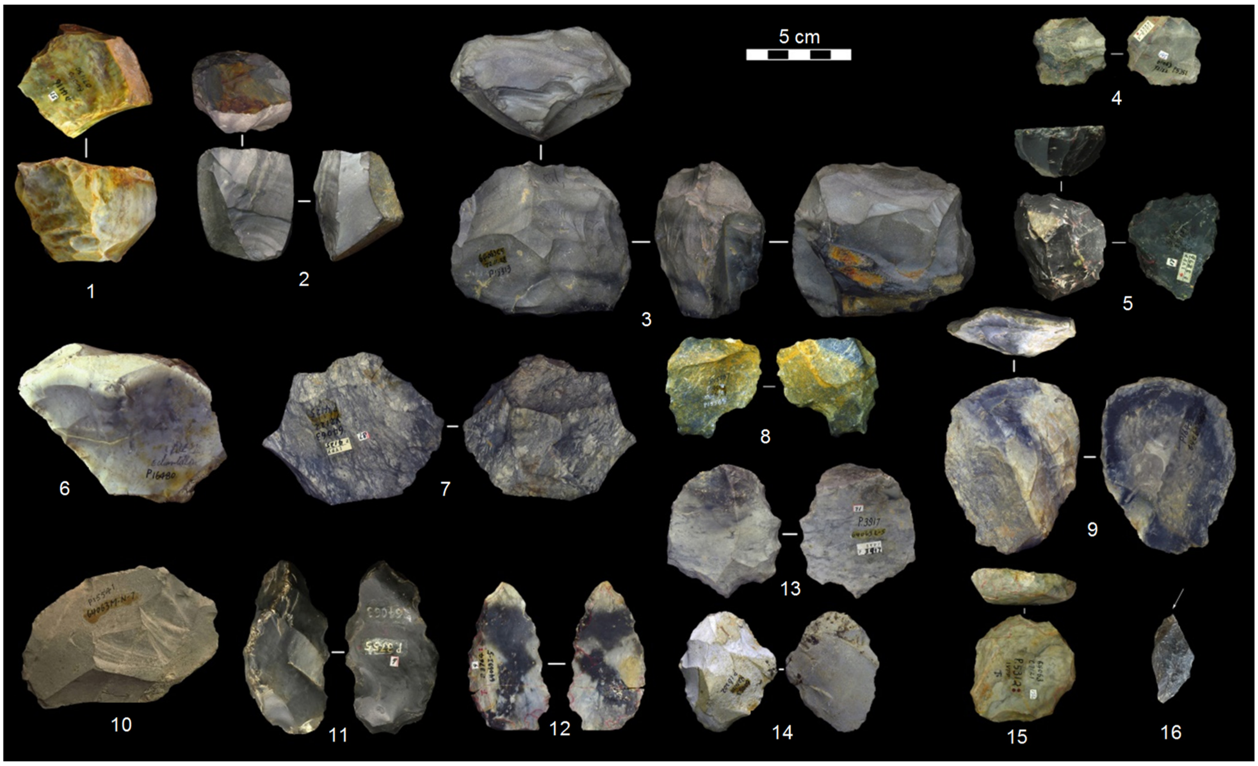

Supplementary Figure 22 | Photos of selected non-Levallois artefacts. 1, Single platform core. **2,** Double platform core. **3–4,** Discoid cores. **5,** Blade core. **6, 7,** Truncated facetted pieces. **8,** Kombewa flake. **9, 10, 14,** Flakes. **11 and 13,** Denticulates. **12,** Convergent scraper. **15,** Double scrapers. **16,** Burin. The line drawings of these artefacts are shown in Supplementary Fig. 21.

Supplementary Figure 23 | Photos of selected non-Levallois artefacts. 1–2, Blade cores. **3,** Truncated facetted pieces. **4–5,** Bifaces. **6–10,** Flakes.

Supplementary Figure 24 | Photos of selected non-Levallois artefacts. 1–5, 9, Scrapers with retouched edges that resemble tools found in Mousterian industries. **6, 10, 11,** Convergent scrapers. **7, 8, 19,** Double scrapers. **12–14,** Denticulates. **15–17,** Borers. **18,** Notch.

References

1 Zhang, M. L. *et al.* The record of paleoclimatic change from stalagmites and the determination of termination II in the south of Guizhou Province, China. *Science in China Series D: Earth Sciences* **47**, 1-12, doi:10.1007/BF03028857 (2004).

2 Li, Y. X. & Wen, B. H. *Guanyindong—A Lower Paleolithic Site at Qianxi County, Guizhou Province*. (Cultural Relics Publishing House, 1986).

3 Pei, W. C., Yuan, C. S., Lin, Y. P., Chang, Y. Y. & Tsao, C. T. Discovery of Paleolithic chert artifacts in Kuan-Yin-Tung Cave in Chien-Hsi-Hsien of Kweichow Province. *Vertebrat Palasiatic* **9**, 270-279 (1965).

4 Yuan, S. X., Chen, T. M. & Gao, S. J. Uranium series chronological sequence of some Paleolithic sites in South China. *Acta Anthropologica Sinica* **5**, 179-190 (1986).

5 Grün, R., Eggins, S., Kinsley, L., Moseley, H. & Sambridge, M. Laser ablation U-series analysis of fossil bones and teeth. *Palaeogeogr. Palaeoclimatol. Palaeoecol.* **416**, 150-167, doi:https://doi.org/10.1016/j.palaeo.2014.07.023 (2014).

6 Shen, G. J. & Jin, L. H. U-series dating of speleothem samples from Guanyindong Cave at Qianxi County, Guizhou Province. *Acta Anthropologica Sinica* **11**, 93-100 (1992).

7 Hovers, E. *The lithic assemblages of Qafzeh Cave*. (Oxford University Press, 2009).

8 Perpère, M. Apport de la typométrie à la définition des éclats Levallois: l'exemple d'Ault. *Bulletin de la Société préhistorique française*, 115-118 (1986).

9 Boëda, E. Approche de la variabilité des systèmes de production lithique des industries du paléolithique inférieure et moyen: chronique d'une variabilité attendue. *Techniques Culture* **17–18**, 31–79 (1991).

10 Freeman, L. G. in *Paleoanthropology in the People's Republic of China: A Trip Report of the American Paleoanthropology Delegation: Submitted to the Committee on Scholarly Communication with the People's Republic of China* Vol. 4 (eds William White Howells & Patricia Jones Tsuchitani) 79-114 (National Academies, 1977).

11 Li, Y., Hou, Y. & Boëda, E. Mode of débitage and technical cognition of hominids at the Guanyindong site. *Chinese Science Bulletin* **54**, 3864-3871 (2009).

12 Gao, X. Paleolithic Cultures in China: Uniqueness and Divergence. *Curr Anthrop* **54**, S358-S370, doi:10.1086/673502 (2013).

13 Bar-Yosef, O. & Van Peer, P. The Chaîne Opératoire Approach in Middle Paleolithic Archaeology. *Curr Anthrop* **50**, 103-131, doi:10.1086/592234 (2009).

14 Monnier, G. F. & Missal, K. Another Mousterian Debate? Bordian facies, *chaîne op eratoire* technocomplexes, and patterns of lithic variability in the western European Middle and Upper Pleistocene. *Quaternary International* **350**, 59-83 (2014).

15 Boëda, E. *Approche technologique du concept Levallois et évaluation de son champ d'application: étude de trois gisement saaliens et weichseliens de la France septentrionale*, Paris 10, (1986).

16 Dibble, H. L. Biache Saint-Vaast, Level IIA: A comparison of analytical approaches. *The definition and interpretation of Levallois technology*, 93-116 (1995).

17 Mathias, C. After the Lower Palaeolithic: Lithic ramification in the early Middle Palaeolithic of Orgnac 3, layer 2 (Ardèche, France). *Quaternary International* **411**, 193-201, doi:https://doi.org/10.1016/j.quaint.2016.01.033 (2016).

18 Moncel, M.-H. *et al.* The Emergence of Neanderthal Technical Behavior: New Evidence from Orgnac 3 (Level 1, MIS 8), Southeastern France. *Curr Anthrop* **52**, 37-75, doi:10.1086/658179 (2011).

19 Li, Y. H. *Tehnological study of lithic industry of the Guanyindong site, Guizhou province, south-west of China* PhD thesis, The Institute of Vertebrate Paleontology and Paleoanthropology, Chinese Academy of Sciences, (2009).

20 Bar-Yosef, O. & Kuhn, S. L. The big deal about blades: Laminar technologies and human evolution. *Amer Anthrop* **101**, 322-338 (1999).

21 Dibble, H., L. & McPherron, S., P. The missing Mousterian. *Curr Anthrop* **47**, 777 (2006).

22 Marwick, B., Clarkson, C., O'Connor, S. & Collins, S. Early modern human lithic technology from Jerimalai, East Timor. *J Hum Evol* **101**, 45-64 (2016).

23 Dibble, H. The Mousterian Industry from Bisitun Cave (Iran). *Paleorient* **10** (1984).

24 Brantingham, P. J., Olsen, J. W., Rech, J. A. & Krivoshapkin, A. I. Raw Material Quality and Prepared Core Technologies in Northeast Asia. *J Archaeol Sci* **27**, 255-271 (2000).

25 Shimelmitz, R. & Kuhn, S. L. The toolkit in the core: There is more to Levallois production than predetermination. *Quatern Int*, doi:https://doi.org/10.1016/j.quaint.2017.08.011 (2017).

26 Wang, H. & Song, M. Ckmeans. 1d. dp: optimal k-means clustering in one dimension by dynamic programming. *The R journal* **3**, 29 (2011).

27 Moore, M. W. The tula adze: Manufacture and purpose. *Antiquity* **78**, 61-73, doi:10.1017/S0003598X00092930 (2004).

28 Leader, G., Abdolahzadeh, A., Lin, S. C. & Dibble, H. L. The effects of platform beveling on flake variation. *Journal of Archaeological Science: Reports* **16**, 213-223, doi:https://doi.org/10.1016/j.jasrep.2017.09.026 (2017).

29 Watanabe, T. & Kanazawa, M. Observations on the melt-off pores of sintered Al-5%Cu alloy compacts by the use of scanning electron microscope. *Journal of the Japan Society of Powder and Powder Metallurgy* **20**, 87-88, doi:10.2497/jjspm.20.87 (1973).

30 Chiotti, L., Dibble, H. L., Olszewski, D. I., McPherron, S. P. & Schurmans, U. A. Middle Palaeolithic lithic technology from the western high desert of Egypt. *J Field Archaeol* **34**, 307-318, doi:10.1179/009346909791070862 (2009).

31 Herries, A. I. R. A Chronological Perspective on the Acheulian and Its Transition to the Middle Stone Age in Southern Africa: The Question of the Fauresmith. *International Journal of Evolutionary Biology* **2011**, 25, doi:10.4061/2011/961401 (2011).

32 Porat, N. *et al.* New radiometric ages for the Fauresmith industry from Kathu Pan, southern Africa: Implications for the Earlier to Middle Stone Age transition. *J Archaeol Sci* **37**, 269-283, doi:https://doi.org/10.1016/j.jas.2009.09.038 (2010).

33 Tryon, C. A. & Faith, J. T. Variability in the Middle Stone Age of Eastern Africa. *Curr Anthropol* **54**, S234-S254, doi:10.1086/673752 (2013).

34 Brown, F. H. & Fuller, C. R. Stratigraphy and tephra of the Kibish Formation, southwestern Ethiopia. *J Hum Evol* **55**, 366-403, doi:https://doi.org/10.1016/j.jhevol.2008.05.009 (2008).

35 Grün, R. *et al.* Direct dating of Florisbad hominid. *Nature* **382**, 500-501 (1996).

36 Douze, K. & Delagnes, A. The pattern of emergence of a Middle Stone Age tradition at Gademotta and Kulkuletti (Ethiopia) through convergent tool and point technologies. *J Hum Evol* **91**, 93-121, doi:https://doi.org/10.1016/j.jhevol.2015.11.006 (2016).

37 Tryon, C. Middle Stone Age Lithic Technology of the Kapthurin Formation (Kenya). *Curr Anthropol* **47**, 367-375, doi:10.1086/503066 (2006).

38 Hawkins, A. L. *et al.* New research on the prehistory of the escarpment in Kharga Oasis, Egypt. *NYAME AKUMA* **55**, 8-14 (2001).

39 Van Peer, P. *et al.* The Early to Middle Stone Age Transition and the Emergence of Modern Human Behaviour at site 8-B-11, Sai Island, Sudan. *J Hum Evol* **45**, 187-193, doi:https://doi.org/10.1016/S0047-2484(03)00103-9 (2003).

40 Buraczynski, J. & Butrym, J. in *Loess and Environment* Vol. 9 (ed M. Pesci) 81-94 (1987).

41 Falguères, C. *et al.* The Lower Acheulian site of Ambrona, Soria (Spain): ages derived from a combined ESR/U-series model. *J Archaeol Sci* **33**, 149-157, doi:https://doi.org/10.1016/j.jas.2005.07.006 (2006).

42 Santonja, M. & Villa, P. The Lower Paleolithic of Spain and Portugal. *J World Prehist* **4**, 45-94, doi:10.1007/BF00974819 (1990).

43 Falguères, C. *et al.* Earliest humans in Europe: the age of TD6 Gran Dolina, Atapuerca, Spain. *J Hum Evol* **37**, 343-352, doi:https://doi.org/10.1006/jhev.1999.0326 (1999).

44 Fontana, F. *et al.* Widespread diffusion of technical innovations around 300,000 years ago in Europe as a reflection of anthropological and social transformations? New comparative data from the western Mediterranean sites of Orgnac (France) and Cave dall'Olio (Italy). *J Anthropol Archaeol* **32**, 478-498, doi:http://dx.doi.org/10.1016/j.jaa.2013.08.003 (2013).

45 Carbonell, E. & Rodríguez, X. P. El Paleolítico Inferior En Cataluña. *VELEIA* **24-25**, 331-343 (2008).

46 Falguères, C., Bahain, J.-J. & Saleki, H. U-Series and ESR Dating of Teeth from Acheulian and Mousterian Levels at La Micoque (Dordogne, France). *J Archaeol Sci* **24**, 537-545, doi:http://dx.doi.org/10.1006/jasc.1996.0137 (1997).
47 Tuffreau, A. *L'Acheuléen dans la vallée de la Somme et Paléolithique moyen dans le Nord de la France: données récentes*. (Centre d'études et de recherches préhistoriques, Université des sciences et technologies de Lille, 2001).
48 Michel, V. *et al.* Application of U/Th and $^{40}Ar/^{39}Ar$ dating to orgnac 3, a Late Acheulean and Early Middle Palaeolithic site in Ardèche, France. *Plos One* **8**, doi:10.1371/journal.pone.0082394 (2013).
49 Jaubert, J. & Bordes, J.-G. 370 (Société préhistorique française, 2008).
50 White, M. & Ashton, N. Lower Palaeolithic Core Technology and the Origins of the Levallois Method in North‐Western Europe. *Curr Anthropol* **44**, 598-609, doi:10.1086/377653 (2003).
51 Westaway, R., Bridgland, D. & White, M. The Quaternary uplift history of central southern England: evidence from the terraces of the Solent River system and nearby raised beaches. *Quaternary Sci Rev* **25**, 2212-2250, doi:http://dx.doi.org/10.1016/j.quascirev.2005.06.005 (2006).
52 Santonja, M. & Villa, P. in *Axe age : Acheulian tool-making from quarry to discard* (eds N. Goren-Inbar & Gonen Sharon) (Equinox, 2006).
53 Grimaldi, S. Analyse technologique, chaîne opératoire et objectifs techniques. Torre in Pietra (Rome, Italie). Torre in Pietra (Rome, Italy). Technological analysis, chaîne opératoire and technical objectives. *Paléo*, 109-122 (1998).
54 Tuffreau, A. in *The Transition from the Lower to Middle Palaeolithic and the Origin of Modern Man* Vol. 151 (ed A. Ronen) 137-149 (British Archaeological Reports, International Series, 1982).
55 Gagnepain, J. & Gaillard, C. in *La grotte de la Baume Bonne (Quinson, Alpes de Haute-Provence) : synthèse chronostratigraphique et séquence culturelle d'après les fouilles récentes (1988-1997).* 73-86 (John and Erica Hedges Ltd).
56 Jarry, M., D., C., L.A., L. & V., M. *Les Bosses (La Magdelaine, Lot, France): Un gisement paléolithique moyen antérieur à l'avant-dernier Interglaciaire sur la moyenne terrasse du Lot*. (Société Préhistorique Française, 2007).
57 Van Baelen, A., Meijs, E., Van Peer, P., de Warrimont, J.-P. & De Bie, M. An early Middle Palaeolithic site at Kesselt-Op de Schans (Belgian Limburg). Preliminary result. *Notae Praehistoricae* **27**, 19-26 (2007).
58 Ryssaert, C. Lithische technologie te Mesvin IV: selectiecriteria voor geretoucheerde werktuigen en hun relatie met Levalloiseindproducten. *Anthropologica Et Praehistorica* **117**, 13-33 (2006).
59 Colonge, D. *et al.* De la transition paléolithique inférieur-moyen dans la vallée de la Garonne: l'Acheuléen supérieur de Raspide 2 (Blagnac, Haute-Garonne). *Bulletin de la Société préhistorique française* **107**, 205-225 (2010).
60 Thissen, J. *Die Paläolithischen Freilandstationen von Rheindahlen im Löss Zwischen Maas und Niederrhein*. (Rheinische Ausgrabungen 59, Verlag Philipp von Zabern, Mainz, 2006).
61 Blackwell, B. & Schwarcz, H. P. in *La Grotte Vaufrey: Paléoenvironnement, chronologie, activités humaines* (ed Jean-Philippe Rigaud) 365–380 (Mémoires de la Société Préhistorique Française, 1988).
62 Balescu, S. & Tuffreau, A. La phase ancienne du Paléolithique moyen dans la France septentrionale (stades isotopiques 8 à 6) : apports de la datation par luminescence des séquences lœssiques. *Archaeological Almanac* **16**, 5-22 (2004).
63 Wisniewski, A. & Fridrich, J. in *Middle Palaeolithic Activity and Palaeoecology* (eds J. M. Burdukiewicz & A. Wisniewski) 217–243 (Studia Archeologiczne 41, Biblioteka Cyfrowa, Wydawnictwa Uniwersytetu Wroclawskiego, 2010).
64 Bahain, J.-J. *La méthode de datation par résonance de spin électronique (ESR) au Muséum national d'histoire naturelle. Vingt ans de recherches méthodologiques et d'applications géochronologiques*, Université Michel de Montaigne - Bordeaux III, (2007).
65 Cyrek, K., Sudoł, M., Czyżewski, Ł., Osipowicz, G. & Grelowska, M. Middle Palaeolithic cultural levels from Middle and Late Pleistocene sediments of Biśnik Cave, Poland. *Quatern Int* **326**, 20-63, doi:http://dx.doi.org/10.1016/j.quaint.2013.12.014 (2014).

66 Sun, X. *et al.* Recuperated optically stimulated luminescence dating of middle-size quartz grains from the Palaeolithic site of Bonneval (Eure-et-Loir, France). *Quat Geochronol* **5**, 342-347, doi:http://dx.doi.org/10.1016/j.quageo.2009.05.004 (2010).
67 Jaubert, J. & Servelle, C. in *L'Acheuléen dans l'Ouest de l'Europe* (ed A. Tuffreau) 77-108 (University of Sciences & Technology, Centre d'Etudes et Recherches Préhistoriques, 1996).
68 Brenet, M. *et al.* Interprétation de la variabilité technologique de deux industries du Paléolithique moyen ancien du Bergeracois : Cantalouette 1 et Combe Brune 3 (Creysse, Dordogne). *Bulletin de la Société Préhistorique Française*, 57-81 (2008).
69 Wiśniewski, A. The beginnings and diversity of Levallois methods in the early Middle Palaeolithic of Central Europe. *Quatern Int* **326**, 364-380, doi:http://dx.doi.org/10.1016/j.quaint.2013.10.027 (2014).
70 Marks, A. E. *et al.* Le gisement pléistocène moyen de Galeria Pesada (Estrémadure, Portugal) : premiers résultats. *PALEO* **14**, 77-100 (2002).
71 Adler, D. S. *et al.* Early Levallois technology and the Lower to Middle Paleolithic transition in the Southern Caucasus. *Science* **345**, 1609-1613, doi:10.1126/science.1256484 (2014).
72 Haesaerts, P. & Koulakovskaya, L. V. in *The European Middle Paleolithic* (ed L. V. Koulakovskaya) 21-38 (Shlyakh, Kiev, 2006).
73 Callow, P. & Cornford, J. M. *La Cotte de St. Brelade, 1961-1978 : excavations by C.B.M. McBurney*. (Kluwer Academic, 1986).
74 Delagnes, A. & Ropars, A. in *Paléolithique moyen en pays de Caux (Haute-Normandie). Le Pucheuil, Ettoutteville: Deux gisements de plein air en milieu loessique* (Éditions de la Maison des Sciences de l'Homme, 1996).
75 Adam, A. Les pointes pseudo-Levallois du gisement moustérien Le Rissori, à Masnuy-Saint-Jean (Hainaut, Belgique). *L'Anthropologie* **106**, 695-730, doi:http://dx.doi.org/10.1016/S0003-5521(02)01143-3 (2002).
76 Vandenberghe, J., Roebroeks, W. & van Kolfschoten, T. *Maastricht-Belvédère: Stratigraphy. Palaeoenvironment and Archaeology of the Middle and Late Pleistocene Deposits. Part II*. (Mededelingen Rijks Geologische Dienst, 1993).
77 Ameloot-van der Heijden, N., Dupuis, C., Limondin, N., Munaut, A. V. & Puissegur, J. J. The Middle Palaeolithic open air site of Salouel. *L'Anthropologie* **100**, 555-573 (1996).
78 Picin, A., Peresani, M., Falguères, C., Gruppioni, G. & Bahain, J.-J. San Bernardino Cave (Italy) and the Appearance of Levallois Technology in Europe: Results of a Radiometric and Technological Reassessment. *Plos One* **8**, e76182, doi:10.1371/journal.pone.0076182 (2013).
79 Scott, B., Ashton, N., Lewis, S., Parfitt, S. & White, M. in *The Ancient Human Occupation of Britain* (eds Nick Ashton, Simon Lewis, & Chris Stringer) 67-89 (Elsevier, 2011).
80 Locht, J.-L., Antoine, P., Hérisson, D., Gadebois, G. & Debenham, N. Une occupation de la phase ancienne du Paléolithique moyen à Therdonne (Oise). Chronostratigraphie, production de pointes Levallois et réduction des nucléus. *Gallia préhistoire*, 1-32 (2010).
81 Mallick, R. & Frank, N. A new technique for precise uranium-series dating of travertine micro-samples. *Geochim Cosmochim Ac* **66**, 4261-4272, doi:http://dx.doi.org/10.1016/S0016-7037(02)00999-7 (2002).
82 Rolland, N. The early human occupation of high latitudes, Boreal, continental and periglacial habitats: Middle Palaeolithic milestones In northern Eurasia. *Acta Universitatis Wratislaviensis* **3027**, 15-46 (2010).
83 Akhilesh, K. *et al.* Early Middle Palaeolithic culture in India around 385–172 ka reframes Out of Africa models. *Nature* **554**, 97 (2018).
84 Derevianko, A. P. *et al. Paleoenvironment and Paleolithic human occupation of Gorny Altai: subsistence and adaptation in the vicinity of Denisova Cave*. (2003).
85 Mercier, N. *et al.* Hayonim Cave: a TL-based chronology for this Levantine Mousterian sequence. *J Archaeol Sci* **34**, 1064-1077, doi:http://dx.doi.org/10.1016/j.jas.2006.09.021 (2007).
86 Hershkovitz, I. *et al.* The earliest modern humans outside Africa. *Science* **359**, 456 (2018).
87 Tensorer, J.-M. L. *et al.* Long-term site formation processes at the natural springs Nadaouiyeh and Hummal in the El Kowm Oasis, Central Syria. *Geoarchaeology* **22**, 621-640, doi:10.1002/gea.20177 (2007).
88 Petraglia, M. D. *et al.* Hominin Dispersal into the Nefud Desert and Middle Palaeolithic Settlement along the Jubbah Palaeolake, Northern Arabia. *Plos One* **7**, e49840, doi:10.1371/journal.pone.0049840 (2012).

89 Otte, M. *et al.* Long-term technical evolution and human remains in the Anatolian Palaeolithic. *J Hum Evol* **34**, 413-431, doi:http://dx.doi.org/10.1006/jhev.1997.0199 (1998).

90 Valladas, H. *et al.* Dating the Lower to Middle Paleolithic transition in the Levant: A view from Misliya Cave, Mount Carmel, Israel. *J Hum Evol* **65**, 585-593, doi:http://dx.doi.org/10.1016/j.jhevol.2013.07.005 (2013).

91 Mercier, N. & Valladas, H. Reassessment of TL age estimates of burnt flints from the Paleolithic site of Tabun Cave, Israel. *J Hum Evol* **45**, 401-409, doi:http://dx.doi.org/10.1016/j.jhevol.2003.09.004 (2003).

92 Hoffecker, J. *Desolate landscapes: Ice-Age settlement in Eastern Europe*. (2003).

93 Krivoshapkin, A. I., Kuzmin, Y. & Jull, A. J. T. Chronology of the Obi-Rakhmat Grotto (Uzbekistan): First Results on the Dating and Problems of the Paleolithic Key Site in Central Asia. *Radiocarbon* **52**, 549-554 (2010).

94 Slavinskiy, V. S. & Rybin, E. P. Levallois Convergent Unidirectional Typical Technology in Southern Siberia and the Northern Part of Central Asia: Variability, Distribution, Chronology. *Stratum Plus* **2015**, 285-307 (2015).

95 Derevianko, A. P., Postnov, P., Rybin, E. P., Kuzmin, Y. & Keates, S. G. The Pleistocene peopling of Siberia: A review of environmental and behavioral aspects. *Indo-Pacific Prehistory Association Bulletin* **25**, 57-68 (2005).

96 Rose, J. I. *et al.* The Nubian Complex of Dhofar, Oman: An African Middle Stone Age Industry in Southern Arabia. *Plos One* **6**, e28239, doi:10.1371/journal.pone.0028239 (2011).

97 Shirokov, V. N., Volkov R. B., Kosintsev, P. A. & Lapteva, E. G. Paleoliticheskaya stoyanka Bogdanovka (Yuzhnyy Ural). *Rossiyskaya arkheologiya* **1**, 111-125 (2011).

98 Svendsen, J. I. *et al.* Geo-archaeological investigations of Palaeolithic sites along the Ural Mountains – On the northern presence of humans during the last Ice Age. *Quaternary Sci Rev* **29**, 3138-3156, doi:https://doi.org/10.1016/j.quascirev.2010.06.043 (2010).

99 Pavlov, P., Roebroeks, W. & Svendsen, J. I. The Pleistocene colonization of northeastern Europe: a report on recent research. *J Hum Evol* **47**, 3-17, doi:https://doi.org/10.1016/j.jhevol.2004.05.002 (2004).

100 Petraglia, M. *et al.* Middle paleolithic assemblages from the Indian subcontinent before and after the Toba super-eruption. *Science* **317**, 114-116, doi:10.1126/science.1141564 (2007).

101 Blinkhorn, J., Achyuthan, H., Petraglia, M. & Ditchfield, P. Middle Palaeolithic occupation in the Thar Desert during the Upper Pleistocene: the signature of a modern human exit out of Africa? *Quaternary Sci Rev* **77**, 233-238, doi:DOI 10.1016/j.quascirev.2013.06.012 (2013).

102 Hidjrati, N., Kimball, L. R. & Koetje, T. A. Middle and Late Pleistocene investigations of Myshtulgaty Lagat (Weasel Cave) North Ossetia, Russia. *Antiquity* **77**, 298 (2003).

103 Chlachula, J., Drozdov, N. I. & Ovodov, N. D. Last Interglacial peopling of Siberia: the Middle Palaeolithic site Ust'-Izhul', the upper Yenisei area. *Boreas* **32**, 506-520, doi:10.1111/j.1502-3885.2003.tb01231.x (2003).

104 Vasil'ev, S. A., Kuzmin, Y. V., Orlova, L. A. & Dementiev, V. N. Radiocarbon-based chronology of the Paleolithic in Siberia and its relevance to the peopling of the New World. *Radiocarbon* **44**, 503-530 (2002).

105 Blinkhorn, J. Late Middle Palaeolithic surface sites occurring on dated sediment formations in the Thar Desert. *Quatern Int* **350**, 94-104, doi:https://doi.org/10.1016/j.quaint.2014.01.027 (2014).

106 Andrews, J. E. *et al.* Do Stable Isotope Data from Calcrete Record Late Pleistocene Monsoonal Climate Variation in the Thar Desert of India? *Quaternary Res* **50**, 240-251, doi:https://doi.org/10.1006/qres.1998.2002 (1998).

107 Wang, X. K., Wei, J., Chen, Q. J., Tang, Z. W. & Wang, C. X. A preliminary study on the excavation of the Jinsitai Cave site (in Chinese). . *Acta Anthropologica Sinica* **29**, 15-32 (2010).

108 Krause, J. *et al.* Neanderthals in central Asia and Siberia. *Nature* **449**, 902-904, doi:http://www.nature.com/nature/journal/v449/n7164/suppinfo/nature06193_S1.html (2007).

109 Liu, D. *et al.* Progress in the stratigraphy and geochronology of the Shuidonggou site, Ningxia, North China. *Chinese Sci Bull* **54**, 3880, doi:10.1007/s11434-009-0652-y (2009).

110 Li, F. *et al.* The development of Upper Palaeolithic China: new results from the Shuidonggou site. *Antiquity* **87**, 368-383 (2013).

111 Boëda, E., Hou, Y. M., Forestier, H., Sarel, J. & Wang, H. M. Levallois and non-Levallois blade production at Shuidonggou in Ningxia, North China. *Quaternary International*, doi:http://dx.doi.org/10.1016/j.quaint.2012.07.020 (2013).
112 Derevianko, A. *et al.* The stratified cave site of Tsagaan Agui in the Gobi altai (Mongolia). *Archeology, Ethnology, and Anthropology of Eurasia* **1**, 23-36 (2000).
113 Zwyns, N., Gladyshev, S., Tabarev, A. & Gunchinsuren, B. Mongolia: Palaeolithic. *Encyclopedia of Global Archaeology* **8**, 5025-5032 (2014).
114 Kreutzer, S. *et al.* Introducing an R package for luminescence dating analysis. *Ancient TL* **30**, 1-8 (2012).
115 Peng, J. & Li, B. Single-aliquot regenerative-dose (SAR) and standardised growth curve (SGC) equivalent dose determination in a batch model using the R Package 'numOSL'. *Ancient TL* **35**, 32-53 (2017).

Selected Levallois cores in 3D PDF Format

The following three pages show the CT-scanned structures of three selected Levallois cores from GYD in 3D PDF format, where the structures can be manipulated within Acrobat Reader.

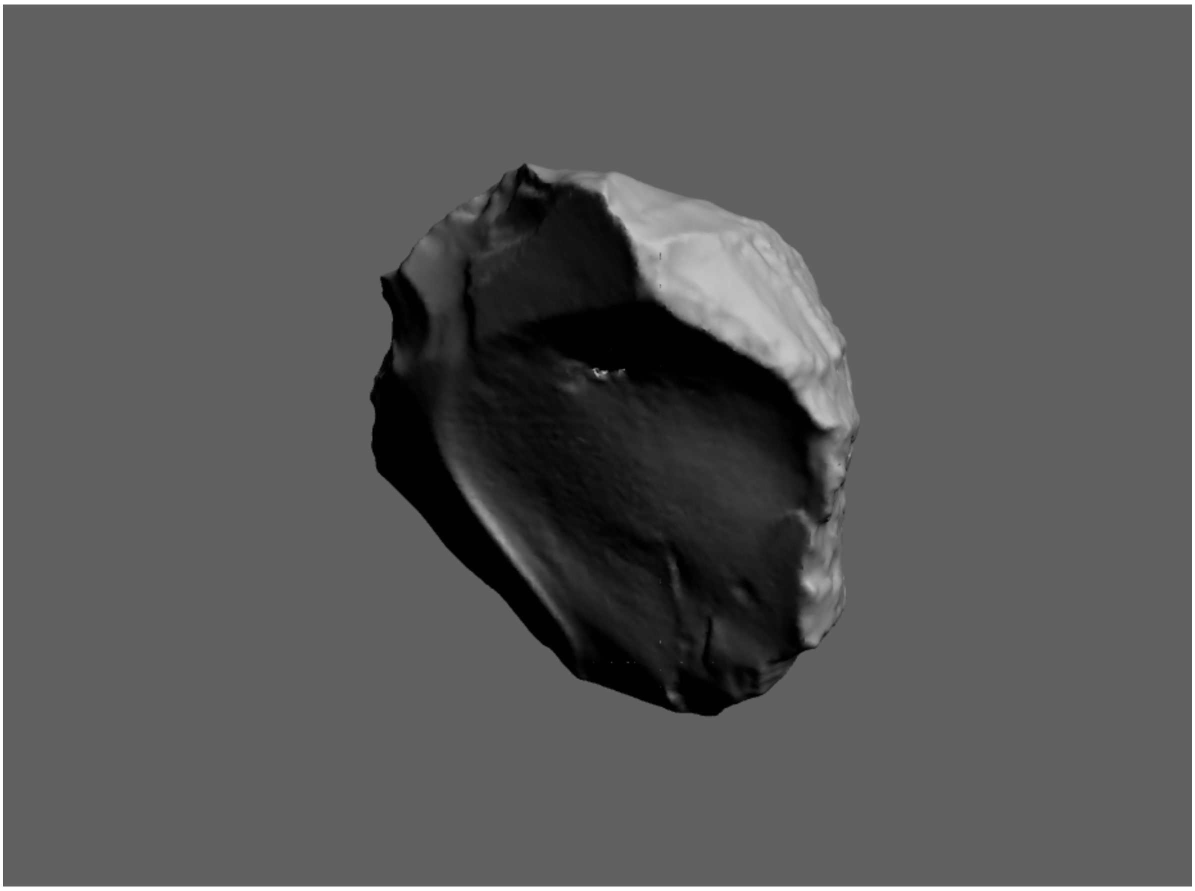

Supplementary Data 1 | The structure of a Levallois preferential core from Guanyindong Cave. The maximum dimension, length and thickness of this specimen are 83, 72 and 23 mm, respectively. This artefact is identical to that appearing in Fig. 3b and Extended Data Figure 5b.

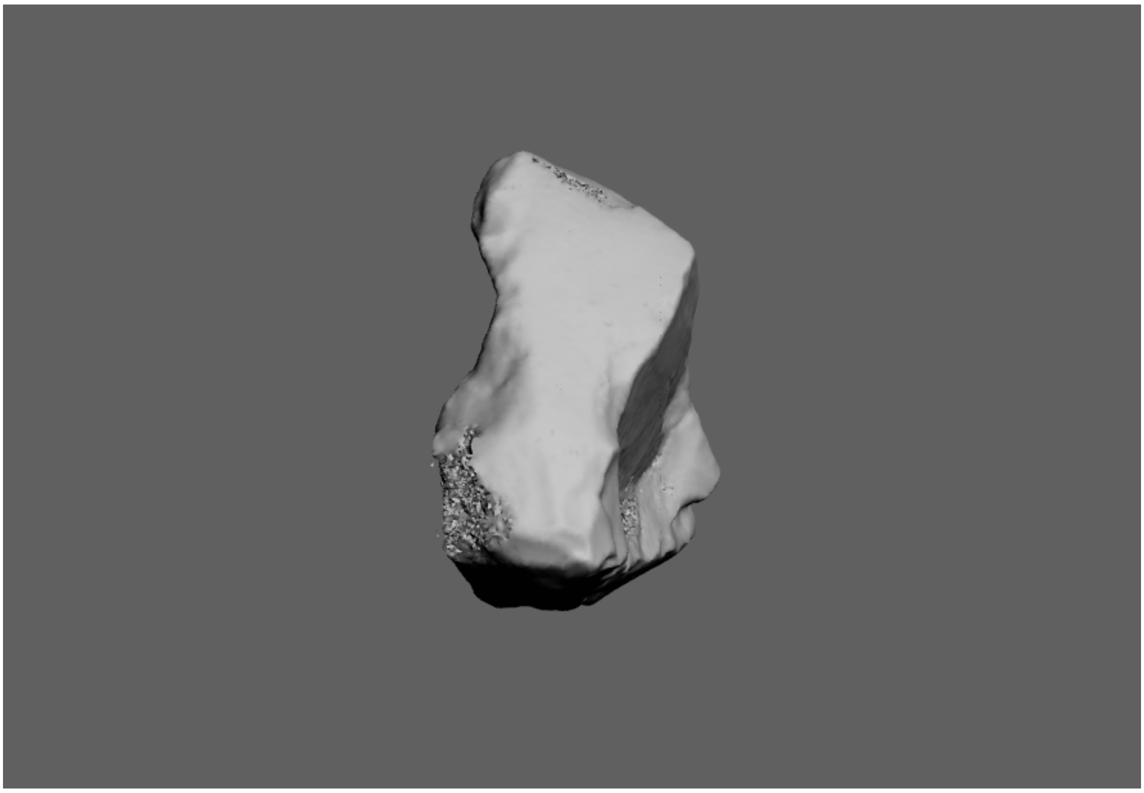

Supplementary Data 2 | The structure of a Levallois preferential core from Guanyindong Cave. The maximum dimension, length and thickness of this specimen are 86, 76 and 22 mm, respectively. This artefact is identical to that appearing in Fig. 3c and Extended Data Figure 5c.

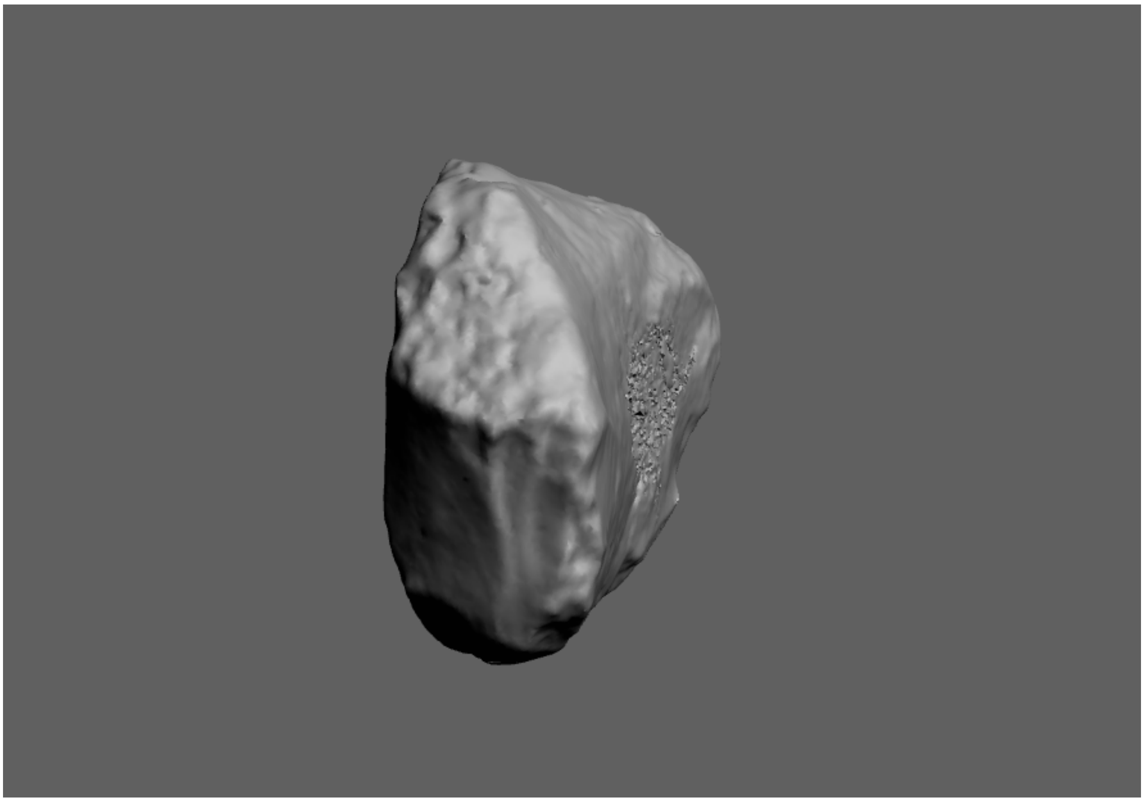

Supplementary Data 3 | The structure of a Levallois recurrent core from Guanyindong Cave. The maximum dimension, length and thickness of this specimen are 69, 56 and 21 mm, respectively. This artefact is identical to that appearing in Fig. 3a and Extended Data Figure 5a.